Smart microsystems for cell manipulations

Mark Prince

Doctor of Philosophy

ASTON UNIVERSITY

October 2006

Smart microsystems for cell manipulations

Mark Prince

Engineering Systems and Management
ASTON UNIVERSITY

A thesis submitted for partial fulfilment of the degree of
Doctor of Philosophy

October 2006

This thesis documents the design, manufacture and testing of a passive and non-invasive micro-scale planar particle-from-fluid filter for segregating cell types from a homogeneous suspension. The microfluidic system can be used to separate spermatogenic cells from testis biopsy samples, providing a mechanism for filtrate retrieval for assisted reproduction therapy. The system can also be used for point-of-service diagnostics applications for hospitals, lab-on-a-chip pre-processing and field applications such as clinical testing in the third world.

Various design concepts are developed and manufactured, and are assessed based on etched structure morphology, robustness to variations in the manufacturing process, and design impacts on fluid flow and particle separation characteristics. Segregation was measured using image processing algorithms that demonstrate efficiency is more than 55% for 1 μl volumes at populations exceeding 1×10^7. The technique supports a significant reduction in time over conventional processing, in the separation and identification of particle groups, offering a potential reduction in the associated cost of the targeted procedure.

The thesis has developed a model of quasi-steady wetting flow within the micro channel and identifies the forces across the system during post-wetting equalisation. The model and its underlying assumptions are validated empirically in microfabricated test structures through a novel Micro-Particle Image Velocimetry technique.

The prototype devices do not require ancillary equipment nor additional filtration media, and therefore offer fewer opportunities for sample contamination over conventional processing methods. The devices are disposable with minimal reagent volumes and process waste. Optimal processing parameters and production methods are identified with any improvements that could be made to enhance their performance in a number of identified potential applications.

ICSI, micro-PIV, cell separation, microfluidic flow, microfilter

dedicated to Emma and my family

Acknowledgements

Contents

1

List of Figures

8

9

10

11

14

List of Tables

15

Nomenclature

Roman Symbols

A	Area	m^2
A_{lv}	Area of the liquid-vapour interface	m^2
A_{sl}	Area of the solid-liquid interface	m^2
A_{sv}	Area of the solid-vapour interface	m^2
$\bar{u}$	Mean velocity	m/s
D	Diffusion coefficient	
ΔP_{lv}	Pressure difference across the liquid-vapour interface	N/m^2
d_h	Channel or pipe hydraulic diameter	m
F	Force	N
H	the height of the inlet fluid level above that of the channel	m
K_n	Knudsen number	
L	characteristic dimension	m
l	Channel or pipe length	m
m_o	molecular mass	kg
N	Molecular population	
n	Average number density	
P	Pressure	N/m^2
Q	Mean volumetric flow rate	m^3/s

R	Radius	m
R_e	Reynolds number	
T	Temperature	$^{\circ}C$
U	Energy	J
U_T	total energy	J
V	Volume	m^3
x	displacement or distance in the x direction	m
l_0	Initial offset in x at time $t = 0$	m
$l(t)$	progression into capillary in the x direction w.r.t time	m
y	Distance or length in y-direction	m

Greek Symbols

γ_{lv}	surface energy of liquid-vapour interface	
γ_{sl}	Surface energy of liquid-solid interface	
γ_{sv}	Surface energy of solid-vapour interface	
λ	gas mean free path	m
ρ	density	kg/m^3
σ	Surface tension line force	N/m
τ	Fluid shear stress	N
θ_c	Static contact angle	$^{\circ}$

18

Chapter 1

Introduction

1.1 Problem Description

Advancements in biological science have led to the generation of a myriad of methods for the processing and separation of cells from a mixture or mixed population suspension. A modern laboratory is equipped with methods and apparatus capable of measuring a variety of cellular parameters, and in many cases the facilities to sort and count differing cells based on small chemical or physiological differences. Typically, sorting and separating technologies make use of chemical or radiochemical markers that adhere to specific sites on a cell based on its biochemistry. Other sorting or singulation mechanisms exploit differing cellular masses or mobilities and require time intensive diluting and centrifuging cycles. The cell suspension is systematically 'spun down' through an agent of known viscosity in order to exaggerate the differences in cellular mass, permitting smaller cells to be decanted off. This has the drawback that the fluid suspension must be brought into contact with several potentially polluting or contaminating agents. In-vitro

studies cannot be processed in this way, as the cells are being processed with the intention of returning them to a donor, or to another subject to form part of a living organism. A stark example of this is In-Vitro Fertilisation (IVF), or more specifically Intra-Cytoplasmic Sperm Injection (ICSI). Biological applications such as this involve the direct manipulation of oocytes and spermatogenic cells to the end of procreation. The ethically and chemically sensitive nature of these cells in particular preclude the use of chemical tagging, leaving the andrology clinician with few choices in the acquisition and manipulation of the cells.

The majority of patients referred for Assisted Reproduction Therapy (ART) are done so as a result of male factor infertility, which could arise through a variety of mechanisms. Male infertility due to absence of spermatozoa in the ejaculate, a condition known as azoospermia, can be classified into two types, obstructive and non-obstructive. In the case of the latter, azoospermia is due to arrest in the maturation of the spermatogenic cells and requires that germ cells are harvested direct from the site of their manufacture and development: the seminiferous tubules within the testes.

The cells are retrieved surgically as a biopsy pellet containing a variety of tissues and a range of germ cells from all orders of maturity. As germ cells mature they become smaller, beginning as a large round spermatogonion and ending as a small and slender spermatozoon. Processing these tissues ready for the ICSI process is time intensive, requiring manual mincing of the pellets beneath a microscope to liberate the cells, successive cell separation cycles through centrifugation, and individual cell discrimination before the possibility of identifying a viable spermatogenic cell - if indeed there are any viable cells available.

1.2   Novel Separation Concept

This research aims to develop an alternative method for rapidly separating ethically, mechanically, biologically and chemically sensitive materials in solution based on their morphology and size without the need for chemical tagging or staining, in a much shorter time period than previously possible, and using no additional tools or techniques other than those found in a conventional ICSI capable laboratory. It is postulated that through the application of microtechnologies in the form of a passive cell segregation device, the components of a cell, or particle, suspension could be rapidly segregated according to cell size and morphology unaided by external pressure sources or forces.

Using proven bio-compatible materials such as silicon and glass aids in alleviating concerns over sample damage or pollution during the separation process, whilst the single use package removes the need for inter-sample cleaning time consuming and potentially polluting cleaning processes, and eliminates opportunities for cross-contamination between successive samples. The manufacturing processes involved in their fabrication are derived from semiconductor manufacture and as such are well established and cost effective for large production volumes. Furthermore the raw materials of silicon and glass are ubiquitous, naturally abundant and in-line with conventional laboratory materials such as glass, for which there are already standard disposal protocols.

The inclusion of physical filtration structures provide that any samples processed are not contaminated after filtration - opening new opportunities for field-based cell analysis. The process simplicity leads to a marked reduction in processing time and offer great potential for standardisation of separation processes across a number of fields and disciplines.

It is the intention that the research presented in this thesis will show the potential of Micro Electro Mechanical Systems (MEMS) tools and techniques in the creation of new procedures and protocols in the direct manipulation of cells and cell populations for immediate application within a clinical environment, and with minimal supporting equipment. The project has been targetted towards the development of a single use statistical amplifier to supplement efforts within a urological laboratory environment to disseminate mixed cell populations and accelerate the procedure of acquiring viable donor cells for IntraCytoplasmic Sperm Injection. ICSI involves the direct injection of an immobilised human spermatozoon, or late-stage germ cell, directly into a prepared oocyte thereby artificially fertilising the egg and increasing the probability of a successful foetus conception. This direct cellular manipulation requires highly skilled laboratory technicians and the use of specialist micromanipulation and microscopy equipment. However, it could be argued that the isolation of the sperm cells in preparation for the procedure is an equally lengthy and complex task. Through the application of microtechnologies a tool or set of tools can be developed and refined that can simplify this lengthy preparatory procedure into a less skilled, subsequently less time-consuming, and more standardised process through exploiting micro-fluidic principles.

This research has the potential to generate such an enhancement that could result in the first clinical deployment of a microfabricated device or devices for the semi-automated processing and analysis of biological tissue for the ICSI procedure. The speed and ease of use means devices such as these could be used for applications such as on the spot diagnostics for hospitals, lab-on-a-chip pre-processing, drug house research and field applications such as AIDS testing in the third world.

1.3   Objectives

The objective of the work in this thesis may be summarised as follows:

1. to study principles and characteristics of microfluidic flows

2. to develop a sound working knowledge of microfabrication tools, techniques and materials and their application in biological environments.

3. to develop a working prototype of an unpowered single use microfluidic cell separation device through MEMS technologies with a view to proof and deployment within a clinical environment.

4. to successfully apply a novel etching protocol in the manufacture of the prototypes.

5. to develop experimental techniques for evaluating and testing prototype devices.

6. to analyse the behaviour of fluid within the prototype devices and evaluate their efficacy as both a source of useful fluid power and as statistical cell and particle amplification tool.

7. to characterise the devices and their operation, and identify optimal operating parameters including particulate population and sample load-to-flush ratio.

1.4   Structure of Thesis

Initially a survey of lierature is presented in Chapter 2, indicating the need and applications for cell manipulation and separation within biology, and available methods of achieving this. This is followed by a review of modelling methods applied to the characterisation of micro-flows, or flows within micro-scale systems, and the validity of conventional or classical fluid models. A treatment of the literature on the measurement and observation of liquid flows and micro-flows is presented with a debate on their underlying assumptions. The remainder of the chapter is dedicated to previous work on the separation of particles from a liquid suspension in a micro-scale device and the suitability of the presented techniques or principles as they apply to subsequent cell processing or in-vivo viability.

Chapter Three introduces the process of cell preparation for ART and presents current methodologies applied in spermatogenic cell isolation, and a discussion of the scales of the structures involved. These findings are then summarised in the form of a specification for the design solution to the problem of cell separation for ART. The design concept is presented, discussing the principles it exploits and the aspects of the manufacturing process that influence design decisions. Further detailed designs are identified indicating which aspects of the device concept they represent or are intended to evaluate.

An investigation of the principles of quasi-steady microfluidics is undertaken in Chapter 4, with discussion to the more influential parameters affecting the fluid as the scale of a system is reduced. Particular attention is paid to surface effects such as capillarity and their practical application in both active and passive microfluidic systems. Chapter 5 deals with the mathematical modelling of a fluid flow within a microfabricated channel, an assessment of contemporary approaches

to the modelling of microfluidic flows as applied to wetting and viscous flow, and selection and tailored application of these models to the modelling of the cell separation solution.

The design of experiments and experimental methods for the evaluation of the prototype concept device and a discussion of the criteria against which it was evaluated may be found in chapter 6, followed by their results and a discussion of findings.

Chapter 7 draws the work to a conclusion, discussing all aspects of the work from inception through to experimental evaluation. Potential improvements and further work required are detailed along with a discussion of potential applications of both the statistical amplifiers themselves, and the principles involved in their design, manufacture and function.

Appendix A contains a summary of the features of the various prototype devices along with the manufacturing and fluid flow considerations that inspired them.

Chapter 2

Review of Literature

2.1 Introduction

This chapter reviews and identifies cited examples of cell manipulation, particle processing techniques and technologies, and any shortfalls in the state of the art as applied to the stated problem. The chapter then goes on to review the literature in order to assess the methods and approaches made by way of improving these processes and determine if, and how, they may be applied to the possible application of germ call manipulation.

A technique has been developed that can potentially provide an alternative to conventional cell and particle segregation techniques in a solution that is better suited to the task of germ cell selection for ART. Through the application of microfluidic principles, and the exploitation of microscale structures and physical effects a technology has been developed that can facilitate the rapid segregation of cells or particles held in fluid suspension based on differences in their size or morphology, without the need for external pressure or power sources, and without complex sensing technologies or instrumentation beyond that typically found in

a reproductive therapy laboratory.

2.2   Cell Manipulation

For decades microbiologists have been handling cells, cell cultures and manipulating them both physically and chemically using crude tools and techniques. A vast understanding of biochemistry and physiology has been the result of these trials, however the physical interaction with biological structures on a cellular scale beyond chemically invasive techniques is limited. More recently, since the realisation of microchannels and microfluidic structures, direct cell manipulation has become a possibility and thus yielded many opportunities in biology and genomics [11].

2.2.1   The Need for Cell Manipulation

Initially, cell manipulation is referred to primarily in the physical sense, that is the use of various methods to physically control the position, orientation or activity of a cell or particle. Perhaps the simplest application is that of fixing or immobilising a body, or bodies, in order that it may be subjected to biochemical interrogation. Conventionally this would be done through the deposition of an alcohol based binding or fixing agent, which has potential to alter the cell and thus potentially bias the outcome of an experiment that observes the physical parameters or interactions of the cell [12]. Without the use of a binding agent, the cells are free to move in fluid, and become difficult to image due to their high mobility and as such controlled and detailed visual studies are difficult (Dr. S.N. Smith[1], personal communication, 2006). A non-chemical means of physically restraining a cell would permit such studies without affecting the status of the

---

[1]Aston University, School of Life and Health Sciences

27

cell.

More advanced cell manipulation refers to sorting and processing technologies whereby cells are sorted based on their status, such as in viability assays after a sample has been innoculated as part of a mortality study. This is another area that could be aided by improved manipulation techniques. Finally there are the target fields of ART and genetic manipulation whereby cells must be immobilised and undergo surgical processes involving dissection, aspiration or injection, by way of specialist micromanipulation tooling [4]. Without a means of controlling the cell and its environment directly such processes could not be reliably or repeatably achieved, if indeed they could be achieved at all.

2.2.2 Cell Manipulation in ART

The advent of ICSI has significantly improved the efficacy of assisted fertilisation procedures, and has been demonstrated to be effective in even severe cases of azoospermia through testicular sperm extraction (TESE) [13] [14] and injection, or to a lesser degree through spermatid injection [15]. The actual injection procedure is conducted on a heated microscope stage within the ART clinic using specialised micromanipulation and microinjection equipment and serves as only a single stage in a lengthy process. From the perspective of the male germ cell the process begins much earlier in the actual harvesting, diagnosis and selection of viable cells. For patients suffering from germ cell maturation failure there is a requirement for the harvesting of immature germ cells, known as spermatids, directly from the seminiferous tubules within the testis.

The conventional process by which the spermatogenic cells are separated from the surrounding tissues is detailed by Schlegel *et al* [4] and is summarised in Section 3.1.1. The process involves the manual inspection and dissection of tissues

beneath a dissection microscope using scissors, needles and glass slides. In the event that the desired cells are not located within the biopsy, a further biopsy from an alternative site on the testis must be taken. Once a viable cell harvest is observed the tissue suspension is refined through multiple centrifugation and decantation cycles until approximate single cell-type suspensions are obtained from which a single cell can be aspirated and used.

Since its inception and successful application in 1992 by urologists in Belgium [16] the tools available for ICSI have been further developed and refined, culminating in specialised cell holding pipettes and fine injection and aspiration needles of the order of 5-7 microns in diameter (figure 2.1). The small scale of the cells, and subsequently the tools, require the intermediate control using micromanipulation equipment: robotic devices that offer the operator the capability of working with sub-micron precision. Verheyen *et al* were among the first to indicate the need for improved methods in the selection of spermatogenic cells in the treatment of severe male infertility, ephasising in particular the difficulty in identifying round spermatids in testis biopsy tissues [17]. A range of possible solutions are put forward by Aslam *et al* [7] with endorsement going to Fluorescence Activated Cell Sorter (FACS) separation based on differences in forward and wide angle light scattering profiles.

Approaches to tackling cellular manipulation can be considered to be from one of two directions: *single cell* and *multiple cell*.

(i) Micromanipulation tools being used to perform ICSI

(ii) Microinjection needle mounted on microscope
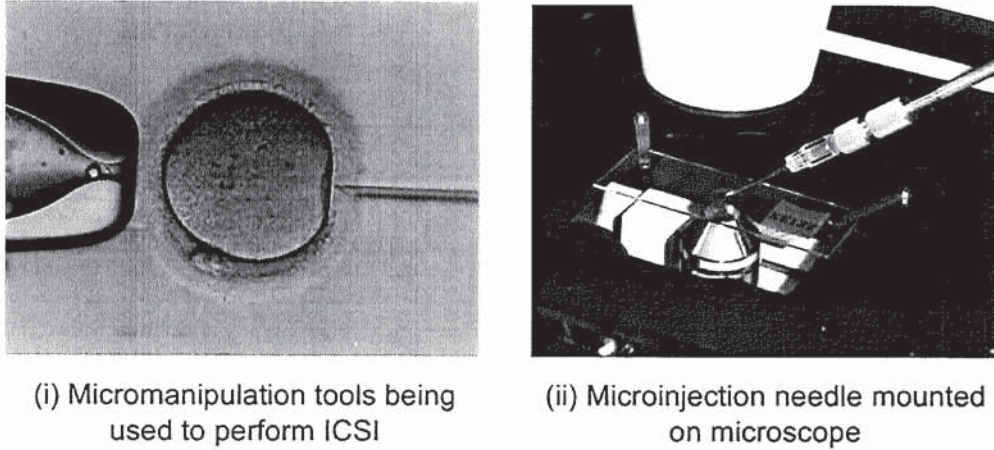
Figure 2.1: specialised micromanipulation and microinjection tools typical to the the ICSI procedure

2.2.3 Single Cell Manipulation

Perhaps the most versatile, commercially available, non-contact manipulation technique is that employed by laser tweezers. Suited mostly for smaller cells and particles laser tweezers apply a force onto the body through the difference in refractive index between the cell and its host fluid. The change in refractive index has the effect of re-directing photons incident on the body away into the fluid and results in a small but not insignificant force. Applegate [18] demonstrates the use of this effect in order to generate configurable optical boundaries that can be use to hold, steer or move cells in a controlled manner. Ashkin [19] relates how this technique may be exploited to the end of applying physical forces, and the measurement of biological cytoskeletal forces [20], further demonstrating the versatility of the technique.

Laser tweezers can also be used for indirect contact manipulation whereby refractive particles, such as diamond, can be used as tools or handles on which the laser

can effect a higher force and provide highly dextrous cell manipulation. Gosse *et al* [21] introduce another extension in the pseudo-non-contact manipulation process through the direct manipulation of magnetic particles by way of a magnetic field and using these to perform similar feats of measurement and manipulation [22]. Lee *et al* [23] demonstrate that micro-particles and a yeast cell have been spatially controlled with precision using an array of electrodes, insulated from the sample but in proximity to a ground plane on the far side of the cell media, generating a surrounding electric field and resultant force capable of inducing cell movement. Diop [24] demonstrates the successful retention and manipulation of sperm cells using the interfacial surface of an opto-thermally generated microbubble, a 'soft-trapping' technique shown to leave the cell un-impaired once released. Being only transient in nature the bubbles can be expanded and collapsed, or fused with others to facilitate cell transfer [25]. The common factors between all of these systems being their non-contact nature, and a dependence upon specialist ancillary control equipment.

Chronis [26] presents an alternative method by way of a microfabricated robotic microgripper that uses elecrothermally uniaxially actuated mechanical fingers to physically grasp a single cell. Although benefiting from a reduced requirement for ancillary control equipment their application is perhaps limited due to the limited degrees of motion and the large scale of the grippers themselves - with a minimum grip diameter of the order of 7 μm. The precise control of individual cells is in the majority of cases dependent upon a preliminary separation process by which they are isolated from a group of cells. These methods were of course conceived with a view to the precise control of individual cells, which must presumably be isolated by other means beforehand.

2.2.4   Multiple Cell Manipulation: Bulk Processing

Bulk cell handling processes can range from the simplest means, such as a microporous filter membrane, to advanced computer guided separation systems, an example of which is the widely deployed Fluorescense Activated Cell Sorter (FACS). The FACS is capable of rapid cell discrimination and separation with an accuracy permitting the selection of a single cell from a population of thousands [27]. The cells are identified by size, or more commonly fluorescent emission spectra, and are atomised into airborne fluid droplets to which an electrical charge is applied and used to steer them towards their sorted destination. The speed and versatility of the FACS has spawned many attempts to reduce the scale of the technology through exploiting microfluidic flow methods and has seen the development of a number of novel micro-scale cell manipulation strategies that are discussed in Section 2.6.

2.3   Microfluidics

The advent of microelectromechanical systems (MEMS), that is mechanical structures with a characteristic dimension of between $1\mu m$ and $1mm$ [28], and particularly the development of microfluidic structures has promoted great interest in the manipulation and interrogation of biological cells and processes to the ends of analysis and diagnostics [29]. A principal aim of the development of microscale biological tools and techniques is widely acknowledged to be the development of micro total-analysis systems (μTAS) or Lab-on-chip devices [30]. Reducing the scale of the biological laboratory processes has a number of advantages including reduction in required analyte and reagent volumes and reduced time for processing [31] [32]. In addition, the greater ratio of surface area to volume as a result of reduced dimension can increase the degree of sensor-surface interaction,

permitting higher resolution in the monitoring of chemical processes [33].

2.4 Modelling Microfluidic Flows

2.4.1 Microfluidic flows

As science and engineering turns its hand to the MEMS domain then the macroscale assumptions that are made in conventional mechanical theory must be tested to ensure they are applicable and valid. The reduction of fluidic systems is no exception, and much work has been done in evaluating the relevance of classical fluid mechanics to microfluidic flows. Surface tension is the most notable deviation. Acting as a line force as opposed to a body force, the surface tension force scales directly with length, which for sub-millimetre flows renders them more dominant than others such as pressure or mass [34] due to the large surface-to-volume ratio [35]. The prediction, modelling and control of surface tension forces has led to the development of modern inkjet printing techniques, a particular application of the wetting of capillary-type micro-scale structures.

2.4.2 Wetting

Following an inspection of the Navier-Stokes equations for incompressible flow, and Darcy's equation for hydraulic drag, Washburn derived the boundary conditions and subsequently an equation connecting the distance a fluid could ingress into a porous material in a given time period. The equation accounts for both pressure across the fluid plug as a result of surface tension and hydraulic drag due to the fluid plug length, and is written in equation 2.1.

$$x = \sqrt{\frac{\sigma r t \cos \theta_c}{2\mu}} \qquad (2.1)$$

where x is the distance the fluid of dynamic viscosity μ has progressed in time t into the capillary of radius r, as a result of the surface tension force (σ) acting along the channel perimeter at the static contact angle θ_c. This was derived on the assumption that porous media could be approximated to a bundle of horizontal cylindrical tubes of radius r [36], and has been successfully applied for the modelling of wetting flow into microfabricated capillaries for several applications. The Washburn equation was proven to adequately predict measured fluid meniscus position as a function of time for microchannels of as little as 1 μm in height [37]. The equation was later modified for modelling microchannels of non-circular cross section by Tas *et al* [38].

Yang *et al* [37] derive a variation on Washburn accounting for gravity driven flow and permitting the calculation of intermediate flow positions and velocities, and demonstrate its application for the determination of channel surface properties. Kemling [39] applies the Washburn model with a view to surface modulation in order to accommodate the effects of surface roughness changes. In a study of the effects of convergent-divergent microchannels Erickson, Li and Park [40] found that despite local velocity changes, the Washburn model was found to accurately predict the overall wetting time.

Finally in a study of surface tension in fine quartz capillaries of sub-micron diameters the contact angles of the fluid as derived by the Washburn equation were found to be non-linear at velocities of below 5 $\mu m/s$, and constant for all velocities above [41], and that the values for surface tension at a sub-micron scale do not differ from published bulk values. Further to this Sobolev *et al* showed that the Young-Laplace equation for calculating pressure across a liquid meniscus remains valid down to capillaries of the order of 100 nm in diameter [41].

2.4.3   Controlling Wetting

As an alternative to closed fluidic channels Bouaidat *et al* [35] put forward the concept of a low cost, low pressure fluidic network based on the control of surface contact angle (θ_c). Through creating two initimately supported, planar, parallel surfaces, one of the surfaces being hydrophobic, the other mainly hydrophobic but with hydrophilic pathways defined on it, produces an effective microfluidic channel. The result is a capillary system that does not require precision alignment for the channel formation, and a large liquid-vapour interfacial area, as a result of the open liquid sidewalls, potentially very useful for enhanced gas exchange applications [42].

More complex fluid control has been implemented through selective hydrophobic patterning of regions within conventional fluid channels. Andersson *et al* [43] employ the selective patterning processes used in microlithography to deposit hydrophobic polymer onto a hydrophilic silicon oxide substrate in specific regions within a microfluidic channel to produce valve systems. Surface wetting can also be changed through the design of channel geometry. The wetting characteristics of a surface are manifested in the static contact angle of a liquid at its interface [44], Duffy *et al* [45] use changes in channel geometry to physically offset the surface contact angle and produce burst valves based on hydrophobic transitions without the requirement for surface treatments.

2.4.4   Continuum Flows

After a system has wetted, and the effect of the fluid surface tension has dissipated, it may be considered to be in the flow regime where classical mechanics may be applied. A basic assumption of eulerian fluidics is that of the fluid being a continuum [46], an assumption demonstrated by Nguyen and Wereley [6] as being

valid for liquid flows in channels of the order of 1 μm in diameter. Hansen and Quake [33] show that, through consideration of Reynold's number (R_e), viscous forces predominate over inertial ones for the majority of MEMS scale fluid flows, with $R_e < 1$ for sub 0.1 mm flows at velocities up to 10 mm/s. Thus illustrating that, with the exception of high velocity flows, fluid flows in microscale channels are inherently laminar.

Studies have indicated wall slip effects to be negligible, entrance effects are significant and surface roughness effects can also have a great impact [47] on microfluid flows. A range of other sources for micro-scale fluid transport mechanisms including electrophoresis and electroosmosis are discussed by Molho *et al* [48] and the generation of microfluidic pressures by way of pumping techniques are thoroughly covered but found to be lacking in all but a few specific applications in a review by Laser and Santiago [49].

2.5   Measuring Micro-Scale Fluid Flows

Although there are areas of consistency between micro-fluid and conventional bulk fluid flows [50], there are also regions of stark contrast. Differences in flow patterns between multiphasic flows, and unbalanced shear stresses in miscible fluid flows have all been observed. As such it is difficult to explain certain microfluidic dynamics by using conventional theory, and therefore, experimental approaches to the study of microscopic flow are very important [51]. Microscale flow observation continues to play a central role in the development of the field of microfluidics, with direct flow visualization of key importance for the fundamental understanding and analysis of microflows, and the development of novel microfluidic processes [52].

Particle image velocimetry (PIV) is a widely employed technique for visualising fluid flow vectors of fluid particles, and it is a method that has seen, and continues to see, significant development [52]. Through dosing the working fluid with neutrally buoyant particles precise flow measurements can be made by observing the particles optically, as opposed to the insertion of mechanical probes that would destroy device function or introduce peturbations or disruptions to the fluid flowfield [53]. It may be argued that the introduction of the particles changes the very nature of the fluid. A pure liquid, that is one that does not contain particulates or mixed emulsions, can be assumed to be Newtonian as they have a constant coefficient of viscosity, that relates the magnitude of viscous drag losses to the fluid velocity. The addition of sufficiently large numbers of particles affect this assumption as the density and viscosity of the fluid can vary depending upon the distribution of the particles within the suspension. Koutsiaris *et al* [54] however report on an agreement between Newtonian fluid models and PIV for the measurement of velocity fields within 200 μm diameter glass capillaries when using a

liquid suspension of 10 μm diameter microspheres.

The application of PIV as a flow imaging technique is of course subject to the size of the particles used. Devasenathipathy *et al* [50] stipulate that for PIV, particles should be small compared to the dimensions of the microfluidic channels, and much smaller in size than the distance over which any spatial velocity gradients will be measured. This is not to say that the smaller the particle the better the results. When particles become sufficiently small, particlefluid interactions give rise to random particle movement, preventing the particles from faithfully following the flow [55]. A compromise is required, whereby the particles must be small enough to avoid clogging of the flow field but also be large enough to be adequately imaged and to dampen the effects of Brownian motion [56].

One of the earliest examples of imaging microfluidic flows with particle suspensions was presented by Santiago *et al* [56] and involved the use of 100-300 nm particles flowing around a microfabricated elliptical cylinder of some 20×25 μm, etched to a depth of 30 μm. Imaging was conducted through fluorescent excitation of the tagged polystyrene particles and captured via a ccd camera through a $100\times$ objective, with an inter-frame capture time of 64 ms. The delay was a result of the relatively large image area and low intensity of the emission of the microspheres, a consequence of ther small size, but this permitted the imaging of bulk fluid flows up to 50 $\mu m/s$.

2.5.1 Micro-PIV in Confocal Microscopy

Extending beyond the 2-dimensional limitations of the optical microscope can be facilitated by the use of a confocal microscope. The confocal microscope employs a pinhole positioned before the image sensor in order to attentuate any out-of-focus incident light or information (figure 2.2). Through changing the position of the sample, or that of the objective and pinhole, the sample can be sectioned optically with a resolution dependent upon the size of the pinhole and the numerical aperture of the objective lens (figure 2.3).
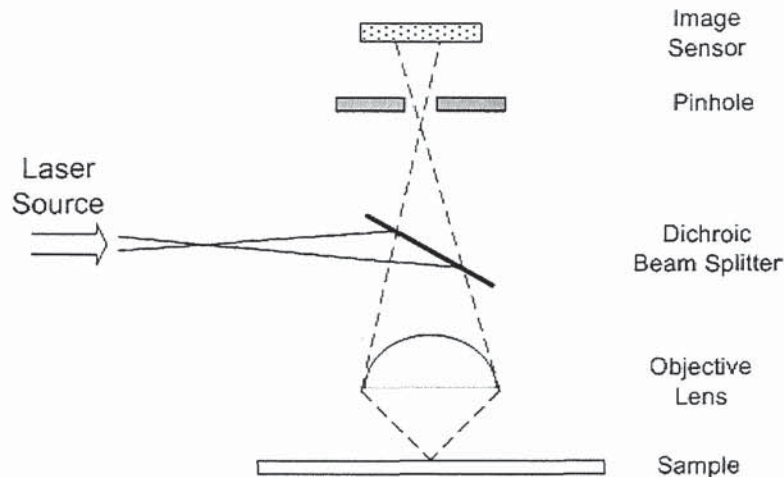
Figure 2.2: in confocal microscopy, a pinhole is used to block any out-of-focus information from reaching the image sensor

Lima *et al* [57] exploit the optical sectioning capabilities of confocal microscopy in order to create 3-dimensional images of a particle and blood suspension flow through a microdevice. Using a modified confocal microscope with a spinning disc comprised of 20,000 lenses and matching pinholes permitted the rapid collection of a vast number of 2-dimensional images across the depth of the micro-channel. Through this technique flows were successfully imaged within a microchannel of
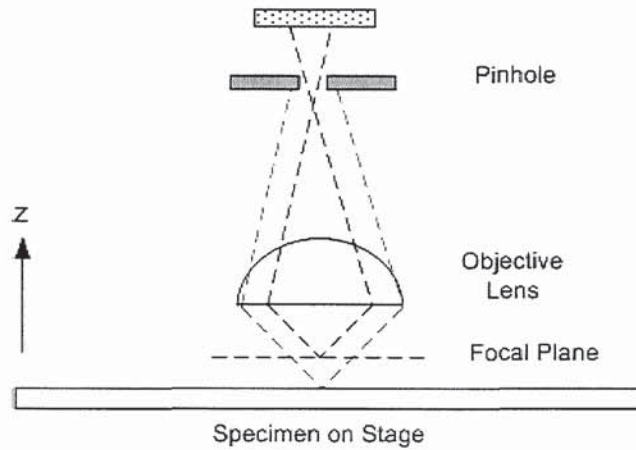
Figure 2.3: changing the position of the focal plane within the sample, transparent samples can be sectioned optically through the exclusion of unfocussed information

100 μm characteristic dimension at rates of up to 0.52 mm/s in a blood cell fluid suspension.

Aside from the collection of multiple optical sections throughout a sample, the focal exclusivity of the confocal imaging process enables the user to select a single focal plane from which to capture data. Used in conjunction with a tuned laser light source highly specific 2-dimensional fluorescent images can be constructed. Chao *et al* [53] use this capacity in order to isolate sample illumination and imaging to a 1-dimensional line mid-stream within a micro-channel, in a technique that has been termed Particle Linear Image Velocimetry (PLIV). Through imaging a line of pixels at some angle to the direction of fluid flow and measuring the time period over which the fluorescent trace of a particle is visible then the particle velocity can be inferred (figure 2.4). Although the volume of information accrued by this method is far less than that by Lima, the simplicity of the process and resulting concise datasets offer an attractive solution for μ-PIV applications.
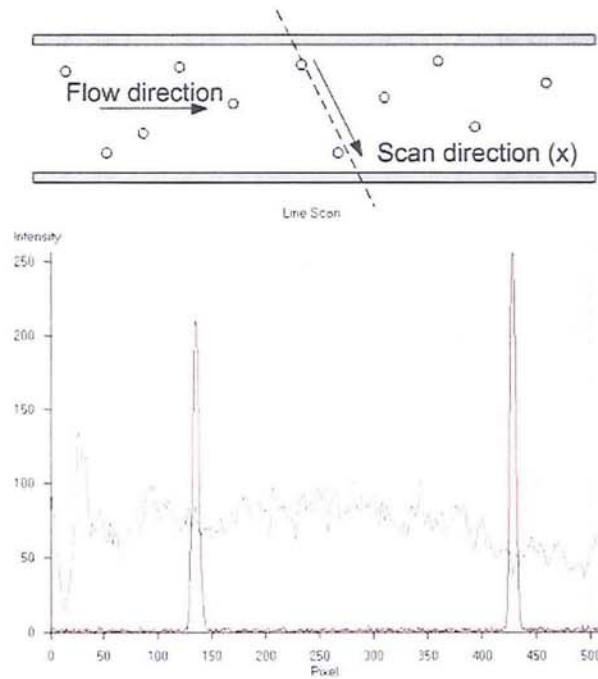
(i) imaging at an angle to
the direction of flow
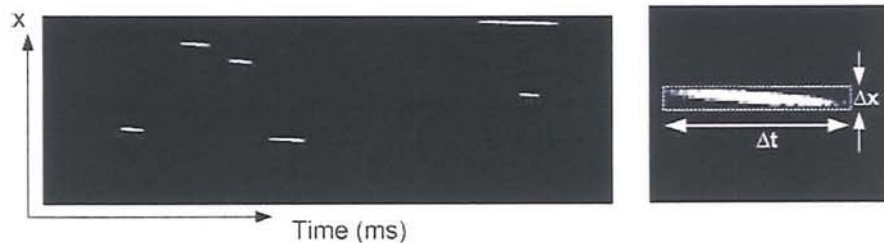
(ii) linescan vs. time returns
data on 2-D velocity

Figure 2.4: (i) imaging a line of pixels that cross the direction of flow returns (ii) a time-resolved intensity image from which 2-dimensional velocity data can be inferred

2.6 Particle Separation in MEMS

A thorough review of microfluidic cell separation technologies and their application is covered by Kang and Park [58], with descriptions and comparisons between contemporary solutions, some of which are discussed herein, along with their suitability for application in Lab-on-a-chip devices.

FACS devices offer impressive separation statistics for large eukaryotic cell populations, providing high accuracy at high sorting speeds, they are however cumbersome and expensive systems in terms of capital purchase, operation and maintenance, and typically rely upon attaching fluorescing stains or markers to the living cells. Fu et al [59] derived a smaller microfluidic cell sorting apparatus, operating on similar detection principles, which employed microfluidic flow switching as the mode of cell sorting. This is in contrast to the droplet based electrostatic deflection method employed within the conventional FACS [27]. Benefits of this microfabricated fluidic channel solution over the conventional air-borne droplet method are cited as being increased robustness of measurement and deflection mechanisms, and reduced risk of sample cross-contamination and backflush into successive sample streams. In addition, a single-use glass or polymeric microcapillary structure can drastically reduce the time required for sterilisation between tests.

The degree of sensitivity of the microfabricated FACS (μFACS) has been demonstrated to permit the sizing and sorting of DNA molecules based indirectly on their individual length through the intensity of fluorescent emission [60]. Microfluidic sorting devices have also been used to facilitate sorting of unlabelled cells from a continuum. Chen et al [61] describe the development of an active microfluidic switch that uses an extension of a fluid sheathing technique used in

42

conventional FACS cytometry in order to steer the bulk fluid trajectory. Through differential pressure control of two sheathing fluid flows, creating laminar boundary layers adjacent to the analyte fluid flow, the bulk fluid mixture can be steered into 2 or more collection chambers or outlets. The device and method can be applied to sorting fluorescence stained cells or large cells such as embryos when combined with suitable sensing apparatus. This and similar attempts to reproduce the performance and behaviour of the conventional FACS tend to rely upon a wealth of external processes and pressure sources [62], but enjoy benefits from the micro-volume sample and analyte sizes, and implicit laminar flow profiles inherent in microfluid processing. FACS replicates also have a certain degree of versatility in the range of cell sizes and types they can accommodate. However, providing that a more controlled range of cells or filtrate particles are acceptable then more simple solutions perhaps become available.

As an alternative to adjusting bulk fluid pressures, a means of manipulating cells in a suspension through the generation of micro-pressure gradients is demonstrated by Harris *et al* [63] whereby particles are switched between two outlets through ultrasonic excitation of a controlled region within a continuous fluid flow. Ultrasonic actuation is also employed by Petersson *et al* [64] whereby a standing acoustic wave forms static pressure nodes and antinodes inside a microfabricated channel, at which particles congregate and are effectively separated whilst the particle-free fluid continues to flow. This method has been proven to be 80% successful for the separation of lipids from milk flows, and blood flows, within a 350 μm wide channel, and with separation efficiency being inversely proportional to flow velocity. The applied frequencies are stated as being consistent with those used in diagnostic ultrasound processes and as such are currently understood to be undamaging to the processed cells. Both techniques demonstrate great promise

for the filtration of fluids, but there are limitations. In the case of Harris, fluids can only be cleaned of particles and debris with complex sounding-chamber design and precision ultrasonic transducer control. The Petersson method is more versatile providing separation for fluids containing one or two components, but the components must behave differently at the nodes and anti-nodes of the standing wave in order for the process to be effective. It would seem that the cells have to be fundamentally different of materials such as lipids and blood cells. Based on this principle it is difficult to fractionate cells that have more subtle differences in size or morphology [58]. In both cases multiple stages may be required for more complex suspensions. Furthermore, there is at present a great deal of off-chip control required, in both flow control and acoustic wave generation [65].

MacDonald *et al* present a micro-sorter that employs optical waves, exploiting the same principles as those found in laser-tweezers [66]. A configurable 3-dimensional lattice pattern is generated by interfering five laser light sources in the flow region of a microchannel. Cells or particles flowing within the fluid are then sorted based on the strength of their physical response to the lattice, as a result of their size, refractive index or shape. The technology boasts separation efficiencies in excess of 95% and as such its application to particle sorting is promising, but the considerable overheads and required ancillary sources of both fluid and optical power are daunting.

Brody *et al* [1] describe the development and manufacture of a planar microfabricated fluid filter for the purpose of separation of cells or particulates based on size from a suspension via a 'tap' that acts tangentially to the direction of fluid flow. A degree of external pressure control is required to prevent filtrate backflow across the separation boundary and to produce shear forces in the fluid flow that act on any arrested particles and prevent blockage by washing them downstream.

The manufacture of the threshold for the tap is achieved through wet etching of a wall structure, the resultant height of which is controlled by the duration of the etching period (figure 2.5), but as such local variations in etch depth would be difficult to control thus limiting the threshold for devices on a single wafer to be of a single height.

Figure 2.5: cell selection height is governed by the wet-etching of a wall feature, etch duration controls the minimum clearance between the barrier and the lid [1]

Along a similar vein, Ehrfield *et al* [67] describe a LIGA microfabricated filtration device where the source fluid flow is tangential to the aspirated filtrate, a cross-flow microfilter, that could be applied to biological applications. The LIGA manufacturing technique promises the possibility of very fine filtration structures, of the order of $0.1 \ \mu m$. As with Brody [1] the method will suffer incomplete filtration, and numerous devices will be required to separate different cell sizes. The technique employs a comb-like filter structure that would be difficult to clean and subsequently re-use. Sufficiently high production volumes could subtend a potentially disposable device, however the moulding process would require a polymeric die material which would require chemical modification of the surface properties in order to be hydrophilic for passive flow, or a high pressure fluid source.

Regnier *et al* [68] introduce the concept of lateral percolation into planar filtration

45

structures. Cuboid projections from the substrate enable the selective capture of larger cells whilst permitting fluid and smaller particles to pass unimpeded across the surface of the substrate when a liquid suspension is added perpendicularly to the plane of filter elements. Obstruction of the flow due to the cuboid projections provide that any cells captured in this method will be difficult to extract or aspirate with conventional tools for further use. Suitable applications are therefore better orientated towards the mechanical trapping or immobilisation of cells for imaging or biochemistry, or for the preparation of finely filtered fluids where any filtered particles are not required.

This concept is elaborated upon by Austin *et al* [69] detailing possible flow obstacle element morphologies and the incorporation of a means for inducing particle migration through electrophoresis, or an applied electromagnetic field. The different pillar morphologies offer a degree of variation in the behaviour of the filtrate but their proximity and scale are comparable with the particles that they intend to immobilise, thus eliminating any controlled mechanical liberation of specific cells or particles when held within the obstacle array. Such a device, as with Regnier, could be well applied in cell immobilisation for in-situ biochemistry.

Andersson, Wijngaart and Stemme [70] present a similar technology to the same end through the fabrication of voids within a silicon substrate with barriers or fences intended to capture cells within a particular area, made viewable by way of anodic bonding to a glass cover. In the given configuration the chip is described to provide visual access to an accumulation of tagged or marked polymer microspheres without provision for retrieval. The microspheres serve to act as binding sites for biological or chemical agents upon which further biochemical reactions are conducted and the resultant effect can be visualised through some optical change. Substrate projections serve to form a permeable membrane around

an otherwise closed reaction chamber. Andersson *et al* also include hydrophobic patches within the structures to permit discontinuous flow or fluid loading through the selection deposition of the C_4F_8 sidewall passivation polymer used during the Deep Reactive Ion Etch manufacture process [43].

Kricka and Wilding [71] developed a microfluidic device for the trapping of different cell sizes from suspensions, or the separation of cells based on their motility as applied to spermatozoa. Again predisposed by the inherent layered 2D morphologies permitted by photolithographic micromachining, the device comprises an inlet and outlet that are connected by tortuous channels into which sperm cells are able to navigate, with those exhibiting higher motility reaching an oocyte repository where fertilisation can occur. The authors then went on to develop a variation on the device for more general continuous flows of fluid-borne particulates whereby projections from the substrate are designed to inhibit particulate flow from fluid suspension [72].

A continuous white blood cell separation and fractionation method is put forward by Carlson *et al* [73] whereby whole blood is drawn by suction through a number of densely populated parallel 'strainers' etched to a depth and width of $5 \ \mu m$ in an attempt to mimic biological capillary structures. Chamber sealing is effected by the application of a removable elastomeric membrane providing subsequent probing of trapped cells and further processing following cell adhesion to the filters. The actual liberation of individual cells or groups of similar cell types from the filter network would not be possible without highly specialised tooling that permits sub-micron positional accuracy and end effector or manipulator dimension. Without exception these techniques employ directly or indirectly an

external source of pressure or motive force, assuming one or more configurable and controlled sources of fluid flow. As such the majority of these technologies would serve well as incorporated into a microfluidic system, but few could stand alone as a clinically applicable device.

Ohman and Mendel-Hartvig [74] present an alternative use of densely populated micro-pillars extending from a substrate in order to facilitate unpowered wetting and introduce a means of inducing fluid flow in microfabricated lab-on-chip devices, thus negating the need for external pressure sources or similar fluid driving effects. Given such a configuration, however it is worthy of note that inducing flow beyond the capillary wetting structures would be difficult without the incorporation of some hydrophilic gradient. A membrane is supported above the capillary elements but not in contact with the fluid. Fluid volume is limited to that which can be supported within the limits of the wetting structures, minus the volume of the structures themselves. Ohman *et al* indicate the possible use of these structures as a means of arresting cells and organisms according to their size or rigidity.

Such a format would provide little benefit for the given problem as they have a low volumetric capacity for a comparatively large spatial distribution, and afford little opportunity for the retrieval of trapped cells. Furthermore, without a means of controlling fluid evaporation or systematic rehydration, the low volume and large area of the liquid-air boundary could suffer significantly from fluid loss and cell damage through dehydration.

It may be considered that the Ohman device is a derivation of a mechanism proposed by Lopez *et al.* This mechanism relies upon a regular array of cylindrical projections extending from a substrate varying in pitch or diameter of sub-micron

dimension through which a fluid analyte can be passed. The projections change gradually across the plane of the device providing a gradient against which a biomolecule can be separated chromatographically [75].

2.7 MEMS in Biology

In their review of microfluidic separation devices Kang and Park [58] make the observation that amongst the solutions under development, the most influential factor on the selection of fractionation mechanism should be that of the aim of the process. That is to say, physiological viability of the cells is more important than cell viability to researchers with regards to clinical diagnostics or cell population analysis. However, preservation of cell viability is of primary importance for subsequent biological studies or processing of the cells, and of particular importance to ART cell pre-processing.

For the deployment of MEMS devices in biological applications (Bio-MEMS) beyond pure diagnostic cell isolation then the nature of the working fluid and the filtrate may be considered to be extremely sensitive to either mechanical or chemical harm. The nature of silicon, the most widely applied MEMS material as a result of the momentum of the semiconductor industry [76], makes it especially suitable for such applications since its surface characteristics, such as hydrophilicity and roughness, can be precisely tailored during the etching process thereby minimising the degree to which proteins and biological structures adhere, or are denatured upon contact [77]. Furthermore, Weisenberg [78] conducted a study on the interaction of common MEMS materials with blood chemistry as a biological fluid and found that native silicon dioxide demonstrated low cellular adhesion indicating its viability for biological applications.

Cleanliness and sterility are vitally important to the practicing clinician in all fields of medicine. Although the chemistry involved in the manufacture of MEMS structures is aggressive and toxic to life [79], providing sufficiently effective cleaning and decontaminating processes are employed the high temperatures, inert atmospheres and cleanroom conditions in which MEMS devices are fabricated make subsequent sterilisation procedures unnecessary. Furthermore, the low potential unit costs afforded by semiconductor fabrication processes and the ubiquitous raw materials make MEMS structures and products viable candidates for single-use and disposable applications [80].

2.8 SUMMARY OF REVIEWED WORK

2.8.1 Microfluidic Flows

In general, microfluidic flows have not had the same rigourous study as macroscale systems, and as such are typically assessed empirically. Current understanding of microscale liquid flows reveal them to be inherently laminar at all but the highest of velocities and largely subject to fluid mechanics modelling assumptions down to sub-micron channel dimensions. The most widely applied and accepted means of observing and empirically measuring fluidic flows on a microscale is that of particle image velocimetry, whereby particle suspensions are used as the working fluid and the motion of the particles is used to infer the motion of the fluid. Adding particles to the fluid potentially negates the fundamental Newtonian fluid assumption of classical fluid mechanics, but PIV is nonetheless an accepted analog of a fluid particle's motion and is found to be in approximate agreement with Newtonian fluid models for low particle concentrations.

Microfluidic flows can be imaged with a conventional microscope, however a confocal microscope can restrict image planes to specific regions of fluid flow, i.e. the centre of a fluid conduit, or closer to a channel wall in order to observe boundary effects. Extravagant modifications to the microscope can permit the rapid imaging of a liquid flow in 3-dimensions, however innovative use of the unmodified microscope can also be used for successful flow imaging, with a considerably lower data processing overhead.

Conventional macro-fluidic models have been successfully applied to microscale flows, however the bias of flow source shifts from bulk forces to surface forces as the scale decreases. Small scale flows are recent, lacking the wealth of analysis and understanding of conventionally scaled flows, as such there is still a heavy

dependence upon empirical data, typically collected through non-contact optical interrogation of flow markers or particles occupying a small fraction of the flow dimension.

In the reviewed literature there were many identified studies on the characterisation of wetting fluid flows, and continuum fluid flows, but a comparison of the two has not been made. Simililarly there have been numerous studies of the measurement of continuous microfluidic flows with PIV techniques, but there are no examples of the measurement of wetting velocities beyond total wetting times, and there have been no attempts in the available literature to employ particle velocities in suspension during the wetting phase in order to determine wetting velocities within a complex system.

Furthermore, efforts have been made to discretise the Washburn, and similar, wetting models in order to determine quasi-static meniscus position versus time and to use this relationship to identify immeasurable surface properties or energies, but these methods have not been extended to the prediction of flow velocities in non-uniform micro-channels. There remains a need for the model to be applied and experimentally validated for this purpose.

2.8.2 Surface Effects

Due to scaling laws surface effects are more dominant than bulk fluid effects, consequently the wetting phase of fluid flows are crucial in the success of a microfluidic system. This has been exploited in the creation of passive valve structures, the production of large liquid-air interfacial areas, and general selective wetting applications, through the deposition of wetting and non-wetting surface layers, or the control of surface geometries. This manner of fluid control has great potential for passive and non-passive μTAS systems, but is mostly widely applied in the

formation of barriers to micro-scale fluid flow.

2.8.3   MEMS Particle Separation Solutions

The current state of the art in microfluidic particle separation is largely based on the use of channels populated with projections acting perpendicularly to the plane of fluid flow. Flows are typically constrained within composite channels comprising a substrate and sealing lid or membrane, and between inlet-outlet pairs across which a pressure differential is externally applied. Other methods of inducing fluid flow are widely explored but for the purposes of particulate separation few other alternatives have been implemented. Little has been done on post separation processing as so far as the retrieval of filtrate components, only the removal and isolation of undesired particles from a continuous flow.

Existing microfabrication processes predispose filtering element geometries to two dimensional forms extruded from the plane of the base of the channel. Self-powered fluid progression through capillary action has been implemented on a microscale and nanoscale with a view to chromatographic applications, but subsequent access to filtered particles has not been achieved in the reviewed literature. The self-powered wetting devices covered in the literature rely upon a large surface area in order to maximise the capillary effects, but in several cases this results in a large liquid-air boundary, which with small fluid volumes provides capacity for rapid fluid evaporation. This effect does not appear to have been identified, nor has a means of mitigating it been presented in the reviewed literature.

2.8.4   Conclusions

Currently, of the available or published devices or processes, no devices satisfactorily address the needs of the stated problem, requiring a heavy requirement for ancillary equipment or providing poor access to the filtrate. However, with the application of existing principles and techniques a solution is possible that will provide a separation platform suitable for deployment into an existing biological laboratory.

Chapter 3

Design and Manufacture

This chapter serves as an introduction to the design of MEMS and microfluidic devices, the process steps and in particular the constraints of designing for lithographic microfabrication techniques. Initially there is an exploration of the current methods employed in spermatogenic cell dissemination, the scales of the biological structures, populations and potential barriers to alternative separation methods. There is then a summary of the salient points in the form of a specification for the devices and a discussion of the design criteria. An overview of the design concept and the principles it was founded on are presented, including thoughts on the source of fluid motion and layout considerations. This is followed by a study of applicable filtration and segregation solutions and an appraisal of their integration into the cell separation device.

There is also a brief introduction to the available manufacturing processes and their limitations, specifically Deep Reactive Ion Etching (DRIE), and a discussion of the constraints of designing for lithographic microfabrication processes, highlighting the requirements of the design aspects required for successful construction. The process flow for the manufacture of the device is presented and

discussed in the context of production considerations. Each device chip design is presented with reference to the application and manufacturing considerations taken into account. Finally there is an evaluation of the final devices as far as their yield in the DRIE foundry and the lessons that were learnt from the outcome of prototype production.

3.1   Round Spermatid Injection

The advent of intracytoplasmic sperm injection (ICSI) has provided a means by which the most severe cases of male factor infertility can be treated and overcome to the end of successful conception [14]. Spermatogenesis, the process of male germ cell development, occurs within pyramidal structures in the testes referred to as 'seminiferous tubules', and are indicated in figure 3.1. The stages of spermatogenic cell development are illustrated in figure 3.2. Following the development of spermatozoa the cells migrate along the 'vas deferens' in preparation for ejaculation. The condition where there is a lack of spermatozoa in the ejaculate is referred to as 'azoospermia', which can be divided into two basic categories: *obstructive* and *non-obstructive azoospermia*.

Treatment of the latter requires the harvesting of cells from the testis direct by way of a testicular biopsy, but in such cases the probability of finding spermatozoa in the biopsy is low [8]. An alternative approach is to use spermatozoan precursors, or immature germ cells such as round or elongated spermatids for injection into the oocyte and bring about fertilisation [81]. These processes are referred to as round spermatid Injection (ROSI), round spermatid nucleus injection (ROSNI), and elongated spermatid injection (ELSI), and all have seen varying rates of success in the procreation of healthy offspring [81].

Figure 3.1: schematic diagram of the biology of the human testis indicating the site of germ cell manufacture, the seminiferous tubules.

Sperm cells can be recovered from the testis through a number of methods as shown in figure 3.3. However in cases of severe non-obstructive azoospermia cells are required to be harvested from the seminiferous tubules through a testis biopsy in a process similar to testicular sperm extraction (TESE) (figure 3.4).
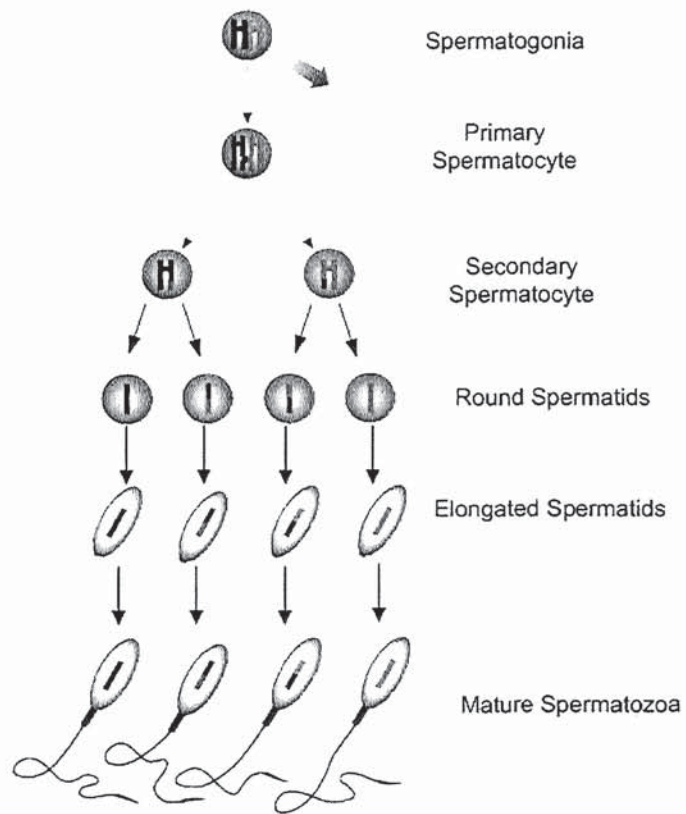
Figure 3.2: developmental stages of spermatogenesis beginning with spermatogonia (top) and resulting in mature spermatozoa (bottom)

Figure 3.3: a survey of the available sperm recovery methods: percutaneous epidydimal sperm aspiration, testicular sperm aspiration, spermatocele aspiration, microsurgical epidydimal sperm aspiration, testicular sperm extraction from biopsy, and vas deferens aspiration [2]

Aston University

Illustration removed for copyright restrictions

Figure 3.4: recovering spermatogenic cells from the testis through biopsy (TESE) [3]

3.1.1 Cell Separation for Spermatid Injection

Numerous tissue samples can be obtained from testis biopsy sites across multiple regions of the testis as necessary [14] that must then be processed in order to obtain a single cell suspension of desired cell types. The most common method is one of mechanical mincing whereby the biopsied tissues are teased apart with sterile glass slides to identify individual tubules followed by mechanical mincing with surgical tweezers (figure 3.5) and needles prior to inspection for spermato-genic cells (figure 3.6) [4]. In the event that the desired cells are not located within the biopsy a further biopsy from an alternative site on the testis must be taken.

Figure 3.5: extracted seminiferous tubules are dispersed using glass slides and manually minced using surgical scissors [4]

Figure 3.6: tubules being dispersed beneath a microscope using needles prior to cell selection [5]

Spermatogenesis can be divided into three major developmental stages based on the cellular changes that occur:

1. The first cell division of spermatogonia to form two primary spermatocytes

2. A further cell division from primary spermatocyte, through secondary spermatocyte and into round spermatid

3. spermiogenesis - spermatids mature into elongated spermatids (lacking a tail) until the final stage of fully mature spermatozoa [82]

Only the cells from the last stage have sufficient genetic material in order to provide offspring. Available data on typical cell quantities representative of these stages obtained in biopsies for both normal and non-obstructive azoospermic males is presented in table 3.1. The figures represent normalised cell populations per gram of testis sample, a quantity much in excess of the normal testis tissue biopsy which is typically of the order of 50-100 mg [4].

Table 3.1: typical cell quantities, normalised per $1g$, as obtained through testis biopsy for healthy, obstructive and non-obstructive azoospermic males [7]

A number of studies on the morphology and scale of spermatogenic cells have been conducted with the intention of providing clear reference marks for the purposes of identification [81]. As such the approximate sizes of the cells may be summarised as in table 3.2.

Table 3.2: typical cell dimensions and their approximate population of total cells per $1g$ of testis biopsy tissue. [7] [8] [9]

The manual mincing technique liberates a number of the cells within the seminiferous tubules, and has the advantage of obtaining an assortment of spermatids ready for immediate use [7] but the onus is on the clinician to identify and isolate them from the other cells and tissues. The standard laboratory process is summarised as:

1. testicular tissue placed in Falcon 2003 tube containing 2 ml of gamete 100 medium, tubules are teased apart and progressively divided into small segments.

2. tubule segments are gently crushed between 2 pincettes in a petri dish containing gamete 100 to obtain a suspension

3. suspensions transferred into a falcon 2003 tube and rotated for 50-60 s with a vortex mixer

4. samples examined at 200-400× magnification under a Hoffman modulator mounted inverted microscope in a Falcon 3802 petri dish containing 5 ml medium.

5. if cells are observed suspension is centrifuged on a two-layer Percoll gradient (70-90%) at 300 g for 20 minutes.

6. cells are kept incubated at $37°C$ until the ICSI procedure.

7. spermatids are aspirated from the pellet or percoll suspension with a 10 μm diameter pipette and transferred into the injection dish (Falcon 1006) containing a 5 μl droplet of Gamete 100 medium.

8. spermatids are aspirated one by one from the droplet and transferred into a droplet of ICSI 100 and injected into the oocyte with a 7-10 μm needle.

[83]

3.2   Design Specification

The devices are intended as a prototype suitable for deployment within a standard ICSI capable andrology clinic or laboratory with a minimum of ancillary equipment, and providing a fast, low cost, and low skill solution to replacing the existing manual process of cell presence determination or cell selection. Intended for the separation of dissimilar spermatogenic cells, with a view to adaptation for other applications, there must be some process by which cells are removed from a mixed population, or by which the local concentrations of cells that can be found are increased. In order to offer time benefits over existing methods there should be clearly distinct regions that offer an elevated probability of finding a particular cell type.

For the target application of ART the mechanism of separation should cause no chemical, thermal, biological or mechanical damage, nor should it pollute or in any way render the filtrate unsuitable for later in-vivo use [7]. The separation mechanism should be optimised for the separation of useful components of the filtrate from non-useful components. Useful post-separation cells or particles should be accessible and ultimately removable from the device without causing harm to them, or adjacent cells, held in suspension. The devices should integrate within the clinical environment without impacting on other processes or facilities. Finally, the devices should be capable of being cleaned, sterilised, or made disposable in order to avoid cross-contamination of samples.

3.3   Design Concept

The scale of the testis samples, and their constituent cells (table 3.2) and particulate bodies involved in preparation of male germ cells for ART predisposed the solution to be one of applied microtechnology. A solution that was felt to best fit the design specification whilst being robust and simple to manufacture was one of monolithothic construction. Comprising a central liquid reservoir and a number of access wells connected by fine channel structures populated with filtration elements, a schematic of which is provided in figure 3.7. A morphology for the system was devised that made use of the physical forces available on the microscale in order to produce the most reliable method of fluid control and maximise the potential of the device. As such a gravimetric head was introduced between the central reservoir and that of the fluid flow channels, and the channels were intended to provide rapid fluid through capillary imbibition.

Crafting the initial fluid reservoirs and access wells from the same substrate as the channels provided a potential cost reduction through optimising material use and reducing the number of etch and alignment processes involved in the manufacture. The open surface-etched channels are sealed through anodic fusion to a glass wafer, providing an imaging window for the clinician to view cells in suspension, whilst limiting the opportunity for contamination to the access wells. Manufacture was planned to be a two-mask process via DRIE, with a simple process flow and few wafer handling operations prior to the glass bonding. In order to achieve this a novel manufacture method was pioneered and developed with Dr. P.T. Docker at the University of Birmingham, and subsequently adapted by process engineers at the Scottish Microfabrication Centre (Section 1.6.2). The
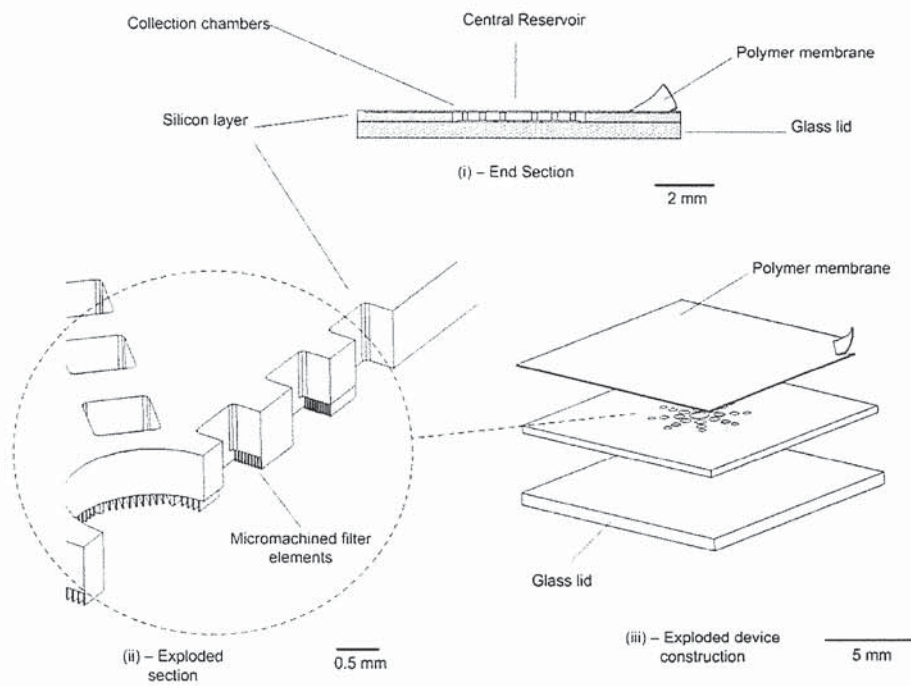
Figure 3.7: schematic indicating the format of the concept design. Linear filtration channels radiate from a central reservoir. Multiple access wells provide access to the filtrate from above, whilst viewing is permitted by the glass window beneath.

method of operation was envisioned to be as simple as possible. Cells in suspension are added to a primary reservoir from where they are drawn off and coarsely separated according to size or morphology by an array of filtration elements, leaving areas where different cell types may be located: the access wells or collection chambers. It was deemed that in the interest of speed and process simplicity it is acceptable that not all cells would be perfectly separated, nor would all cells be retrievable, as without the inclusion of some artificial or external pressure source this would be difficult to achieve. It was decided that the design specification could still be satisfied if the probability of specific cell-types being located in certain areas would be increased over random cell or particle distribution.

Access to the cells after separation would be facilitated through aspiration by micropipette of the contents of specific wells. Removing the liquid containing the cells from the wells by suction would introduce a gravity driven imbalance into the system encouraging further fluid flow from the primary reservoir to the emptying well. In this way, the act of removing calls in fluid can promote the flow of more fluid through the capillary and the separation of further cells.

Any filtration mechanism is subject to the hazard of blocking: the arresting of undesired particles to the extent that the passage of wanted particles is impeded. With a device configuration such as the one proposed any attempts to provide bypass channels would affect the primary flow and consequently be detrimental to the performance of the device, irrespective of blocking. As a means of compromise the channels were designed with a degree of redundancy. A centrally located reservoir with multiple separation channels reduces the probability of overall device failure, and each channel has multiple fluid flow paths. An initial separation stage is incorporated into the central reservoir so that cells large enough to block the channels are arrested in a region of maximum flow path opportunity. Further

to this, the channels were to be etched to a depth in excess of two maximum permissible particle diameters.

3.4 Device Function

3.4.1 Fluid Flow

Cells being processed for ART, genomics and other biological studies are typically handled in fluid. The scale of the structures involved preclude any degree of dry handling and in many cases the dehydration of a cell would bring about its death. As such the device is required to provide a haven for the cells and their liquid environment. Literature studies of microfluidic principles indicate that by far the strongest force in microfluidic systems is that of surface tension. Furthermore, the most common material for microfabrication is silicon, which is subject to the formation of native hydrophilic oxides. So by selecting silicon as the basic substrate material and encouraging the growth of silicon oxide, a surface can be cultured that is conducive to promoting rapid flow via capillary action without the need for external pumping methods.

Capillary action is not only based on how hydrophilic a material is, but it is also subject to geometrical limitations [84]. When a fluid droplet rests on a surface it exhibits a contact angle (θ_c demonstrating whether it is hydrophilic ($< 90°$) or hydrophobic ($> 90°$). Through introducing an offset of $90°$ in a fluid flow path a fluid can be discouraged from progressing in a particular direction (figure 3.8). This is exploited in the design of the reservoirs and access wells, the perpendicularity of the wells to the upper wafer surface ensures that fluid will not readily spread across the regions between the wells despite the surface being hydrophilic.
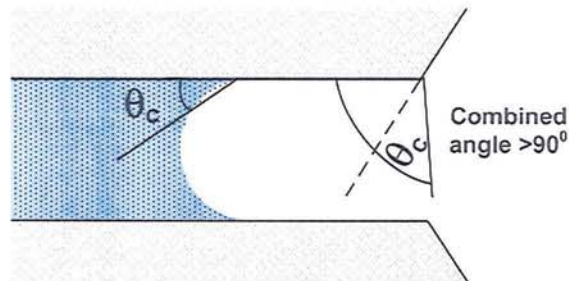
Figure 3.8: a hydrophilic surface and fluid with a contact angle θ_c can be made to behave hydrophobically through introducing an offset to this angle

3.4.2 Cell Separation

As the device concept depends upon capillary flow then the bulk of cell separation would occur within the first few seconds of the fluid being in contact with the device, asking much of any filtration methods employed. In order to offer a degree of redundancy a number of small filter channels were selected over a single larger capacity one. In this way should one channel fail to provide fluid flow then there would remain a number of others that could function correctly. Linear channels were selected in order to reduce the opportunity for fluid arrest and bubble formation. The channels connected an access well to the central reservoir, between which there were three filter stages and two equispaced additional access wells. The filter stages were optimised for the separation of spermatozoa and elongated spermatids ($< 8 \, \mu m$), and round spermatids ($< 15 \, \mu m$) from interstitial cells and debris occuring within the testis biopsy ($> 15 \mu m$). An initial filter stage of 25 μm pitch prevents the ingress of larger cells into the channels and potentially arresting the flow. To further improve particulate flow the linear channels were

designed to be in excess of 60 μm, tall enough to accomodate the stacking of cells whilst preserving acceptable morphology of the filtration structures.

3.4.3 Filtrate Retrieval

Concurrent cell imaging and manipulation requires the use of inverted microscopy techniques, whereby the cells are imaged from below and manipulated and accessed from above (figure 3.9). Applying a glass cover to the base of the filter channels provides a window through which this process can continue unaffected. As will be explained there are a number of factors that impact microfabrication through lithographic processes such as DRIE, in particular the matter of etch micro-loading. In brief, etching depends upon active gas plasma reaching the regions to be etched, the finer the features and the deeper the etch the longer the fresh gas takes to diffuse into the voids. If a large feature is placed in proximity to a much smaller feature then there is a danger of the larger feature becoming over-machined whilst the smaller feature is being processed. Conversely, larger areas require more gas in order to complete the etch, whereas smaller features require very little - consequentially smaller etched structures could be consumed whilst the larger etch is completing. Since the concept design depends upon large access holes being created through the silicon wafer and connecting to a shallow channel populated with fine structures a compromise was required between etch quality and access. This is not more apparent than in the access wells. The access wells were designed to be large enough to permit access only through micromanipulation tools, such as the 5 and 9 μm diameter micropipettes used for germ cell selection in the laboratory.
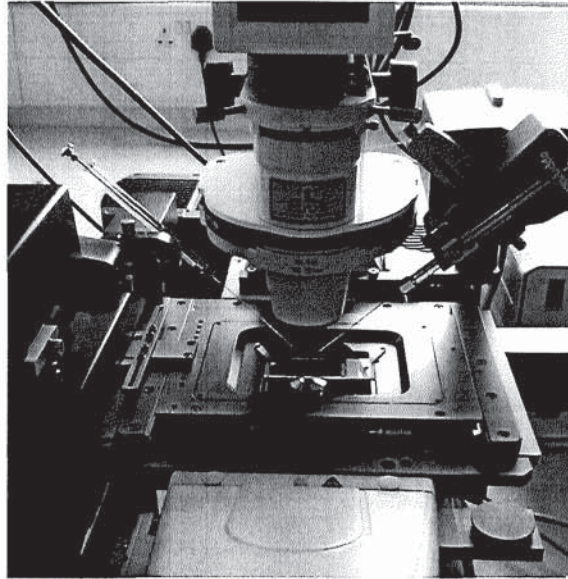
Figure 3.9: an invert microscope permits the imaging of a device from beneath whilst providing access for it to be manipulated from above

3.4.4 Process Summary

Presented here is an anticipated operating procedure for using the device as part of the preparation of spermatogenic cells for spermatid injection:

1. Preparation of single cell suspension, or collection of cell aliquot from manually minced biopsy

2. Primary deposition of cell suspension into central reservoir

3. Second deposition of flushing media into reservoir

4. After sufficient time has passed for flow to arrest mineral oil is placed over wafer surface to prevent evaporation

5. Exit wells inspected for target cells and when detected, cell suspension is aspirated from appropriate wells using a micropipette.

6. Transferral of cell suspension to micro-droplet array for cell inspection and isolation

7. Disposal of device through standard sharps and biohazard waste protocols.

3.5 Microfabrication

Having developed a concept and specification a survey of available manufacturing processes was made in order to identify appropriate techniques and any impacts that their selection would have on design details.

3.5.1 Lithography

The initial stage in an etching process is the deposition of the etch-resistant pattern, or 'resist' in order to selectively control which areas are to be etched. The photosensitive polymer resist is patterned through selective exposure to a coherent source of short-wave radiation, such as U-V light, and then developed in order stabilise the resist and remove (or preserve) exposed polymer (depending upon the type of resist). The selective patterning is achieved through the use of a mask, comprising quartz or soda-lime glass wafers patterned with chromium. Non-contact printing methods such as lithography permit the re-use of a single comparatively expensive mask in large production runs thereby introducing repeatability and the familiar economies of scale observed within the semiconductor industry.

The masks are 2-dimensional designs depicting regions to be etched, or similarly processed, and those to be left unaffected. As a consequence the structures produced by lithography may be considered to be 2.5-dimensional where the features made are linear extrusions of 2-dimensional forms. Changes in 'x' and 'y' dimensions can only be affected with etch depth 'z' through the use of additional masks. Consequently more complex geometries require more masks per die and require more dies to be sold in order to be cost-effective.

3.5.2 Surface Machining

The creation of 2-D forms on the surface of a wafer is known as surface machining, and typically refers to the creation of shallow forms on a substrate through a process of deposition, dry etching of the 2-D pattern into the deposited material, and wet-etch release. Since the forms are etched into deposited films or membranes the height or depth of any surface machined structures are limited to the depth of these films, typically of the order of 1-2 μm. The wet etching phase selectively etches only the substrate material, typically a thin layer of native silicon oxide, releasing the surface machined structures.

3.5.3 Bulk Machining

Bulk machining is usually tackled through wet-etching as it involves larger structures and large volumes of material to be removed from the substrate. MEMS materials are employed as a result of their highly predictable anisotropic etching characteristics, the nature of which is a function of their crystalline lattice structure. In the case of silicon, when considering the crystal structure, the plane intersecting the crystal with the highest atom packing density will etch less quickly than the other planes intersecting lower packing densities. The end result is a directionality in the silicon etch.

The direction of a crystal lattice is described by the miller indices, full details of which may be found in [10], but are summarised here. Consider a face-centred cubic lattice, such as the structure formed by crystalline silicon (figure 3.10). The direction of a plane intersecting the lattice may be described by its miller indices of the form (i) [100], (ii) [110], or (iii) [111] (figure 3.11). The selection of wafer orientation for bulk machining processes is dependent upon the characteristics of the final etched structure required, and are summarised in table 3.3.

76
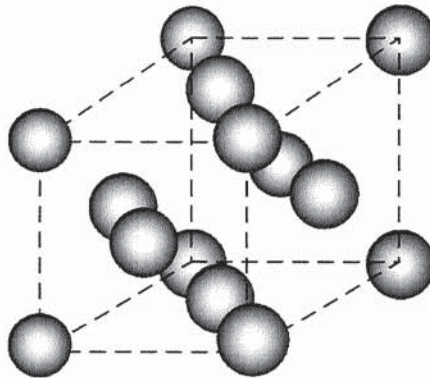
Figure 3.10: diagram of the face centred cubic lattice, typical of Silicon (Si)

[100] Si	*[110] Si*
sloping sidewalls (54.74°)	vertical and sloping sidewalls
flat-bottom cavities parallel to surface	multi-faceted-bottom cavity surface
difficult to undercut structures	undercutting readily achieved
ideal for thin membrane production	membranes difficult to achieve

Table 3.3: comparing the wet-etch characteristics of [100] and [110] silicon wafer orientations [10]
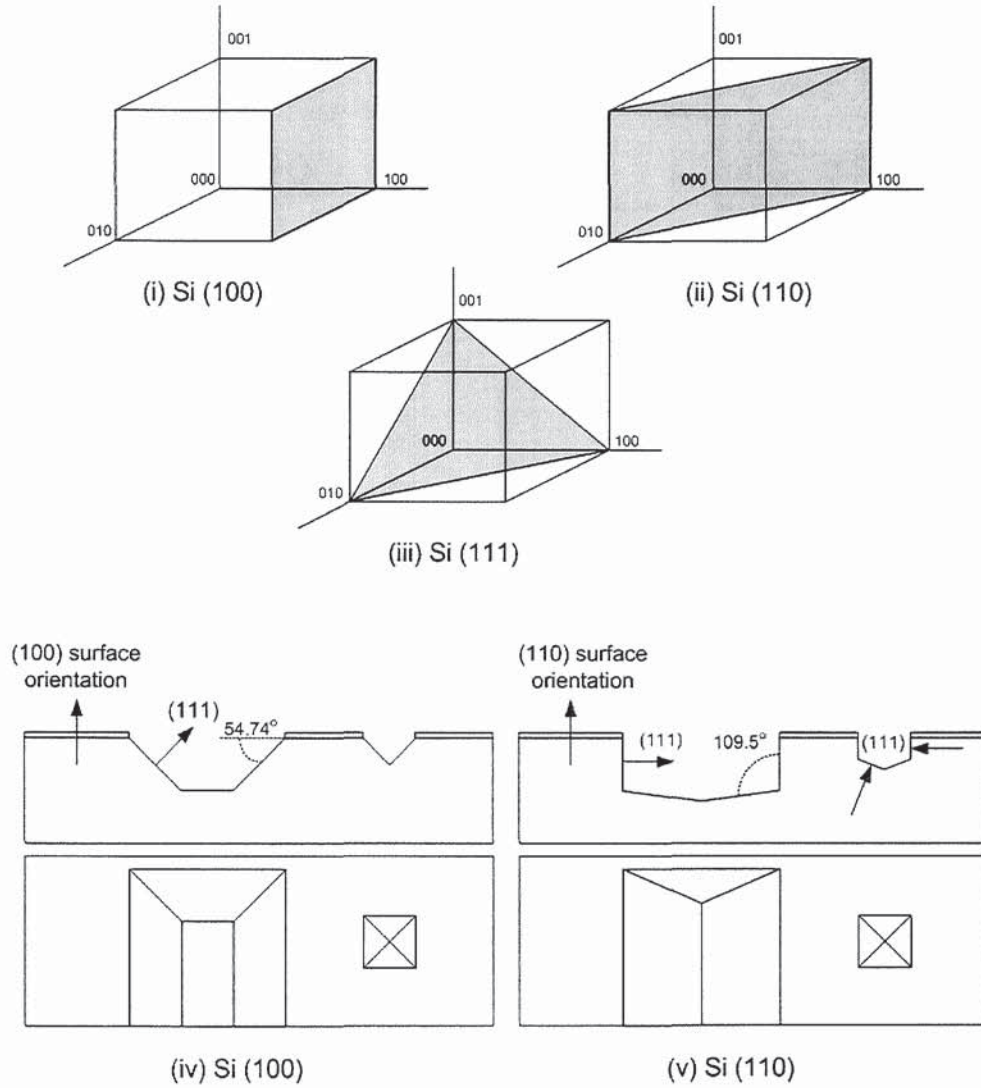
Figure 3.11: the indices of the crystal lattice within single crystal silicon for the (i)100, (ii)110, and (iii)111 planes. The effects of crystal orientation on the etched structures are depicted for (iv) 100 and (v) 110.

Considering table 3.3 it is not a simple task to select the most appropriate method for the production of the filter concept, as neither orientation offers independent control of sidewall and base geometry without imposing considerable design constraints. The anisotropic etch preference as a consequence of crystal orientation can also be observed in dry plasma etching, as employed in surface machining, but the negligible height dimension of the deposited surface layers in comparison with the other etch dimensions make any effect insignificant.

3.6   Deep Reactive Ion Etching

Acting as a compromise between surface and bulk machining DRIE, also known as the Bosch process, is an iterative process of multiple shallow dry etches in order to facilitate deep etch structures. The key to the process is the intermediate sidewall passivation cycle between successive etch stages that coats the etched surfaces with a teflon-like polymer that is directionally ablated from the base of the trench using ion bombardment (figure 3.12). This sidewall protection ensures that the base of any trenches are preferentially etched, regardless of their morphology, and permits trench aspect ratios as high as 100:1. Etch rates are dependent upon the required etch depth and the sidewall quality required, and can range from 25 $\mu m/min$ for deep coarse etches, to $< 1 \mu m/min$ for shallow and fine structures. Ultimately, the total etch depth is controlled through a combination of etchant recipe and etch duration: a deeper etch is executed through a greater number of etch-passivation cycles.
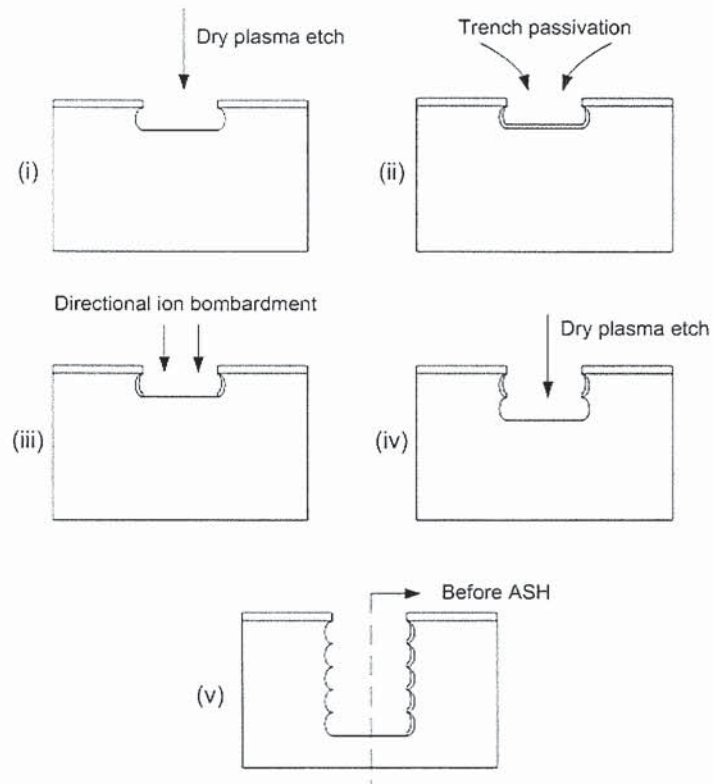
Figure 3.12: schematic representation of the stages of the DRIE advanced silicon etch process, (i) initial etch, (ii) passivation with conformal polymer, (iii) directional ablation of polymer via ion bombardment, (iv) repetition of stages (i)–(iv), and (v) polymer removal with oxygen plasma 'Ash' process

3.6.1 DRIE Limitations

There are two common problems that are experienced in the application of DRIE processing, the formation of black silicon deposits at the bottom of etched trenches, and the effects of microloading. The former is characterised by the formation of sharp black filaments producing localised non-uniformities in the bottom of deep silicon trenches. This occurs only in deeper structures and has been theorised to be a result of a number of possible causes, including

- debris or particulates as a result of insufficient cleaning prior to etching

- polymer redeposition during ablation due to excessively high ion energies

- sharpening of ion-beam angular distribution at higher trench aspect ratios

- incomplete thermal contact between wafer and cathode.

The majority of these effects can be mitigated during the etch process, however in some instances, particularly in deeper trenches, the formation of black silicon or 'silicon grass' can be unavoidable.

Etching with a dry plasma is a process in which the rate of the etch is strongly influenced by the rate of diffusion. This is to say that when a trench is etched and the plasma is exhausted, the etch process stops until fresh plasma can diffuse to the site of the trench. The deeper and more narrow the trench then the slower the diffusion process is in comparison to wider trenches and so an inconsistency in the etch rate results. This is often referred to etch micro-loading, RIE (Reactive Ion Etch) lag, or Aspect-Ratio-Dependent Etching (ARDE). A principle concern therefore in the development of structures for manufacture by the DRIE method is attempting to maintain an even balance in the etch microloading across the die, and wafer, in order to produce optimal etched feature morphology.

The versatility of the DRIE process lends itself to the rapid fabrication of complex and deep structures within a silicon substrate with minimal design complications in comparison with those of wet and dry etching. As a result, this was the chosen manufacturing method for the prototype microfilter devices, and would subsequently serve as the final criteria by which designs would be generated.

3.7 Filter Designs

In the interests of evaluating the effect of a number of differing filter morphologies and layouts, as well as exploring the capabilities and limitations of the manufacturing process a number of filter designs were generated. Several variations were generated evaluating the numerous unknown variables as a result of the design and fabrication process, in particular those as a result of the etch microloading. To aid in simplifying the modelling of the devices a number of test structures were also manufactured that could be used to verify the validity of modelling assumptions, demonstrate the capillary flow mechanism, and provide a baseline comparison for the different filter and flow designs. The device designs are presented and outlined, collated by concept type, whilst the variations on each concept were enumerated chronologically according to the order in which they were drafted. A summary of the device concepts, their features and respective fluid-flow and manufacturing considerations can be found in Appendix A.

3.7.1 Concept A

As in the majority of the concept designs a polar array design was adopted. This format offered a compromise between maximising the number of capillary channels and therefore the volume of fluid that could be processed, and providing as many flow paths as possible to the fluid. It was considered that excessively long capillaries could offer too much opportunity for suspended cells to be unprocessed through lack of motive force or other flow arrest mechanism, so the length of the capillaries was kept to a minimum. It would be undesirable if the majority smaller cells could not reach the ends of the capillaries as a result of there being insufficient periods of flow. Also, a large device area as a result of long channels would make imaging at a high magnification more time-consuming and onerous.

Research indicated a range of sizes for the spermatogenic cells of interest could be found and so three pass bands were selected that would provide segregation amongst the majority of the cell types. These pass bands were 25 μm for interstitial cells and debris, 15 μm for primary and secondary spermatocytes, and finally 8 μm for spermatozoa and round and elongated spermatids.

The capillaries were kept straight as it was felt meandering channels could offer too much opportunity for blockage and flow arresting bubble formation. This also served to reduce the length of channel between access ports thereby reducing the risk of cells being trapped between filter stages - beyond the reach of the user. An attempt was made to restrict the number of filtering elements so as to avoid excessive retardation of fluid propagation. However, in order to accommodate imbalances in micro-loading a number of larger 'balancing' pillars were incorporated. Filtration elements were positioned such as to prevent cells progressing in a linear trajectory thereby increasing the chances of undesired cells being arrested. This design was the first concept and did not incorporate any structures to prevent cells accumulating outside the reservoir and viewing ports. This was an issue addressed in subsequent design concepts.

Figure 3.13 is a schematic of concept 'A' showing the central reservoir and filter structures - including the larger etch load balancing pillars. The radiating access wells reduce in size in order to exploit Young's Law, which stipulates an inversely proportional relationship between the radius of the fluid meniscus and the interfacial pressure [85]. An SEM micrograph shows how the channels are etched vertically down into the surface of the silicon substrate whilst the filter pillars are left extending from the bottom (figure 3.14). The low resolution of the through
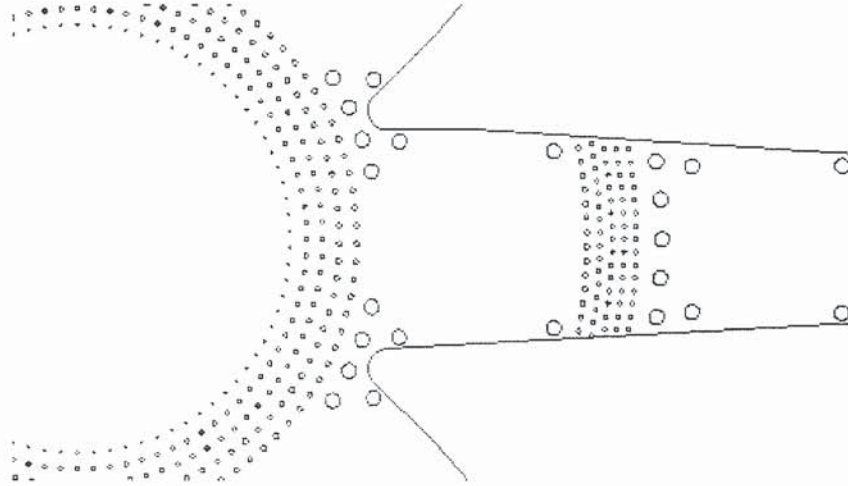
Figure 3.13: schematic diagram of Filter type 'A', with central reservoir surrounded by discrete pillars, and one of the eight-fold symmetrical tapering channels.

holes can be seen in the facetted nature of the walls, and the high aspect ratio of the filter features clearly demonstrates the capabilities of the DRIE process.
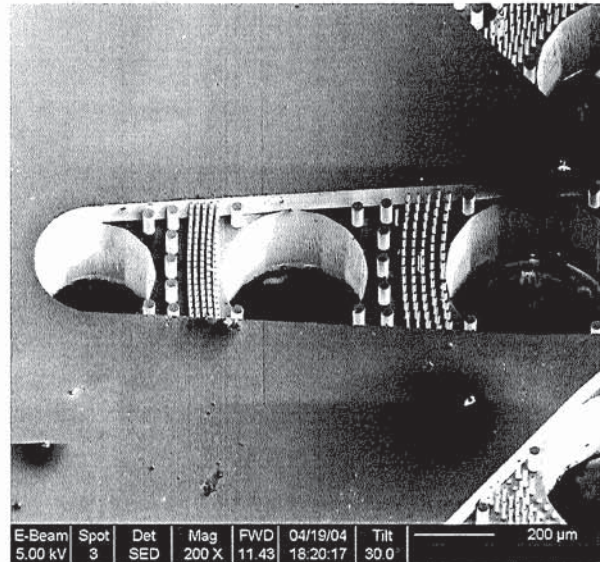
Figure 3.14: scanning electron microscope micrograph of filter 'A', the larger scale balancing pillars shown adjacent to the filtration pillars

3.7.2 Concept A2

This was labelled with the prefix 'A' as it is a variation that uses the same hole mask as 'A', but with a differing feature mask pattern. 'A2' was designed to address some of the uncertainties that arose from the morphology of the filter elements in 'A': more specifically etch micro-loading. It was unknown if the large pillars introduced in 'A' would sufficiently balance the etch-loading of the filter elements and so an equal distribution of small filtering elements was used throughout the capillaries (figure 3.15). Also, the pillars in 'A' were arrayed in an overlapping arrangement so that there was no straight path for particles between the filters, but in an attempt to simplify flow and maximise possible fluid and cell velocities an attempt was made avoid this in 'A2'. Further to this the filter elements in 'A' varied in diameter depending upon location, whereas pillar size was kept approximately constant in this revision. It was hoped that this would

further help balance micro-loading and ensure good pillar morphology throughout all filter stages.
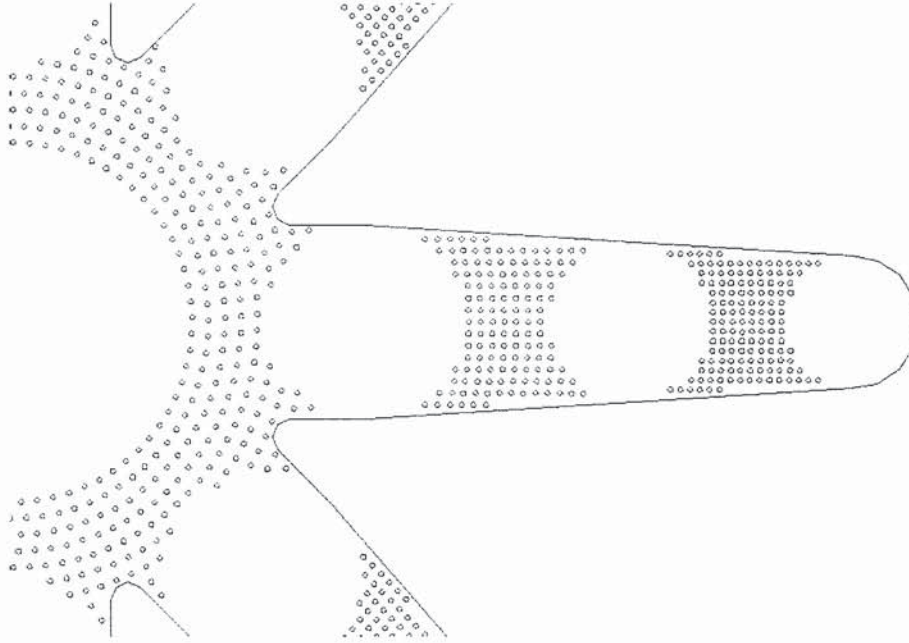
Figure 3.15: schematic of filter device 'A2'. Pillars form linear channels in order to simplify fluid paths and ensure even etch microloading

3.7.3 Concept B

As in the previous concepts a radial layout was adopted, however for this device the capillaries do not taper towards the outer access wells. This was done to increase the volume of fluid within the later filter stages. Also, rather than being equally spaced, the access ports across the final filter stage are much closer together than for the other stages (figure 3.16). This offers a degree of consistency in the number of filter steps within each stage. No balance pillars were required in this design since all areas to be bulk etched were populated with equally spaced identical structures, as in concept 'A2'.
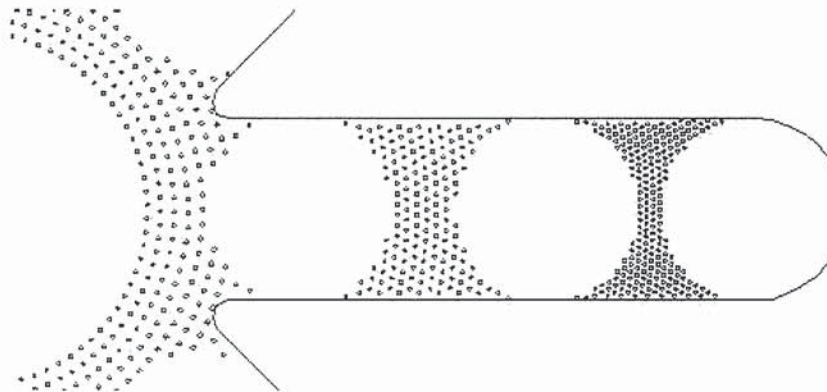
Figure 3.16: schematic of filter 'B' channel layout. Channels and access wells do not taper towards the edge of the die, and all etched areas are populated with identical filter structures.

Figure 3.17 shows the dense population of filter elements, with the density increasing with each successive filter stage. Also shown is the beginning of the final filter stage where it was hoped that the large surface area of the capillary would increase the capillary effect in the same way that the dense packing of fibrous elements in tissue paper encourages fluid absorption. Worth noting is the use of the small filter elements up to the very edge of the reservoir and viewing port

voids. This was done to prevent cells from being pushed or caused to flow out of the port and under the bulk of the wafer: out of reach of the operator. In the later filter stages the figure shows there are some pillars missing around the edges of the wells, this phenomenon is due to an early manufacturing error and is discussed in section 3.9.1.
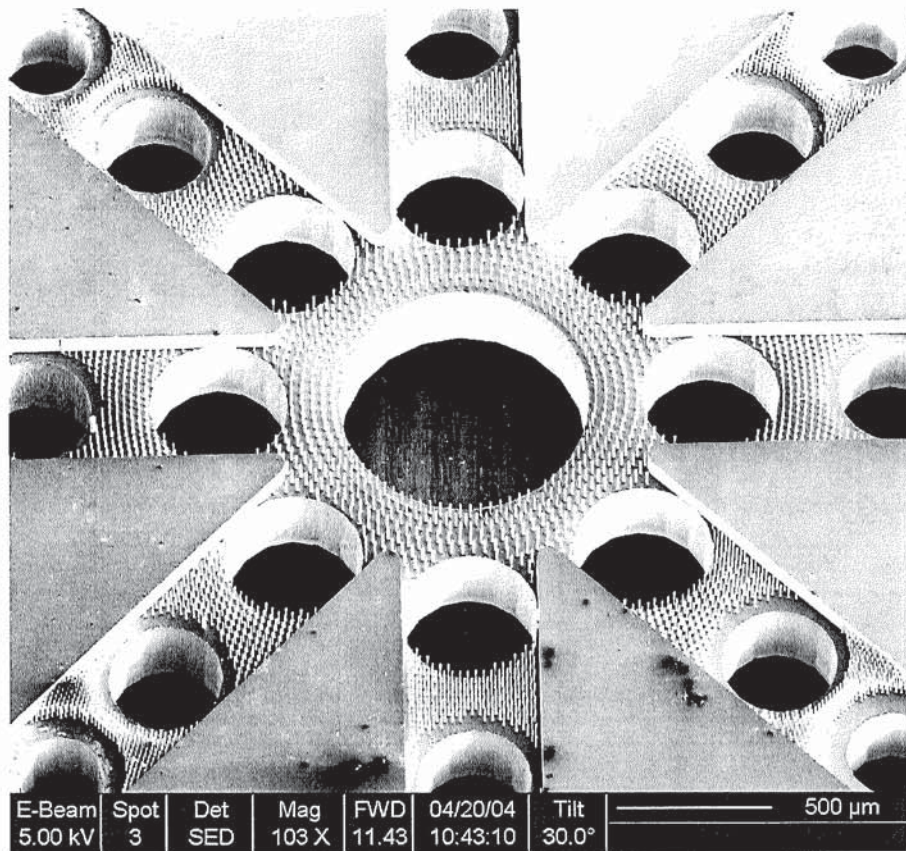
Figure 3.17: scanning electron microscope micrograph of 'B', dense populations of filter structures extend to the very edges of the access wells to avoid cells being trapped beyond the access of the operator

3.7.4   Concept B2

As with concepts 'A' and 'A2', 'B2' is a derivative of 'B' with a differing feature mask. However the primary difference here is the number of features and the filter pitch. The design was intended to evaluate the structure sizes that the DRIE process was capable of producing so a dense array of pillars of 4 μm in diameter were used for the final filter stage (figure 3.18). Further to this an attempt was made to produce very fine filtering capabilities so the filter stages were designed to filter particles of 15, 10 and 4 μm in diameter. Filtering to this degree could provide a degree of separation between spermatids, elongated spermatids, and spermatozoa respectively. However, it was anticipated that if successful the very fine spermatozoa filter may cause a navigational problem for the lengthy tail section of the sperm cells.
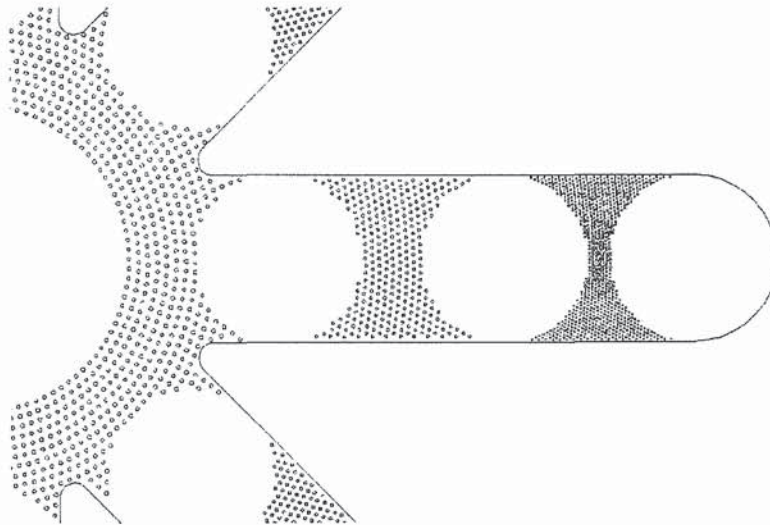
Figure 3.18: schematic of filter concept 'B2', finer filtration elements are used throughout with a reduced pitch for the intended segregation of spermatids and spermatozoa

3.7.5 Concept C

Returning to the standard filter stage pitch of $25 - 15$ and $8 \ \mu m$ concept 'C' was a departure from the curvilinear architecture of the previous concepts. The capillaries were given a direct linear form with square access ports and small rectangular filter pillars (figure 3.19). This was in response to inherent difficulties in translating curved features into discrete segmented arcs on a specified grid as required in the GDSII photomask drafting format and specified by the mask manufacturer (DeltaMask, NL). Replacing the majority of the curved features of both the hole and feature masks enabled a more rapid design generation. Another advantage was the potential for reducing mask costs: translating curved structures into linear segments requires processing time within the translation software and results in an increased conversion cost. Through avoiding round and curved features the mask required would be less expensive to produce.

Alternative port designs were explored with the use of more rectilinear voids, with the exception of the central reservoir which was maintained as a circular feature. To improve etch characteristics the sharp corners of the rectangular ports were filleted so that the etchant could more easily diffuse into the corners and provide better sidewall quality.

As in 'B2' the filter structures were distributed into equispaced rows and columns with direct particle paths through the filter stages - generated in response to concerns over etch loading and excessive flow inhibition through channel convolutions causing a lack of direct fluid flow routes.
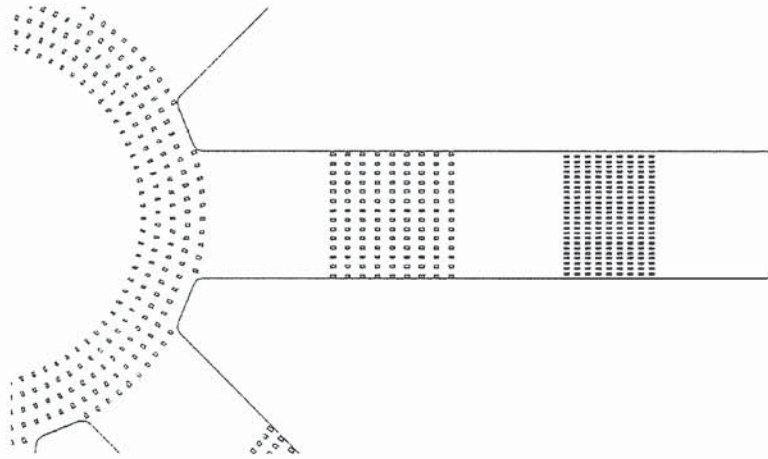
Figure 3.19: square access wells and filter elements were adopted in concept 'C', with filter structures based on a regular square pattern.

3.7.6 Concept C2
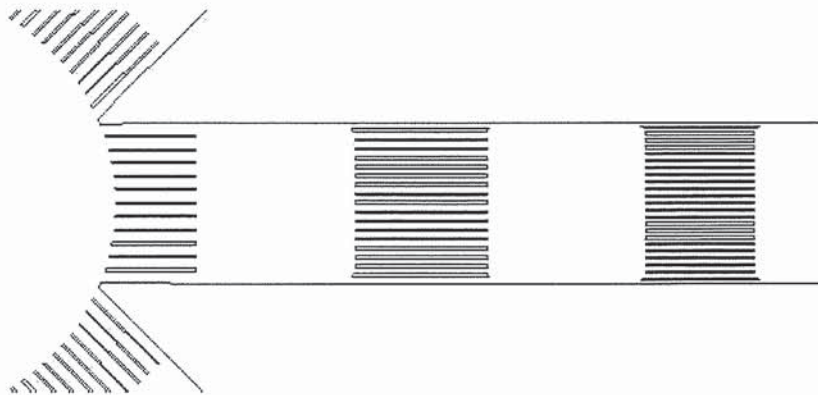
Figure 3.20: schematic of filter 'C2', all discrete filter pillars or posts are replaced with discrete linear sub-channels via fine wall features.

As can be seen from figure 3.20 the capillaries were divided into linear sub-capillaries or channels through the incorporation of fine wall features parallel to the capillary walls. The parallel channels providing a balanced etch load

and a considerably simplified fluid flow path. Figure 3.21 further illustrates the filter wall structures, demonstrating the high aspect ratios possible with DRIE etching techniques. The rectilinear features of 'C2' were also readily generated within AutoCAD because of the small number of individual filter elements in comparison with previous concepts. A concern over this design is the lack of redundant pathways for suspended particles. A single blocked filter channel in the first filter stage has the potential to reduce fluid flow in that capillary by more than 8 %.
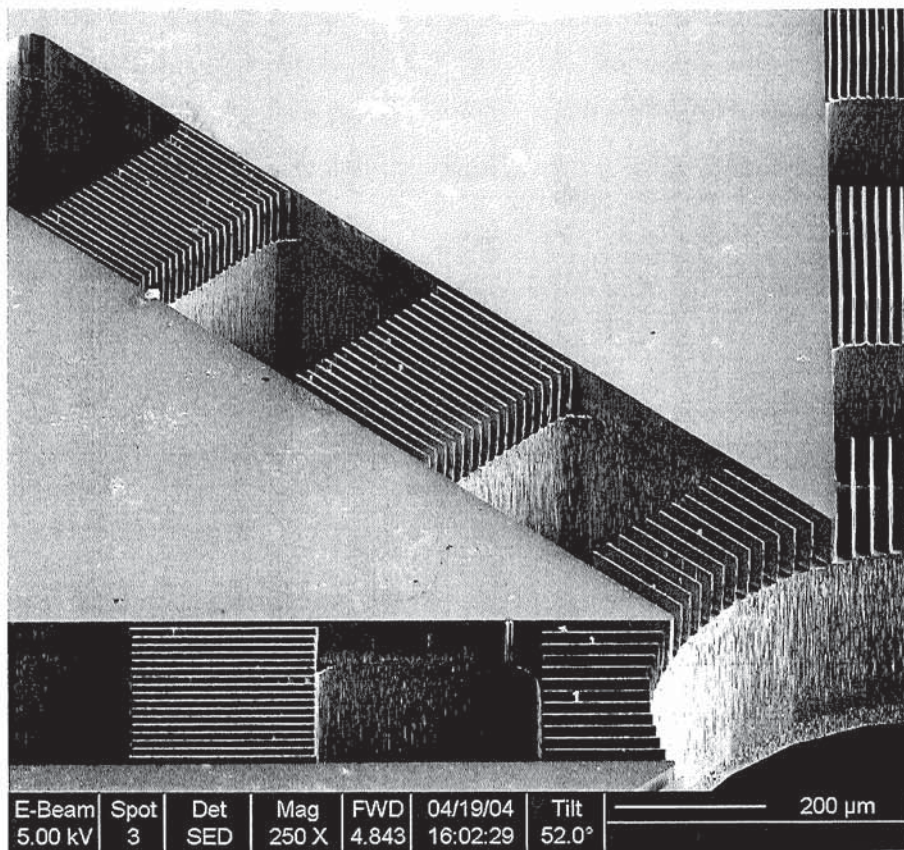
Figure 3.21: scanning electron microscope micrograph of filter 'C2'. The fine wall features demonstrate the high aspect ratios possible with DRIE

3.7.7 Concept D

This is an extravagant design intended to address the effects of blockage and saturation on fluid flow. Concept 'D' uses a central reservoir and circular sink feature (figure 3.22) with drainage paths to an external absorbent medium. The sink and drain combination was an attempt to provide a more continuous flow situation, permitting the use of larger volumes of flushing media to propagate all cells through the various filter stages. In addition to this each filter stage was equipped with multiple fluid paths to help reduce the risk of blockage. The incorporation of these paths made it impractical to have more than five capillary structures. The large areas of silicon to be removed as a result of the long capillaries and ducts were populated with large pillars to balance etch loading, and areas of fine filtration were kept to a minimum to further aid flow.

The drain feature was populated with large structures, of the type employed in concept 'A' for etch balancing, and was extended to the edge of the 10 mm chip, so that when diced it would be open to atmosphere and would permit fluid to escape, or to be drawn off.

The regions connecting the drainage ring to the final stage access ports were populated with very fine pitch filters, comprising columns of approximately 6 μm in diameter with a 3 μm inter-pillar spacing. These fine filters were intended to prevent the small sperm cells from leaving the filter device. A potential concern for this concept with the incorporation of an off-die drainage sink is the possibility of too much fluid being drawn from the sample and resulting in premature drying of the cells. Furthermore, through including an external drain at a lower elevation to the reservoir meant that the addition of oil to the device surface in order to prevent evaporation could provide a pressure differential across the device sufficient for oil to enter and contaminate the filter structures and filtrate.

94
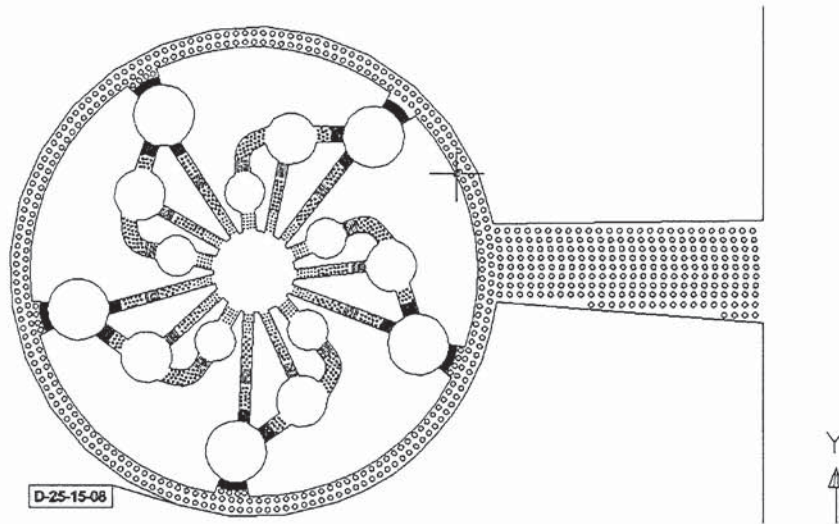
Figure 3.22: schematic diagram of filter type 'D' with drainage structures for the processing of larger fluid volumes.

3.7.8 Concept E

A reversal of the logic used in generating concept 'A' the capillaries increase in width as they approach the final spermatogenic cell stage (figure 3.23). This provides a greater volume at the end of the capillary so that more fluid can reach the final stage and help reduce the risk of the device becoming saturated before many of the cells can reach the last stage of filtration.
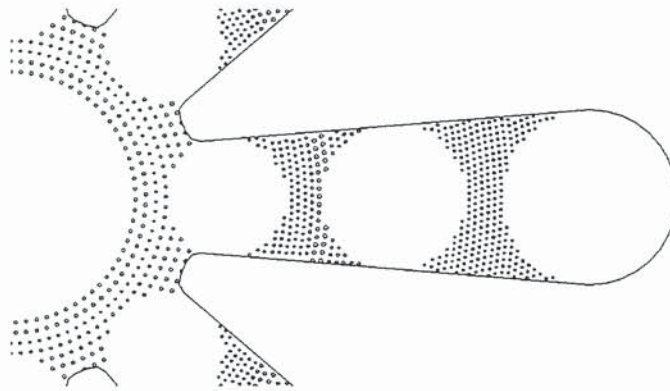
Figure 3.23: schematic diagram of filter type 'E'. Filtration channels taper outwards from the centre of the die peritting larger volumes of fluid to accumulate in the later stages of separation.

This configuration also permits easier access to the later access wells with micro - aspiration tools, but it is anticipated that a larger volume of flushing media will be required for the device to wet completely. In order to provide optimal etch loading the same layout of filter elements was adopted as in 'A2', and the filter stage format was the previously used standard of 25, 15, and 8 μm.

3.7.9 Concept H

A final deviation from the polar design of the other concepts this makes use of rectangular and square access ports and three apparently serpentine capillaries. However, there are actually six straight capillaries leading in pairs from the 3 common reservoirs. This was intended to offer a variety of filter element types on a single chip for direct fluid flow comparison. The upper-most channels are occupied by tapering wall structures that are designed to funnel fluid and trap particles of differing size at different points along the channel. The next capillary down uses ridged parallel walls to trap particles of irregular morphology. The third, fourth and fifth capillaries employ discrete square, elliptical and round pillars respectively. The sixth capillary is populated with parallel wall structures as used in 'C2'. This concept also provides capability for more precise cell selection, using sequential filter stages of 25, 15, 12, 8 and 3 μm pitch.
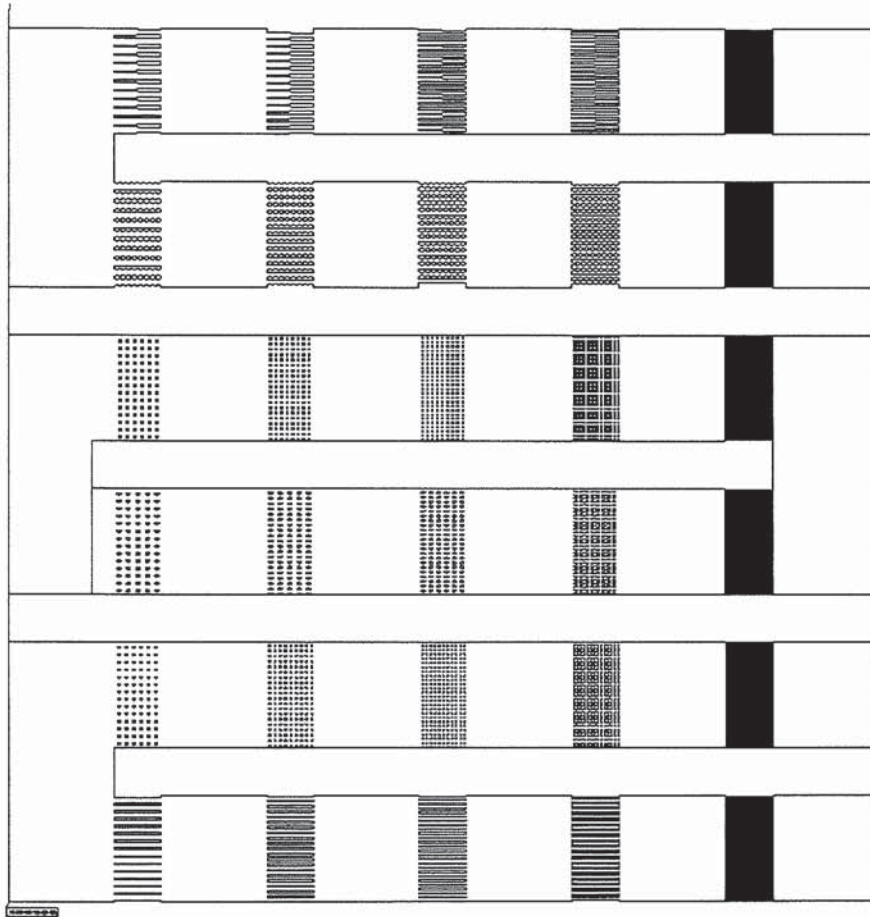
Figure 3.24: schematic diagram of filter type 'H'. A deviation from the polar arrangement of the previous concepts, this has six channels populated with 5 discrete filter stages leading from 3 common reservoirs.

98

3.7.10   Test Device

In order to create an analog of the concept device that can be tested and used to validate design and modelling assumptions, a number of test structures were drafted. The test device was intended to provide comparative data on wetting and particulate velocities within a simple linear microfabricated channel that could be used as a baseline for the overall device types, and as an indication of inter and intra-wafer variations in flow. The test device takes the form of a 5 mm long channel of rectangular section ($300 \times 60 \; \mu m$) connecting the base of two round reservoirs of common size (figure 3.25). Offset from the centre of the channel is a 500 μm region of linear channels with a pitch of 30 μm that simulates filtration elements. The round reservoirs are 2 mm in diameter, facilitating external connection to a continuous flow if required, and providing a stark contrast between surface tension in the channel and the reservoirs.

Test Channel

(i) Inlet   Direction of flow ⟶   (ii) Outlet
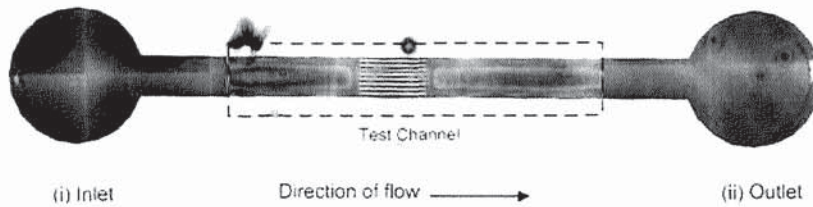
Figure 3.25: micrograph of the manufactured test device showing (i) inlet and (ii) outlet and the filter elements within the test region.

3.8 Manufacture

3.8.1 Introduction

The project saw the development and manufacture of 3 batches of wafers of varying yield, each as a consequence of experience and knowledge gained in the previous batch. With each batch there was a revision of the manufacture process in order to increase wafer yield and accomodate process limitations. This section details the manufacturing details and experiences from the final batch of wafers, with only reference made to previously encountered problems. The section begins with a process flow diagram with a subsection detailing each of the more important processing stages and the impact of device design.

The manufacture of the devices was coordinated across four sites. The microelectronics foundry in the Department of Mechanical and Manufacturing Engineering at the University of Birmingham provided their etching facilities for the first and second wafer batches and also provided anodic bonding of the silicon wafers to glass for these wafer batches. The Scottish Microelectronics Centre at the University of Edinburgh provided use of their foundry for the complete wafer processing of the final batch, and precision dicing machine manufacturers and contractors Loadpoint Ltd of Cricklade Swindon performed all wafer dicing. The final wafer batch was bonded by Applied Micromachining Ltd of Oxford. All testing and evaluation was conducted at Aston University using the microscopy and micromanipulation equipment available.

3.8.2   Wafer Layout

Having determined an approximate device morphology and size, an additional 100% border was created around each device to permit easier handling, resulting in the 5 *mm* devices enjoying 10 *mm* separation in all directions (figure 3.26). The overall wafer size being used for manufacture was some 100 *mm* in diameter, requiring a 125 *mm* square photomask. The photomask layout pattern was then constructed within AutoCAD, adhering to the ASM3500 GDSII drafting software requirements of the mask manufacturer [86]. The wafer and device size permitted the tiling of 96 devices onto the four inch (100 mm) wafer, permitting much flexibility in the number of design variants that could be incorporated into a single manufacturing batch.
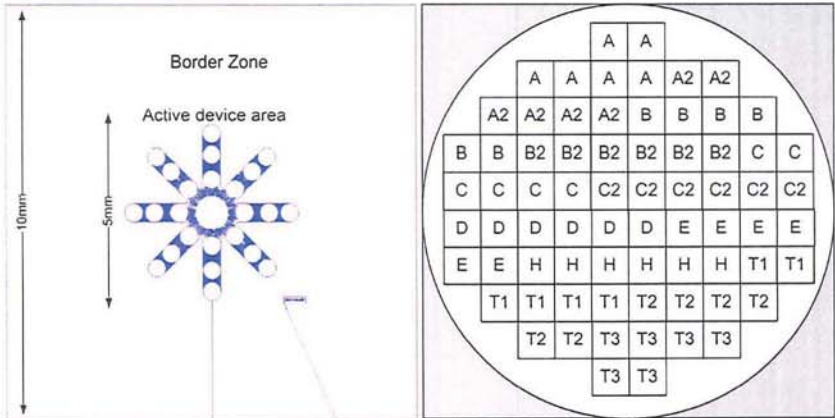
Figure 3.26:   mask layout demonstrating generous border around active device (left), tiling of the devices across the photomask, with indication of device types and locations (right)

3.8.3   Wafer Processing

Following the preparation and manufacture of the photomask, wafer processing can start, beginning with the transferral of the mask pattern. The silicon wafers are initially cleaned in alcohol, eliminating debris and oily residues that could adversely affect subsequent process steps. The transferral of the photomask pattern is achieved through what is termed 'direct-printing'. Through this method a photosensitive polymer is applied to the wafer, that is then exposed using a UV light source. The polymer is known as a 'resist' as once it has been exposed and developed through appropriate chemistry it is resistant to the action of etchants. The nature of the resist is specific to the application and can be either 'positive' or 'negative', being dissipated or cured, respectively, by exposure. The aspect ratio of the DRIE trenches are a function of the resist and its tolerance to the etching chemistry, as such, deeper structures require thicker coats of resist than more shallow features. The thickness of the resist can be controlled during its application to the wafer and is a function of the resist viscosity and angular velocity of the wafer during the 'spinning' process (figure 3.27). Through selecting more viscous resists and applying them to a wafer spinning at lower velocity can permit the application of conformal resist coatings with a thickness of several microns. Patterning and processing of the wafers was conducted via two methods, one method pioneered at Birmingham, the other at Edinburgh.

3.8.3.1   Manufacturing Method 1

Devised and conducted by Peter Docker and Peter Kinell the patterning method involved the sequential spinning of photoresist onto each sides of a double side polished (DSP) wafer and subsequent exposure and development of both faces at the same time. This involved a great degree of skill and careful handling in order to preserve the integrity of the initial photoresist layer during the second
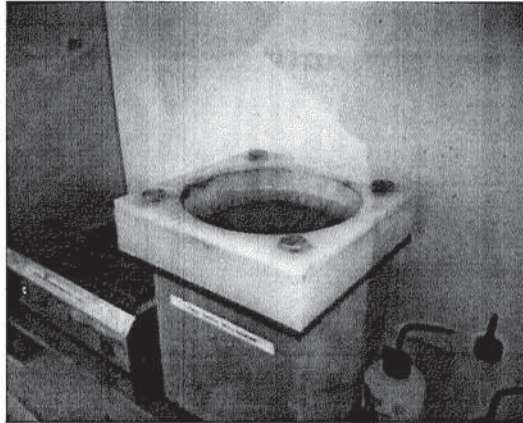
Figure 3.27: image of the resist spinner. Photoresist is applied to the wafer surface through application as a viscous liquid to the surface of the wafer as it spins.

resist spinning process, and also in optimising the development process in order that features on both sides of the wafer were correctly reproduced. The resist used was Microchemicals AZ5214, with several coats being applied to one face in order to facilitate the deeper etch.

The first etch was that of the fine feature side of the wafer, producing the filtration elements and die indentification marks to a depth of 60 μm. In order to complete the through holes, the etched face of the wafer was temporarily bonded to a 'handle' wafer using uncured photoresist that was subsequently baked to secure the bond. This permitted the wafer to be etched from the back without damaging the fine structures on the front. After the second etch was finished, and the through-holes were completed, the wafer was released from the handle wafer by immersion in nitric acid, and the resist was dry stripped and cleaned by oxygen plasma (a process known as *'ashing'*). Figure 3.28 provides a diagrammatic overview of the principal steps in device manufacture by this method.

	healthy fertile man	non-obstructive	obstructive
Total cell count	–	31×10^6	33.3×10^6
Primary Spermatocytes	40×10^6	0.7×10^6	0.8×10^6
Round Spermatids	76×10^6	0.65×10^6	0.76×10^6
Elongated Spermatids	–	0.35×10^6	0.65×10^6

Table 3.1: typical cell quantities, normalised per $1g$, as obtained through testis biopsy for healthy, obstructive and non-obstructive azoospermic males [7]

A number of studies on the morphology and scale of spermatogenic cells have been conducted with the intention of providing clear reference marks for the purposes of identification [81]. As such the approximate sizes of the cells may be summarised as in table 3.2.

structure	diameter (μm)	population %
seminiferous tubule	100-150	N/A
Primary Spermatocytes	16-18	6-9
Round Spermatids	6-8	18-20
Elongated Spermatids	4-6	10-12

Table 3.2: typical cell dimensions and their approximate population of total cells per $1g$ of testis biopsy tissue. [7] [8] [9]

3.8.3.2   Manufacturing Method 2

A more conventional approach was adopted by Tom Stevenson and Bill Parkes at the Scottish Microelectronics Centre, with the patterning of the feature side of the wafer and completing the first etch prior to resist application and pattern exposure of the other side. The front-side pattern was printed in about 1.5 microns of resist and then etched to a nominal 60 micron depth into the silicon, thus producing the fine feature filtration patterns. The resist used was Rohm & Haas (Shipley) SPR350-1.2, which was not stripped following the etch. The fine details of the features following the etch precluded the further application of resist to protect the features as the application would result in an uneven coating and probably damage the sensitive structures.

The back-side of the wafers was then coated with thicker resist (Rohm & Haas (Shipley) SPR220-7.0 - 8.5 μm) and gently soft baked, supported on 3 pins above a hot plate for 4 minutes followed by an oven bake in a cassette holder. This was done to avoid the resist on the front contacting the hotplate and damaging the structures. The back-side pattern was then aligned with a mask aligner based on the feature patterns and exposed resist. The wafers were developed by immersion using a cassette holder to avoid surface damage, then rinsed and dried in a Marangoni process to avoid violent spray washing and the risk of pillar removal. Figure 3.29 shows the process flow diagram of the manufacturing method.

3.8.4 Wafer Cleaning

The etching cycles incorporate the deposition of two forms of resist, a patterned resist for the formation of features, and a sidewall passivation resist applied in the form of a conformal plasma and selective removed through ion bombardment. The wafer was cleaned of these polymers via a selection of the following procedures:

1. Initially an acid strip of the bulk of the resist using fuming nitric acid. Followed by exposure for 60 minute to oxygen plasma, and an additional 65 minute ash.

2. The next trialled clean-up process involved a 60 minute ash, removal of heavier resist deposits with acetone, and a final 65 minute ash to clear.

3. Lastly, a 60 minute ash was conducted, followed by a high power ash at high temperature for an extended period in order to ablate any remaining resist.

Process 3 was found to be effective, but time consuming and inefficient as each wafer must be treated individually, and there is an elevated risk of fine structure damage as a result of the higher pressure of the plasma used. Of the tested procedures method 2 appeared to produce the best results, and for future trials the following modification is recommended:

1. initial edge bead removal - removal of the thicker resist deposits that accumulate at the edge during the spin coating process.

2. standard O_2 plasma ash for 60 minutes.

3. subsequent and final 65 minute O_2 ash to clear any remaining deposits.

Figure 3.29: a diagrammatic overview of the manufacturing process as employed at the Scottish Microelectronics Centre

3.8.5   Wafer Bonding

The etch process involves the deposition of a sidewall passivation polymer, C_4F_8 [79], that is largely removed during a final stage ashing cycle. The silicon wafer, of 350 μm nominal thickness, was wet-stripped of all resist with nitric acid and alcohol and rinsed thoroughly with distilled water before drying. The cleaned wafers were aligned with and bonded to 500 μm thick glass wafers through an anodic bonding process. Also known as fusion bonding, this is a process by which adjacent wafers of glass or silicon can be bonded through the artificial growth of silicon dioxide between them. Bonding involves heating the wafers in order to mobilise the ions within their amorphous structure and applying an electric field across them. In the case of bonding glass to silicon the wafers are heated to approximately 380°C, which permits the movement of Na+ ions and causes them to be attracted to the non-bond surface that is held at a potential of -800 V. The Na+ migration leaves a net concentration of -ve O_2 ions across the bond surface that reacts with the adjacent silicon wafer to form SiO_2 (silicon dioxide) which then fills the gaps between the wafers and creates a strong hermetic bond.

Wafers were bonded with the finely featured side down, closing the capillary structures with a glass lid. Great care was taken to ensure that all filter structures could bond to the glass as well as the adjacent silicon plains, but this could not be guaranteed due to the small size of the features. Bonding of the final batch was conducted by those skilled in the process at Applied Micromachining Ltd in their clean laboratories within the Rutherford Appleton Laboratories, Oxford.

Figure 3.30: Loadpoint MicroACE wafer dicing machine

3.8.6 Dicing

All dicing was contracted to dicing machine manufacturers Loadpoint ltd, of Cricklade, Swindon. The wafers were dissected by 18 equal cuts to produce 96 discrete dies through the use of a 100 μm resin blade on a Loadpoint MicroAce dicing machine (figure 3.30). Typically a metal blade would be used for the sectioning of silicon, however since glass requires a resin blade the glass bonds precluded this. As such the sectioning of the silicon with a non-metallic blade produced localised chipping along the section lines (figure 3.31). Prior to dicing the wafers were bonded to a self-adhesive polymer film, serving to seal the access wells from contamination during and after the dicing process, and transported and locked within a plastic frame (figure 3.32). The blade was calibrated to pass through the wafer and penetrate 100 μm into the film to ensure a clean and complete section. The adhesive on the film was UV sensitive, such that dies could be readily removed from the film frame through exposing the frame to UV radiation without leaving residues. The incomplete sectioning of the polymer film permitted easy transportation of the dies in their original location on the etched wafer.

(i) Silicon diced edge   (ii) Glass diced edge
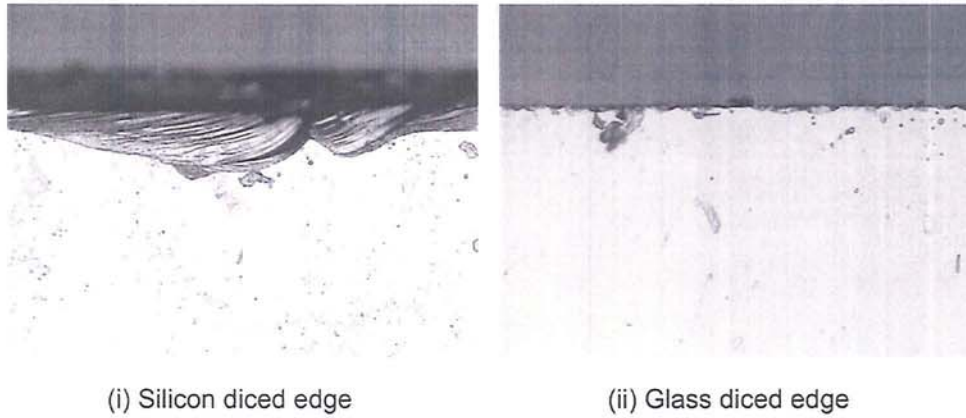
Figure 3.31: optical micrographs of the the diced edge quality of (i) Silicon, and
(ii) Glass, as a result of using the resin cutting blade to cut the composite material

(a) – The diced wafer supported on   (b) – close-up of the section line
the film frame
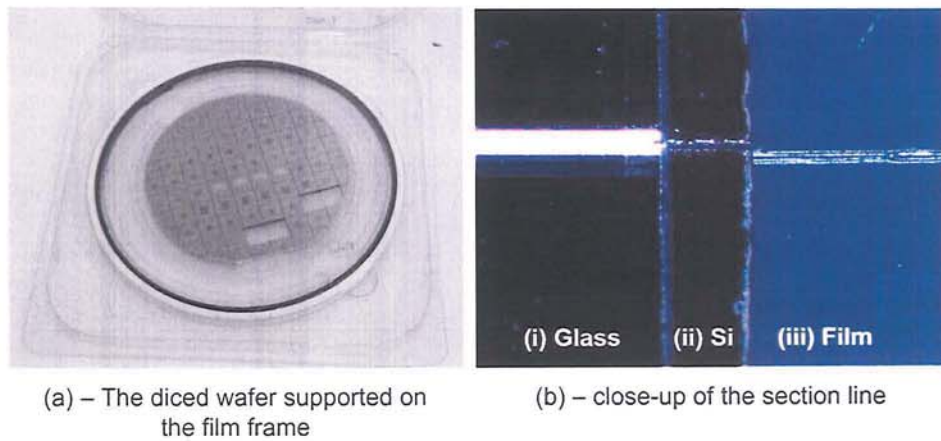
Figure 3.32: (a) the finished diced wafer supported on a polymer film. (b) an
optical micrograph of the cutting line as it sections (i) the glass, (ii) Silicon and
(iii) creates a partial cut in the polymer film layer.

3.9 Evaluations and Revisions

Manufacture was in three batches of five wafers, the results of each batch including the wafer and device yield, and notes on etch quality are discussed here. For reference, a summary of the concept designs and the manufacturing and fluid-flow considerations that they were intended to address can be located in Appendix A.

3.9.1 Batch 1

The manufacture of the devices in the initial batch was, in some cases as expected, fraught. The production run was the most prone to error as it was in this batch that the processing method was developed. The primary mode of failure was a consequence of the invalidity of certain processing assumptions.

Preliminary manufacturing concepts made use of a wafer that was to be subjected to two successive etch processes from one side only. The intended manufacturing concept involved a two photo-mask process whereby holes were to be etched through the silicon wafer by the DRIE process, and then a second etch creates the filter elements and capillaries. The etching sequence was to be conducted such that all etching processes could be performed from the same side of the wafer (figure 3.33). It was thought that this could significantly reduce the opportunities for alignment and handling errors, and a moderate wafer cost saving since only one face of the wafer would need to be highly polished. This process concept was flawed since it relied upon the assumption that a porous wafer could accept coatings of resist as readily as non-porous wafers. The effect of attempting to coat the porous wafer with resist generate pools and troughs of resist resulting in surface height fluctuations that exceeded the tolerance of the exposure process.

Photo resist is spun onto the wafer and exposed and developed. Dark regions indicate areas to be etched

DRIE process is used to etch through the wafer, creating reservoirs and collection chambers

Iinitial coat of photoresist is stripped and prepared for a second thinner coat of resist

Second coat is applied and exposed and developed with the device or feature mask, defining filter elements and flow channels

Second etch is conducted to a depth of 60 microns

Resist is stripped by ashing in oxygen plasma, creating a native silicon oxide on the etched surfaces

Wafer is selectively washed in dilute HCl, and cleaned in preparation for bonding

The wafer is inverted and anodically bonded to a glass wafer in order to seal the capillary trenches

NOT TO SCALE

Figure 3.33: the original concept for the manufacturing process was not possible since resist spun onto the porous silicon produced surface undulations in the second coating of resist

Consequently a dual-side alignment process whereby etching was sequentially undertaken from either side of the wafer was the only solution to manufacture. This revised process brought with it complications. Principally the optics of the dual side mask aligner required the mask for patterning the rear of the wafer to be reversed. Since this was not known at the time of mask drafting this was not the case and the transferred feature patterns were reversed. The subsequent process returned disappointing results.

A shortened production run of 3 wafers was conducted as a result of the mask reversal issue. Of those wafers only the devices that were laid out on the mask with reflectional symmetry were correctly machined. Schematics of the wafer masks are shown in figure 3.34 and the devices without symmetry are indicated. The result of this reversal without symmetry is illustrated in figure 3.35. As mentioned previously the initial batch was also designed to serve as a proof of the DRIE process; an investigation of feature size limits and distribution effects, and as an evaluation of the mask drafting process. Optical micrographs of representative devices were examined and compared with the mask proofs in order to identify any failure mechanisms. Due to the poor yield this was not possible with all device designs, however those that were produced could be used to identify possible problem areas in other concept designs.

3.9.2 Failure Modes and Revisions

In comparing the optical micrograph of device 'A' with the feature mask revealed a number of structures to be absent in the manufactured device, particularly in the vicinity of the central reservoir. The 4 μm pillars surrounding the central reservoir were too small to be constructed as free-standing structures when etched to a depth of 60 μm, possibly being on the limit of the maximum aspect ratio. The
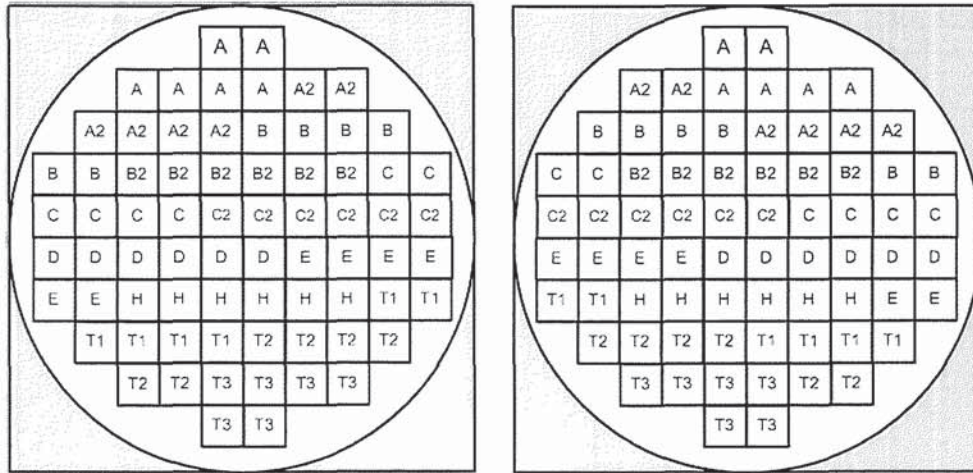
(i) Hole Mask Device Layout

(ii) Feature Mask (Reversed)
Device Layout
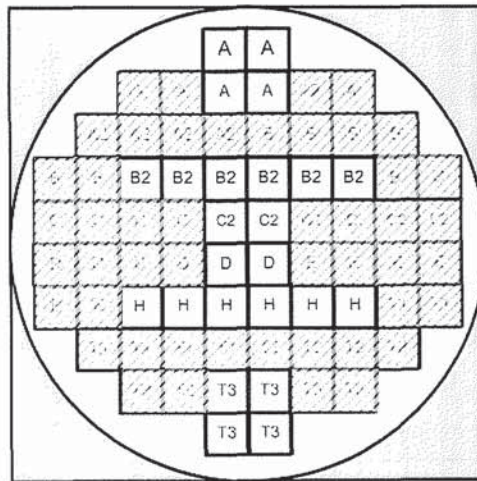
(iii) Composite – invalid devices
greyed out

Figure 3.34: the photomasks used in batch 1. When the feature mask (i) was reversed it only correlated with a small number of devices on the hole mask (ii). A small quantity of usable devices were yielded (iii).

115

(i) Concept B2 feature mask with type A   (ii) type H feature mask with reversed type
              hole mask   H hole mask
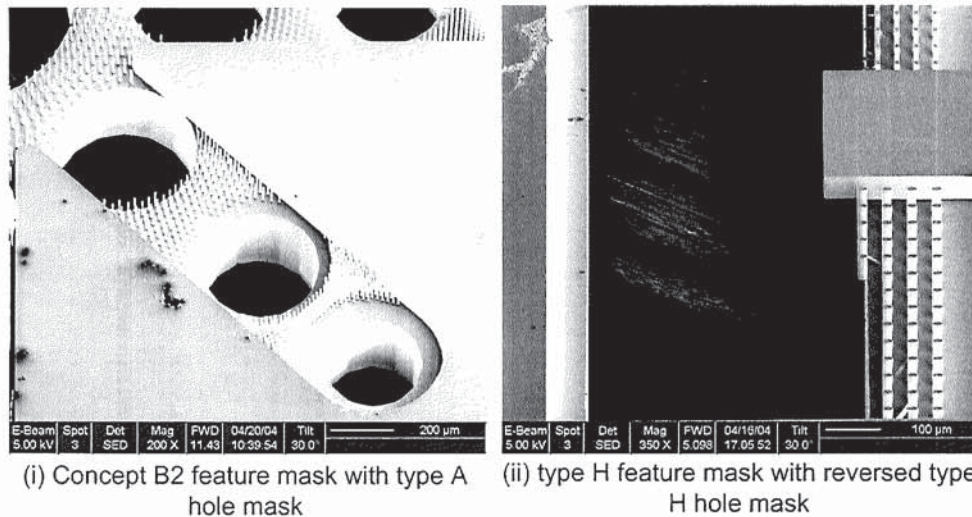
Figure 3.35: (i) voids around access wells as a result of hybridising 'A2' hole mask and 'B' feature mask. (ii) pillars teeter on the edge of a through hole as a result of misalignment.

fine 4 μm found to be missing from the 'A' devices were found to survive in 'B2', however in this instance they were not adjacent to larger structures and as such microloading was much more even. Nonetheless, SEM imaging of the structures identified the resultant structures as exhibiting very poor morphoplogy and prone to damage (figure 3.36). In light of this, concept 'B2' was dismissed and a new concept, 'B3' was introduced (figure 3.37). Concept 'B3' was a variation on 'C2' in that it used linear channels, however it employed the circular hole mask of 'B' and was designed with finer pitch filtration features than 'B2'. The channel filter element pitches adopted were a compromise between the fine 'B2' elements and the standard sizes, at 20, 10 and 5 μm.
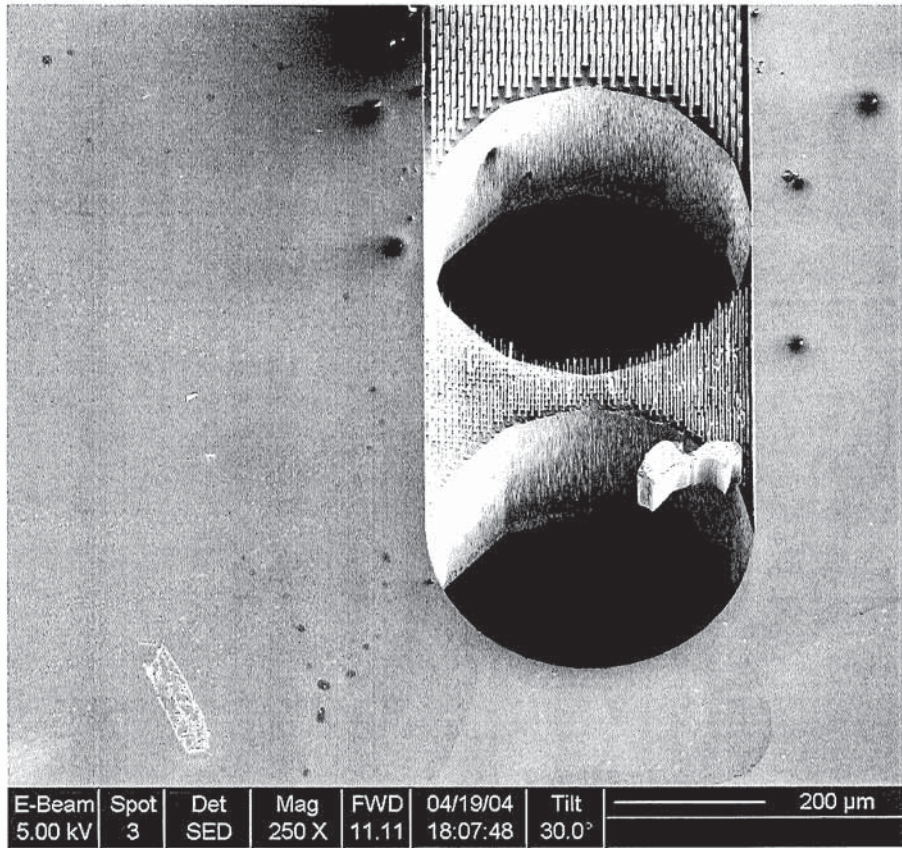
Figure 3.36: the small size of the features in the last filter stage of concept 'B2' returned very poor morphology, with many pillars being lost during the completion of the through-hole.
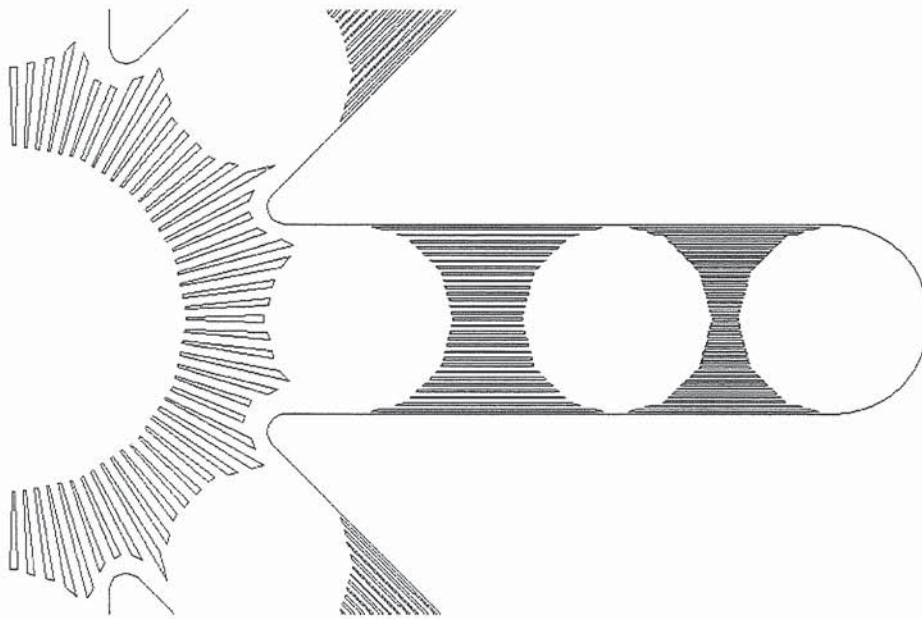
Figure 3.37: concept 'B2' was discontinued and replaced with a design using fine linear filtration channels at a slightly smaller pitch - this was called 'B3'. Care was taken to ensure filter elements extended to the rim of the access wells.

3.9.3 Batch 2

Batch 2 was conducted following the redraft of the hole and feature masks, and the reversal of the feature mask in order to avoid the poor yield of the previous batch. The yield from batch 2 was in fact poorer than that from the previous manufacturing run as a result of poor process control. A thermostat fault in the STS[1] multiplexing etcher at Birmingham University resulted in the wafers being overheated, damaging the integrity of the resist and introducing stresses into the wafer during the etch process. All devices were filled with sooty deposits and exhibited considerable attrition of the filter structures. Further to this, the elevated temperatures caused all wafers to partially bond to the platten within the etcher (figure 3.38) and subsequently fracture upon attempts to release them from the etcher/platten.

3.9.4 Batch 3

The most successful of the manufacturing processes employed the Stevenson-Parkes modified patterning and etching procedure and the revised masks of batch 2. No dies were lost during the etching, bonding, or dicing process and the etch quality of all five wafers was acceptable such that there were no apparent losses of filtration structures. Some variation was found between wafers, with the quality increasing as the process was refined with each iteration, but visual inspection indicated no areas of cause for significant concern.

3.10 Batch 3 - Wafer Etch Evaluation

One of the motivating factors behind the generation of multiple device types was that of evaluating the etch process, exploring the limitations of the manufactur-

---

[1]STS - Surface Technology Systems plc (Newport)
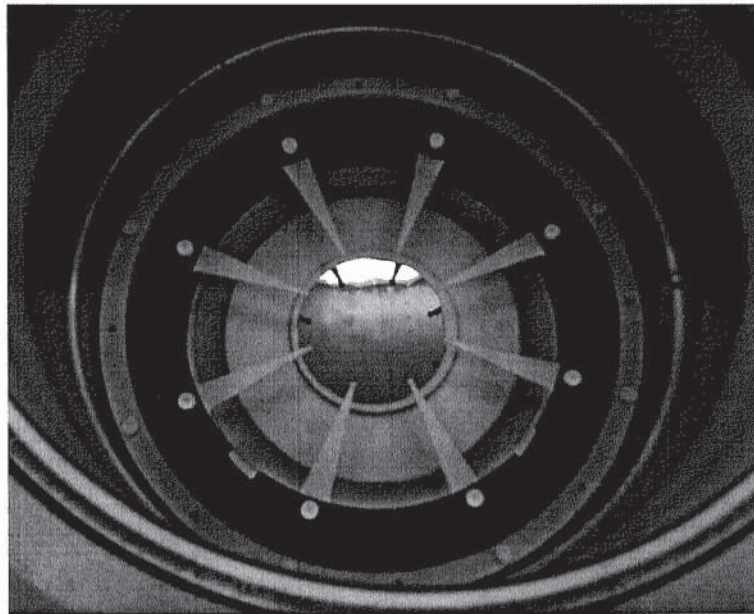
Figure 3.38: photo of the wafer within the etching chamber, taken with the chamber lid removed in order to extract the wafer that had become bonded to the platten

ing techniques applied and to generate an appreciation or understanding of the effects of patterned feature size and density on the final etch quality. To this end this section serves to provide a morphological evaluation of the various dies across the wafer batch and attempts to identify the source of poor manufacturing outcomes. In addition to reinforcing an understanding of the etch process this also serves as a means of identifying dies and wafers suitable for subsequent testing and evaluation.

The wafers are treated individually, referring to the inter and intra-wafer variations where appropriate, and evaluated on the etch morphology in comparison with the design. Sidewall qualities were not possible to image without die disassembly and study with an scanning electron microscope, a length that was not justified for the purposes of this study. Consequently, morphology was based primarily on feature preservation, hole completion, and dimensional accuracy of the etched features.

In addition to the study of individual device types the wafers were closely inspected in order to identify any potential areas for concern such as presence of sooty deposits, missing or damaged etched structures, unetched regions or plateaus, incomplete bonding, or internal debris.

3.10.1   Wafer 2006/1

Initial inspection revealed a small number of voids in the wafer bond, however no voids were found in immediate device regions, making the bond suitable for further processing. A thick beading was prominent around the edge of the wafer on the non-device side as a result of the thick photoresist employed, and although clear of the majority of devices it did cross a number of edge-ward dies.

Fine filter elements such as those featured in 'A' survived poorly, particularly around the central reservoir, an effect that was more prominant towards the edge of the wafer. Larger, more regular pillar structures, such as those featured in 'A2', survived much better. Also there were considerable levels of sooty deposits upon and within the channels of the majority of device types, again an effect that was worse at the wafer edges. The fine 3 μm final filter stage structures in 'H' were reproduced across the wafer with little apparent variation in quality. Some filter structures were damaged and broken as a consequence of some physical handling or washing process (figure 3.39), some were lost as a result of mask misalignment, and others through undercutting.
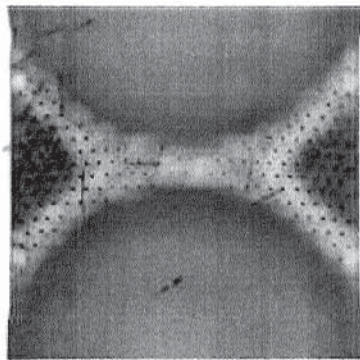
(i) undercutting of slender pillars
leaving needle shaped debris
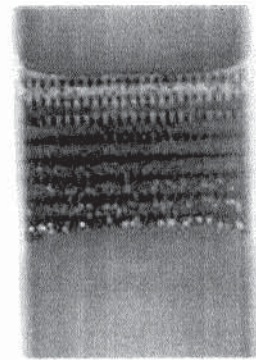
(ii) sooty deposits (black silicon)
discolour channels

Figure 3.39: poor etch morphologies in (i) undercutting of pillars, and (ii) internal deposits

The most noticeable effect, apparent on the 'C' variants, was the incomplete etch-ing of the access wells, retaining plateaus of silicon extending across the through-holes that partially occluded them. This was exaggerated across the wafer with the dies occupying the centre being less thoroughly etched than those at the wafer edges. The 'C2' devices being centrally located on the wafer were subsequently the most affected. The more edge-wards 'C3' with their hole spanning spars were well presented with the spars intact and uniform, but their proximity to the edge makes them subject to contamination with sooty deposits, possibly 'black grass', as a consequence of improper etch control.

In summary, the majority of the edge devices are unsuitable for further testing, and with the 'A' devices suffering from central filter region losses and damage these die types cannot be used. The incomplete etching of the central 'C' and 'C2' devices yield a cause for concern for the wetting phase of the fluid flow and are also unsuitable for testing.

(i) incomplete etching leaves thin
membranes occluding access holes

(ii) hole spanning spars left in-tact
with good morphology
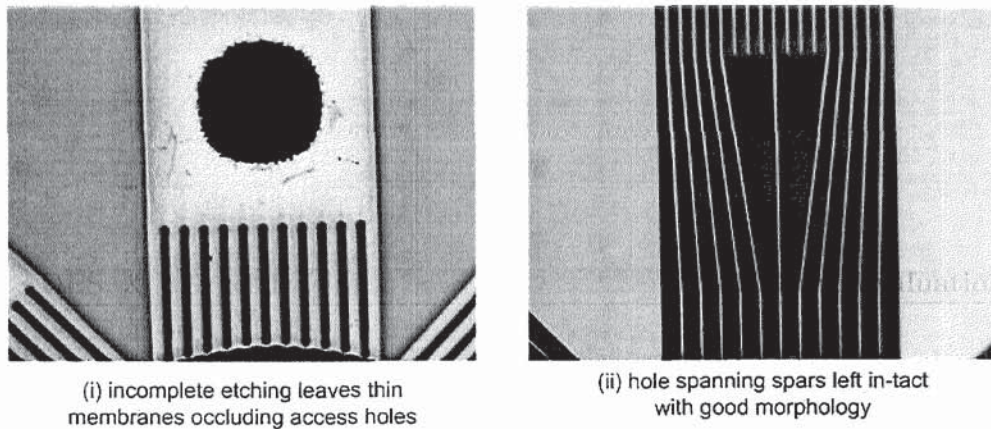
Figure 3.40: (i) device type 'C' exhibited underetching of through-holes. (ii) 'C3' showed good presentation of the delicate, hole spanning spars

3.10.2   Wafer 2006/2

Feature reproduction for the 'A' series of dies was much improved with no dies, even those nearest the edge, exhibiting lost pillars through undercutting or overetching. The through-holes did appear to have over-etched slightly with discoloration of the pillars immediately surrounding them, but this was most prominent around the edge of the wafer. All devices appeared to have successful hole completion, with good preservation of the majority of filter structures. Although some sooty deposit is visible within devices towards the edges of the wafer, this is localised towards the regions immediately surrounding the access wells (figure 3.41).
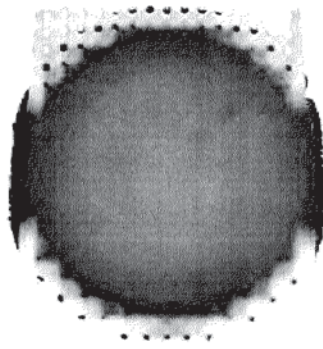
(i) over-etching is evident around through-holes as local discolouration
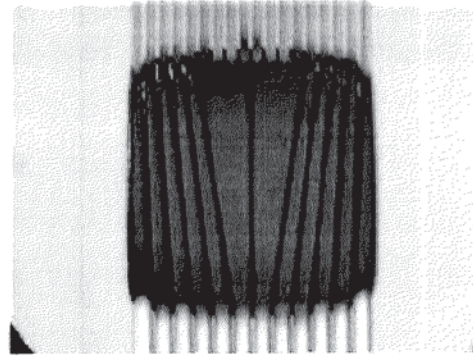
(ii) although spars are intact they are heavily eroded

Figure 3.41: (i) slender pillars are reproduced well, but there is evidence of over-etching of the through-holes, (ii) and heavy erosion of the 'C3' spars.

3.10.3   Wafer 2006/3

In the 'A' and 'B' concepts the majority of filter features are missing or incomplete as a result of excessive etching. No damaged filter elements are visible implying that the filter structures themselves have been etched away. A few remain in the vicinity of the walls, suggesting that they have benefitted from a reduced plasma

access to these regions (figure 3.42(i)). Dies A2-3-6 and A2-3-5 demonstrate good morphology with minimal feature loss, whilst the devices immediately adjacent to them suffer from a considerable degree of feature loss, indicating that dies directly benefit from a more central wafer location even across distances as small 5 - 10 mm.

(i) Pillars protected by the channel walls are preserved

(ii) vertically orientated channels

(iii) angled channels
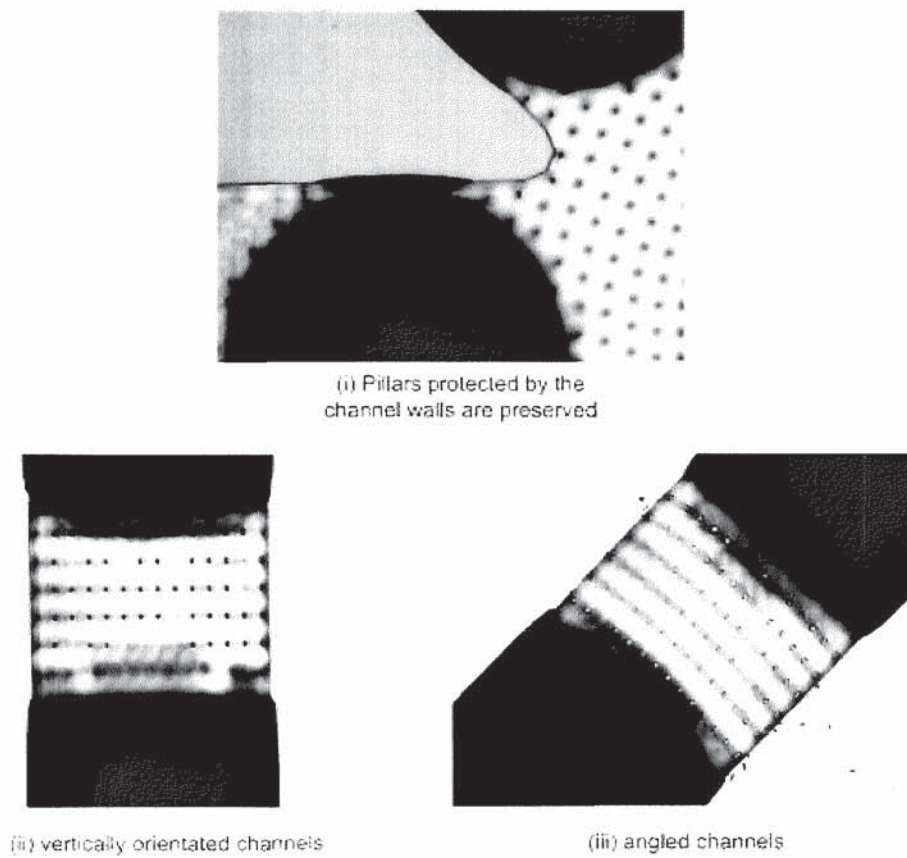
Figure 3.42: (i) only pillars close to wall structures are preserved. (ii) and (iii) pillars in 'C' devices are preferentially preserved depending upon the angle of the channel

'C2' dies with their thick filter structures and prominent wall features survived well, but their precursor 'C' exhibits considerable filter element loss. A degree of directionality in the etch is apparent, with pillars occupying the 0-180° axis of the wafer being considerable more depleted than those at 45° (figure 3.42(ii) and (iii)). This was more apparent nearer the wafer edge. The extravagant 'D' concept pattern of interconnected channels was subject to heavy pillar erosion with only the most densely populated fine structures, and the largest pillars remaining. This was true of all dies of this type.

'H' was extremely well preserved, with some minor damage to the finer filter structures but otherwise appearing robust and intact. This could be said of all filter types explored within the linear devices, including the fine pillars, of which a number were lost, possibly as a result of overetching the through-holes.

The 'C3' device with its hole-spanning spars exhibited good structural morphology within the filter regions but of the spars themselves only a few were intact, and all were subject to partial erosion. This erosion effect appeared to act from the glass surface, implying that the spars were overetched during the initial feature etch as opposed to the through-wafer etch, which without protection from photoresist would cause the spars to etch through from the non-device side.

3.10.4   Wafer 2006/4

As has come to be expected there was no yield of successful 'A' and 'B' devices on this wafer, with the vast majority of dies missing most of their fine filter elements. Some isolated regions of the device were subject to pollution and damage, it is not possible to determine when this occurred but it is perhaps a symptom of incomplete bonding (figure 3.44).

(i) horizontal spars heavily
eroded

(ii) angled spars eroded to a
lesser degree
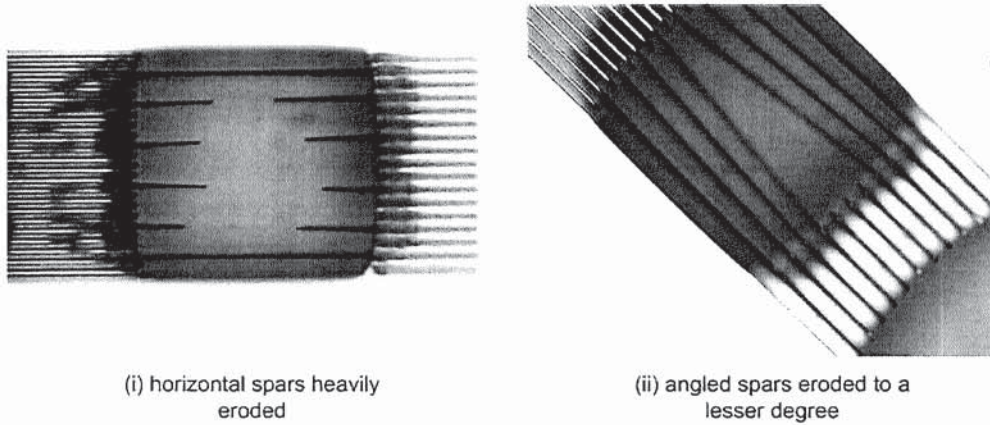
Figure 3.43: (i) spars spanning the holes in 'C3' devices are heavily eroded, again to a degree that is (ii) dependent upon channel angle.

(i) surface imperfections

(ii) first stage pillar loss and void in bond
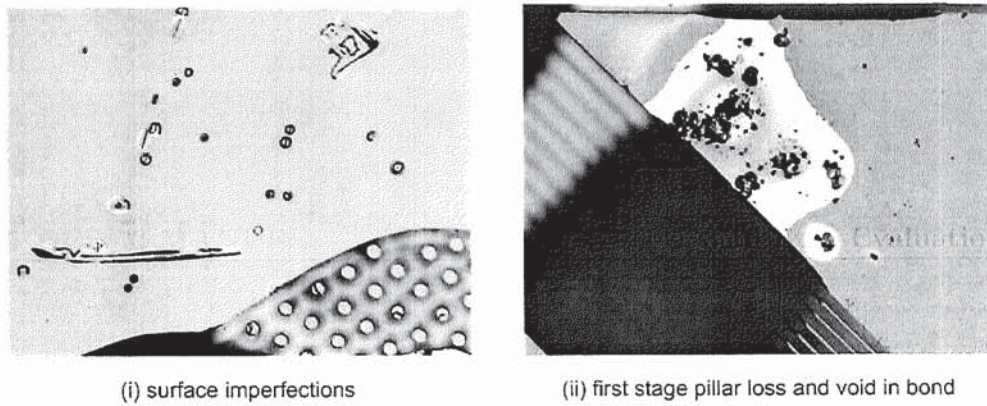
Figure 3.44: (i) surface damage around devices in some regions lead to (ii) voids in the anodic bond.

Of particular note is some of the damage inflicted on the 'H' dies, whereby localised regions of pillars are missing, and there are other regions of severe damage to the linear fine filter sections. In one region it is possible to see how a piece of silicon debris has forced apart some of the silicon channels, most likely during the cleaning process. Die C2-3-9 exhibits a region of channel that is devoid of filter walls, suggesting that there were no filter patterns in the photomask (figure 3.45).

(i) mechanical damage   (ii) mask error
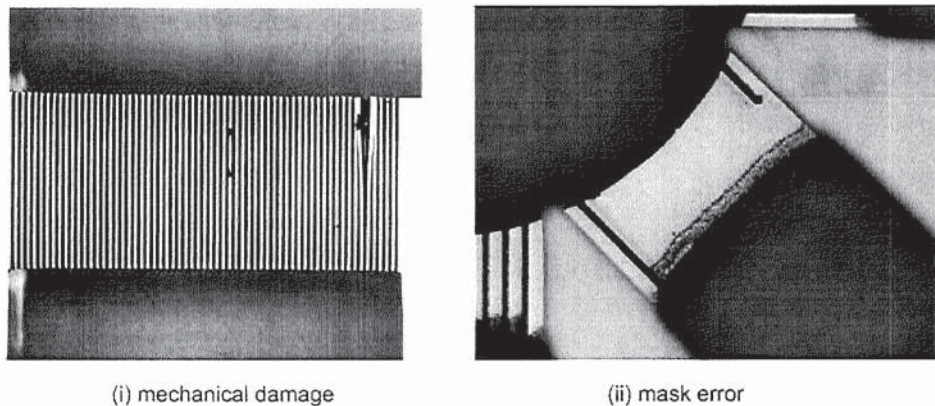
Figure 3.45: micrographs of fine filter stage of 'H' dies showing (i) structural damage due to debris and (ii) missing features caused by errors in the photomask

3.10.5 Wafer 2006/5

This was perhaps the poorest of the wafers, possibly as a result of it being the first of the batch to be etched and the one upon which the majority of processing mistakes were made. The etched channels were subject to thick blackened deposits throughout, and all of the devices of type 'A', 'B' were devoid of any filtration elements. Filters 'C2' and 'C3' were subject to sporadic loss of filter walls, and all devices of type 'E' had no filter elements and all spar structures in 'C3' were lost. The fine structures in 'H' were subject to considerable dam-

age, similar to that observed on wafer 2006/4. A small number of devices may be available for use, depending upon the importance of the primary filter stage, although the wetting properties in light of the polluting residues may render all devices unusable for all but the most basic tests (figure 3.46).

(i) first stage elements largely missing   (ii) sporadic filter element loss and localised pollution
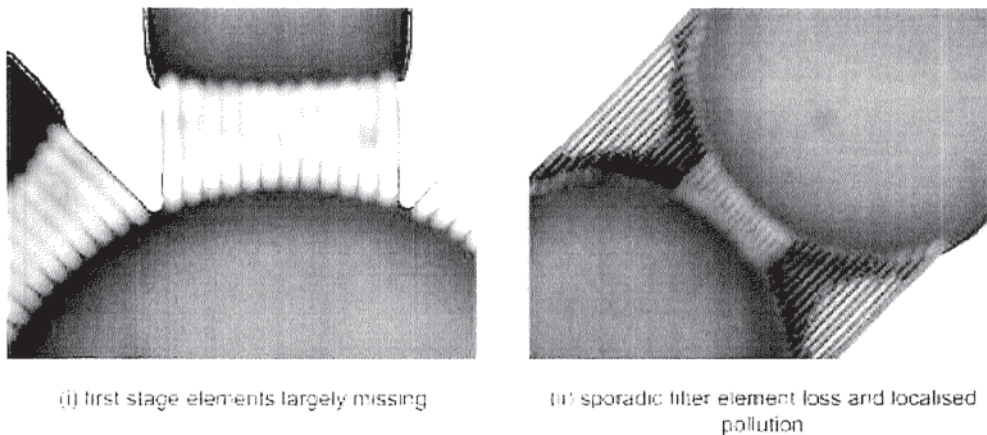
Figure 3.46: (i) early filter stages exhibited sporadic feature loss across the wafer, and (ii) regions of silicon grass pollution were widely observed

3.10.6 Summary

As anticipated, due to the etch loading effects in the dry etching process, the features of the dies nearer to the edge of the wafer etched more quickly than those towards the centre of the wafer. As a result the dies nearer to the edge were more subject to overetching and undercutting than the more central dies. Generally speaking across the entire batch this held true, although the degree that the edge-ward dies were affected did vary as a result of location and pattern.

The majority of the dies of 'A' suffered greatly from etch micro-loading imbalance. Die 'A' also suffered from unfortunate location in that being the first

concept it was placed at the top of the wafer, forming the first 2 rows of device designs nearest the wafer edge (figure 3.47). Suffering heavily from imbalanced etch microloading it is possible to see how the larger pillar filter structures have survived at the expense of the finer features. The smaller filter elements, those comprising the filter stages as opposed to those incorporated for etch-balancing, were subject to heavy attrition. In the latter filter stages it can be seen how some filter structures were sheltered by the edge of the channel.

The features of the 'A2' dies were largely preserved, the consistent pillar size and dense packing across the feature plane served well to balance the etch. In some instances the features in the first filter stage were lost whilst those immediately surrounding the central reservoir were partially formed (extending only 25 μm from the substrate).

The 'C' based dies, and 'H' linear devices appear to have survived the best, with their hardier and more robust designs proving less vulnerable to fluctuations in the control of the process, and of course benefitting as they did from their more central location on the wafer. The majority of edge-based devices are unusable, with the exception of those in 2006/2 whereby a compromise was met with features being underetched and the through holes overetched in order to provide the largest number of viable devices. Future designs should either avoid having etched features towards the edge of the wafer, with thicker more robust structures, or the dies placed around the edge of the wafer should have a uniformly higher etch-load than those nearer the centre that etch more slowly.
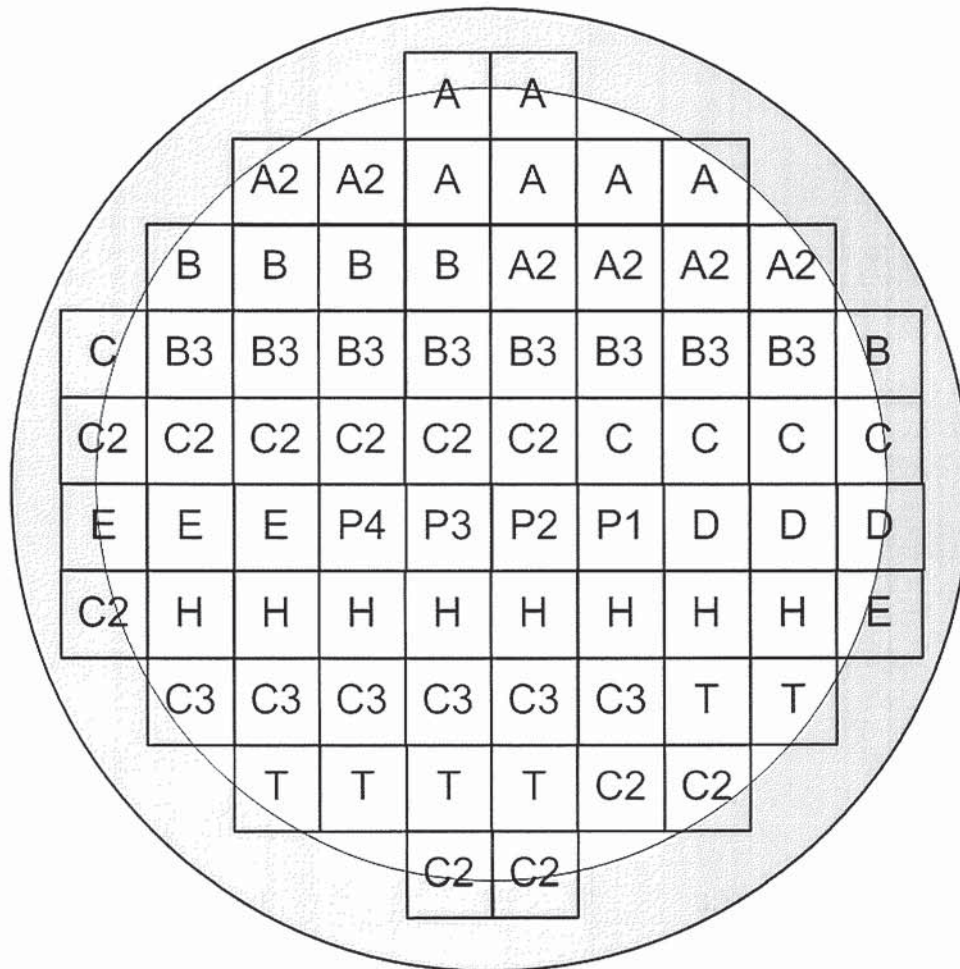
Figure 3.47: edge-ward devices, indicated by the grey ring, were subject to poor morphology, affecting a number of 'A' devices

Chapter 4

Microfluidic Modelling

4.1 Microfluidic Modelling Assumptions

This chapter explores in greater depth the principles involved in the modelling of microfluidic systems and networks, with particular attention paid to the similarities and differences between micro and macro-scale fluid mechanics. Conventional modelling of fluid systems dictate the behaviour of the fluid as being dependent on bulk fluid properties. As fluidic systems are scaled down the effects of molecular forces become more dominant. Through reducing the size of the systems further a point is reached where the effect of inter-molecular forces become stronger than the bulk fluid effects prevalent in macro-systems. This chapter explores this transition point and uses it to debate the validity of a number of classical fluid mechanics assumptions as they apply to MEMS fluidic systems. There is also a qualitative treatment of the sources and mechanisms of micro-scale forces and effects.

132

4.1.1   Fluid Gas Continuum

Fluid mechanics for application to macro-scale problems often work from the assumption that the fluid may be treated as a continuum [6] and as such requires that all of the quantities under investigation, such as density, pressure and velocity are continuous. This is to say that they impinge on neighbouring regions within the fluid causing the properties of interest to vary continuously between infinitely divisible points within the flow [87]. Considering density, for macro-systems this is a reasonable assumption as the fluid volumes are large in comparison with the spacing of the fluid molecules. However, when the characteristic dimension of the flow is reduced, the difference between intermolecular spacing and sample volume is much smaller (figure 4.1).

Gas flow in a micro-channel:
Sample volume of dimension L

L
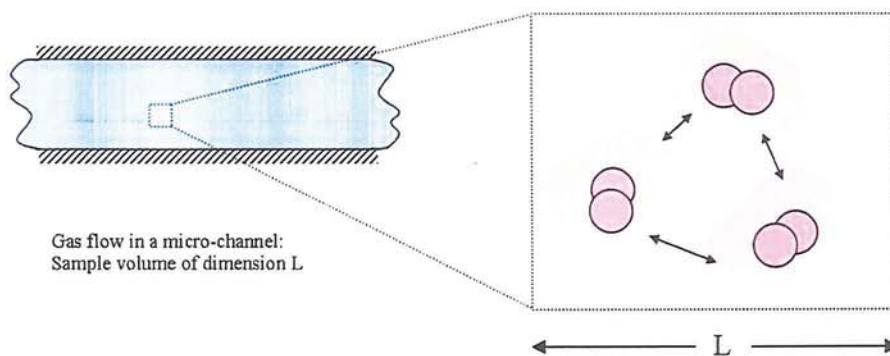
Figure 4.1: reducing the sample dimension L to approach the inter-molecular spacing

Consider a gaseous fluid flow, that is frozen in time and divided into discrete sample volumes. Initially, if the sample volume is comparable to the volume of a single molecule, the density of the sampled volume (ρ) can be considered

constant, and can be found by

$$\rho = \frac{m_o}{L^3} \qquad (4.1)$$

where m_o is the molecular mass, and L the dimension of the sample. Gradually increasing L will occasionally introduce additional molecules into the sample volume and the intermolecular separation becomes prominent. This separation will bring about localised differences in density within the sample volume, and the relationship between ρ and L will vary. As the volume is further increased the molecular population with respect to the dimension L will increase and ρ will become less sensitive to fluctuations in the molecule number (figure 4.2). The characteristic dimension at which this occurs is known as the *point value* [6] and is by definition the point beyond which the density of the fluid can be considered as continuous. If, however, the sample volume is increased too much, regional variations as a result of physical behaviour can be averaged out: for example acoustic shock waves or thermal effects.

In order for continuum conditions to be attained then all kinematic, thermody-
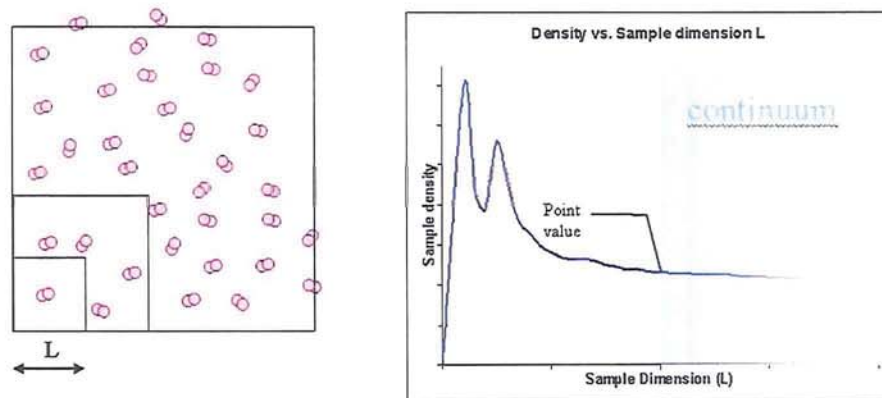
Figure 4.2: (left) increasing sample dimension changes density, (right) till point value is reached [6]

namic and transport properties must be continuous [88]: the validity of the point value for density alone may not be representative of the other fluid properties. In gases the variable of largest scale and fluctuation is the transport property, characterised by the distance a molecule of the gas will travel before it interacts with another, or the *'mean free path'*. The continuum assumption fails whenever the mean free path of the molecules becomes the same order of magnitude as the smallest significant dimension of the system [87]. The ratio of the mean free path of a gas (λ) over the characteristic dimension (L) is often used to determine whether the fluid will behave as a continuum, a continuum with wall slip effects, or as a free molecular flow. This ratio λ/L is called the Knudsen number (K_n). In cases where $Kn > 10^3$ non-equilibrium effects start to occur as different physical phenomena such as wall slip become more prevalent [28]. In such cases it may be said that the fluid ceases to follow continuum models.

4.1.2   Liquid fluid continuum

The intermolecular spacing of a liquid is typically 10% that of a gas, a value that is approximately the same as the molecular diameter (table 4.1). As such, the point at which density becomes continuous within a sample volume will occur at a smaller characteristic length (L) and so the point value of density for liquid flows will be considerably less than that of gaseous flows. Since there is effectively no mean free path for molecules within a liquid phase, the Knudsen definition for non-continuous flow cannot be used. However, as illustrated in table 4.1 the molecular diameter and intermolecular spacing of liquid flows are approximately equal, supplying a parallel to Knudsen number, the molecular *'lattice spacing'* (δ) [28].

Table 4.1: comparison between the properties of a gas and a liquid [6]
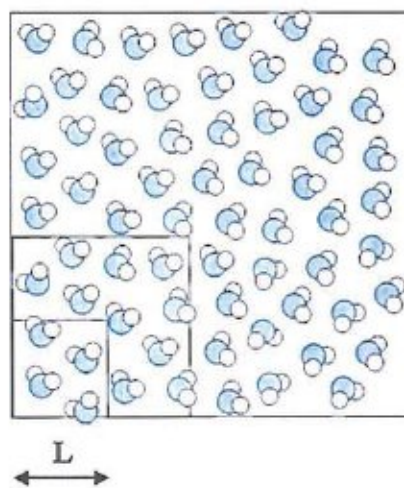
Figure 4.3: increasing sample dimension (L) for a liquid

Effects such as wall slip occur in gases when the mean free path of the molecules is approximately a tenth of the flow dimension - which in the case of air approximates to 650 nm. Since liquids have no mean free path, and the molecules can be considered to be in constant collision (figure 4.3) then these conditions do not arise until much smaller flow dimensions are considered: approx 3 nm. Following this reasoning, liquid flows in microdevices should be described adequately using bulk properties in continuum hydrodynamics with flow dimensions of below 1 μm [89].

4.1.3 Small Fluctuations

This argument is somewhat flawed. From figure 4.3 it can be seen that if the sample volume of gas is studied is too small, and too small a population of molecules is considered then local fluctuations in density and other local properties may be expected. The same can occur within liquids, however to a lesser degree, as a result of geometric voids and packing density limitations brought about as a result of the shape of the component molecules. Furthermore, when the energies and the randomised motions of the molecules are considered then the possibility of continuous conditions occurring at the scale suggested by molecule separation appears unrealistic.

If the fluid is considered as being described within an impermeable boundary of dimension L, and volume V and a fixed temperature T, then variables L, V and T will all remain constant and the probability distribution of energies may be considered Gaussian, with a standard deviation of the order of $N^{-1/2}$ [88]. If the boundary is then made to be permeable the energies will translate to fluctuations in position. The number of molecules within the system, and the local pressure, will then be subject to fluctuations of magnitude $N^{-1/2}$. In samples of small

population these fluctuations could be sufficiently large to negate the continuum assumption. By this reckoning Deen [88] suggests a lower limit for molecular population of 10^4 as a sufficient size to make fluctuations in state quantities acceptably small and explains that from this assumption that minimum sample dimension can be calculated as:

$$\delta L = \left(\frac{N_{min}}{n} \right)^{\frac{1}{3}}$$

where N_{min} is the minimum population, and n is the average number density of molecules. Substituting values of n for N_2 and H_2O:

$$\delta L_{nitrogen} > (\frac{10^4}{3 \times 10^{25}}) \to \delta L_{nitrogen} > 7 \times 10^{-7} m$$
$$\delta L_{water} > (\frac{10^4}{2 \times 10^{28}}) \to \delta L_{water} > 8 \times 10^{-8} m$$

Since N_{min} was arbitrarily assigned, and n is an average value there can be little confidence in the numerical quality of the estimate. The orders of magnitude of the estimates, however, provide a reasonable approximation for minimum sample dimension accommodating small local fluctuations: approximately 1 μm for diatomic nitrogen, and 0.1 μm for water.

4.2 Flow Mechanisms

Having established the viability of classical continuum fluid mechanics as it applies to fluid systems on a MEMS scale it now remains to establish the nature of mechanisms prevalent in microfluidic systems, how they may differ from those on a macro-scale, and the identification of any potential obstacles to the implementation of a microfabricated device that exploits microfluidic principles.

4.2.1 Scaling Laws

Reducing the characteristic length and scale of fluidic systems from conventional macro-scale hydraulic circuits where mass and inertial factors predominate results in the transition to a flow regime where viscous forces and surface effects are dominant - effects such as friction factor, surface roughness, surfaces energies and viscous dissipation.

On a macroscale fluid power losses as a result of viscosity and surface tension can be considered negligible in comparison with pressure heads and turbulent effects. On a microscale the mass of the fluid, and subsequently the pressure head caused by the mass of fluid is insignificantly small when compared with the over-pressure produced by the surface tension of the fluid. This effect comes about as a result of the dimensionality of the quantities involve. Mass is a function of material density and volume, which are the product of the three length components (L^3). Surface Tension is also a function of length, but since it is a *line force* that acts only around the wetted perimeter of a channel it is a function of L^1.

When the scale of a system is reduced, say halved, the volume is reduced by $(1/2)^3$ or $1/8$ whilst the surface tension force is only reduced to $(1/2)^1$ or $1/2$ (figure 4.4). Consequently, when a device is reduced 1000 fold, as is the case in

MEMS-scale structures, the volume, and mass, of a body reduce by a factor of $1/10^9$. So it may be said that the volume and mass of a body reduces with scale more rapidly than perimeter, and surface tension.
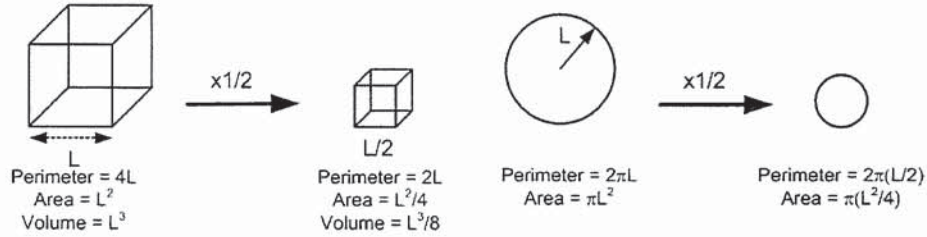
Figure 4.4: geometrical properties of perimeter (L^1) and area (L^2) reduce more slowly with scale than volume (L^3)

4.2.2 Surface Tension

At the liquid-vapour boundary of a fluid surface a tension force is exhibited inducing a pressure across the interface. This phenomenon is a result of a lower or higher molecular density in the interfacial liquid layer than in the bulk liquid. The inter-molecular spacings at the interfacial layer are different to those in the bulk fluid by virtue of an imbalance in the inter-molecular van der waals bonds. Molecules within a bulk liquid, that do not occupy a liquid-liquid, liquid-solid, or liquid-gas interface, exhibit forces of attraction that are equal in all directions (figure 4.5 (left)). These bonds keep the fluid molecules in a coherent mass until enough energy is supplied to overcome the attractive forces and the liquid changes phase to a gas. Interfacial molecules, that is, ones that form the separation between dissimilar phases, are not completely surrounded by adjacent molecules and as such are subject to a net attractive force acting towards the bulk of the liquid (figure 4.5 (right)).
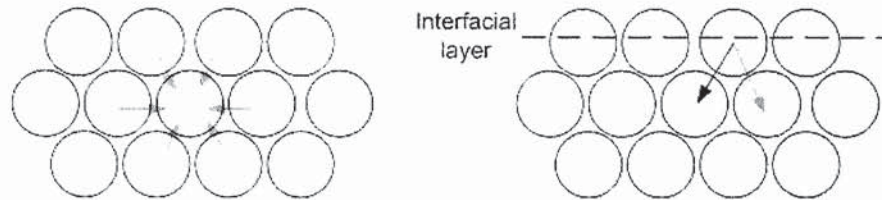
Figure 4.5: molecules in bulk fluid are subject to forces in all directions (left), whereas those occupying interfacial layers have a net force acting towards the bulk fluid (right).

Eyring's significant structures theory puts forward a molecular model for solids and fluids based on lattices with holes and vacancies that can be used to explain the behaviour of solid-liquid boundary interactions [90]. A substance has the least free-energy in its solid state, when the molecules that comprise it occupy an equilibrium state. In an ideal solid the molecules are closely packed without voids or vacancies in the crystalline lattice. When the material is heated and melts, energy is supplied to the molecules providing some with sufficient energy to overcome their inter-molecular bonds and move within the lattice - the bulk material expansion as it melts is testament to this and is a result of molecules displacing and leaving 'holes' or vacancies. The effective flow of the liquid occurs through molecules moving to fill these holes, and subsequently leaving holes from their origin (figure 4.6).

The asymmetry of the molecular force field at the interface and the resultant net force acting towards the liquid interior further reduces the possible molecular movements to fill the hole since it would require more energy for a molecule to work against the opposing force and move from the interior to the phase boundary. As such only sideways movements in the interfacial layer of the lattice are possible (figure 4.7 (i)). The result of these directional limitations mean that the time-
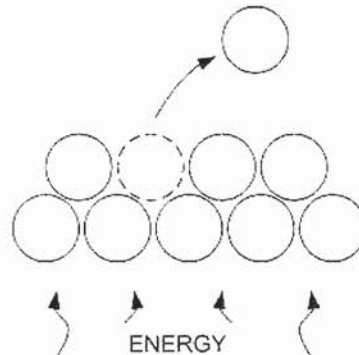
Figure 4.6: supplying energy to the crystalline lattice displaces molecules from the bulk leaving leaving 'holes' in the interfacial layer

averaged concentration of holes in the interfacial layers is greater then the interior layers: the surface layers are of a lower density than the bulk liquid and thus have a tendency to contract (figure 4.7 (ii)).
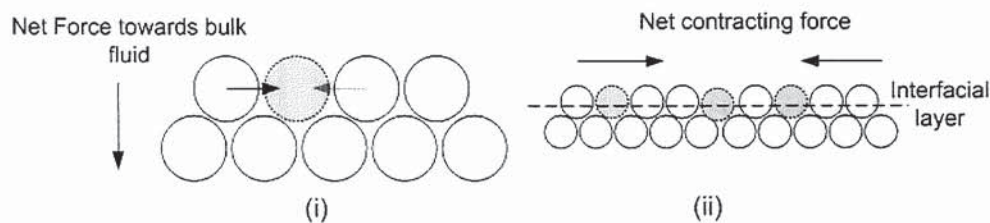
Figure 4.7: (i) a net force acts towards bulk fluid, so molecules can only migrate sideways in the interfacial layer leaving fewer molecules at the liquid-vapour interface (ii)

Now introducing a liquid-solid interface that is hydrophilic, the molecules in the liquid at the boundary behave differently to internal molecules. Holes that occur in the liquid-solid interfacial layer are more easily filled by molecules from the top, since sideways motion of the molecules is restricted by the stronger solid-liquid (adhesive) intermolecular forces. Once in contact with the solid the liquid

molecules require energy to escape and so the number of holes in the interfacial layer is much lower than that of the bulk liquid - giving the interfacial layer a tendency to expand, and the liquid droplet exhibits 'spreading' conforming to the geometry of the solid.
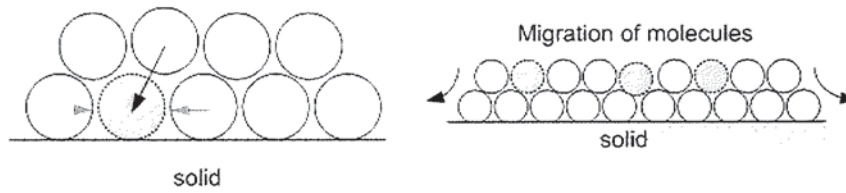
Figure 4.8: strong adhesive bonds between liquid and solid molecules increase layer density at the interface causing *'spreading'*

Conversely, in cases where the solid surface is hydrophobic, the liquid-liquid bonds are greater than the solid-liquid attractive forces and so an interfacial hole is more readily filled from the side than the top. As such the concentration of holes in the interfacial layer is higher than in the bulk, causing the layer to contract, and the liquid to adopts a more spherical form.

4.2.3   Surface Energy and Contact Angle

Considering the free surface energies of a system comprising the interface between a liquid droplet at rest on a non-porous solid phase material (figure 4.9), the total energy may be expressed as

$$U_T = A_{sl}\gamma_{sl} + A_{sv}\gamma_{sv} + A_{lv}\gamma_{lv} \tag{4.2}$$

where γ_{sl}, γ_{sv} and γ_{lv} are the free surface energies of the solid-liquid, solid-vapour and liquid-vapour interfaces, and A_{sl}, A_{sv} and A_{lv} are the respective surface areas.
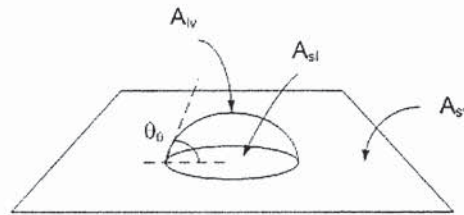
Figure 4.9: A liquid droplet on a solid surface and its interfacial areas

These energies may be visualised through the static contact angle (θ_c): the angle the edges of the liquid droplet make with the solid surface when viewed along the plane of the solid (figure 4.9). The surface energies are related to θ_c by Young's Law (equation 4.3).

$$\gamma_{sv} = \gamma_{sl} + \cos\theta_c \tag{4.3}$$

4.2.4 Capillarity or Capillary Effect

The concept of the fluid droplet on a surface can be extended to a fluid plug within a partially filled capillary. Figure 4.10 illustrates the interfacial surface energies and fluid contact angle. Liquid penetrates into narrow tubes, fine pores, cracks or channels due to an energy gain obtained by extending the solid-liquid interface while at the same time reducing the solid-vapour interface [91]. The total energy within the capillary (U_T) can be written in terms of θ_c as equation 4.4

$$U_T = (A_{sl} + A_{sv})\gamma_{sv} - A_{sl}\gamma_{lv}\cos\theta_0 + A_{lv}\gamma_{lv}$$
$$= U_0\gamma_{sv} - A_{sl}\gamma_{lv}\cos\theta_0 + A_{lv}\gamma_{lv} \tag{4.4}$$

where $U_0 = A_{sl} + A_{sv}$ and is a constant and the total energy of the system U_T is a function of the liquid volume V_l.
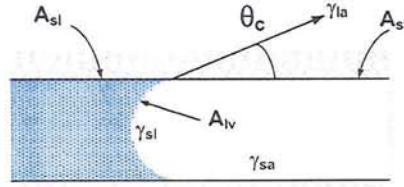
Figure 4.10: the interfacial areas of a capillary partially filled with liquid

The wetted area within the capillary increases commensurately with the volume of liquid within the capillary, and if $\gamma_{sl} > \gamma_{sv}$ then the energy of the system also increases. Given that differentiating the total surface energy with respect to the length of capillary imbibition returns the force exerted across the meniscus:

$$F = -\frac{dU}{dl}$$

then by the same reasoning the pressure across the meniscus can be found by

differentiating U with respect to the change in liquid volume V_l

$$P = -\frac{dU}{dV_l}$$

and so differentiating 4.4 w.r.t. V_l,

$$P = -\frac{dU_T}{dV_l} = U_0 \gamma_{sv} - A_{sl} \gamma_{lv} \cos \theta_c + A_{lv} \gamma_{lv}$$

$$= -\gamma_{lv} \cos \theta_c \left(\frac{dA_{sl}}{dV_l} - \frac{dA_{lv}}{dV_l} \right) \tag{4.5}$$

In uniform hydrophilic channels with $\theta_c \leq 90^0$, $A_{sv} - A_{sl}$ is constant for a constant V_l and consequently so is the pressure across the meniscus, P, that drives the fluid wetting process throughout the channel. The magnitude of P, which will now be referred to as the pressure across the liquid-vapour interface ΔP_{lv}, can be determined through the Young-Laplace equation 4.6.
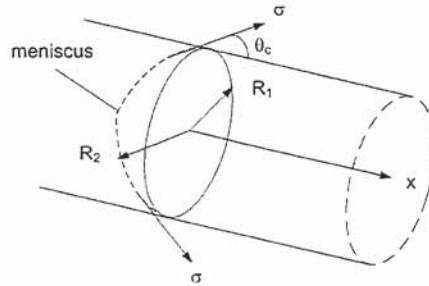
Figure 4.11: the pressure developed across the meniscus is a function of its component radii and the surface tension force and can be resolved in the direction of flow (x) by way of θ_c

$$\Delta P_{lv} = \sigma \left(\frac{1}{R_1} + \frac{1}{R_2} \right) \tag{4.6}$$

where σ is the surface tension force as a result of the surface energies, acting across two intersecting radii which describe the ovoid interfacial surface R_1 and

R_2 (figure 4.11). For a hemispherical liquid-vapour interface $R_1 = R_2 = R$ and so pressure across the meniscus resolved in the direction of fluid flow, eq. 4.6 can be written as

$$\Delta P_{lv} = \frac{2\sigma \cos \theta_c}{R} \tag{4.7}$$

where R is the radius of the hemispherical interfacial area.

From inspection of eq. 4.4 it is apparent that with $A_{sv} - A_{sl}$ decreasing with increasing V_l with a P_{lv} that varies according to the channel geometry (equation 4.7) such capillary induced fluid motion must be assessed in discrete time intervals as *'quasi-steady flow'*.

4.2.5   Laminar Flow - Hagen-Poiseuille

In fluidics, as applied to liquid flows, there are two types or natures of flow in a duct or channel - *laminar* or *turbulent*. Laminar flows are perhaps the simplest to model and evaluate having a predictable and defined flow velocity profile. The nature of a flow can be approximated arithmetically by way of its Reynolds number (R_e). Reynolds number is the ratio of intertial to viscous forces within a flow and may be calculated as

$$R_e = \frac{\rho L \bar{u}}{\mu} \tag{4.8}$$

where ρ is the density (kg/m^3), μ is the viscosity of the fluid media (kg/ms), and $\bar{u}$ is the mean flow velocity (m/s) in a channel of characteristic length L (m). In MEMS devices flow lengths L tend to be short, of the order of a few millimetres, and high mean velocities $\bar{u}$ are difficult to achieve. As such the values attained for R_e in microfluidic devices rarely exceed 10^3. Since the transition between laminar and turbulent flow occurs in the range of $1000 \geq R_e \geq 2000$ [6] it may be said that the majority of microfluidic flows are inherently laminar. Liquid phase incompressible laminar flows are often referred to as being *Poiseuille flows* in that

they meet the conditions required for analysis by way of the Hagen-Poiseuille equation. These conditions may be summarised as:

1. the channel or conduit is complete and rigid

2. the fluid is incompressible

3. the flow is non-turbulent or laminar - with a parabolic flow profile and maximum fluid velocity being twice that of the mean fluid velocity $\bar{u}$ (figure 4.12)
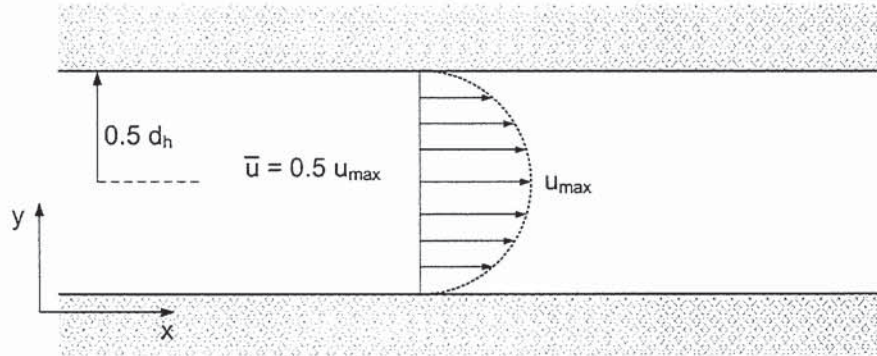
Figure 4.12: diagram of a parabolic laminar velocity profile, maximum velocity occurs at $y = d_h/2$. Mean velocity ($\bar{u}$) is half that of u_{max}.

With these conditions satisfied, and assuming that the depth (d) of the channel is small in comparison with the channel width (w), then the system can be treated as a flow between parallel plates. The Hagen-Poiseuille equation (equation 4.9) can then be used to return the pressure drop across the fluid plug between the plates as a function of mean volume flow rate (Q) and μ

$$\Delta P = \frac{12\mu l Q}{wd^3} \tag{4.9}$$

where l is the pipe length and d is the separation of the plates.

4.2.6   Newtonian Fluid

For a Newtonian fluid, such as water, flowing with a given mean velocity ($\bar{u}$) adjacent to a parallel smooth surface the relationship between the velocity of the fluid particles at a given distance (y) perpendicular to the surface is described by Newton's Law of Viscosity (equation 4.10)

$$\tau = \mu \frac{du}{dy} \tag{4.10}$$

where τ is the shear stress creating the difference in fluid velocity in adjacent fluid layers, and μ is dynamic viscosity which is a constant of proportionality that is characteristic for the fluid at a given temperature. Newtonian fluids are defined as ones that obey Newton's laws of viscosity, and for which μ has a constant value for a given temperature. Most common fluids can be considered Newtonian and have associated published reference values for μ. On a microscale the addition of particulates to the fluid can have a considerable effect on its viscosity [47], permitting particulate and fluid density to vary within the flow causing dynamic viscosity to change throughout the suspension. In such conditions the fluid may no longer be considered as being continuous nor can it be satisfactorily modelled by a single parameter model such as Newton's law of viscosity [92]. As such the models discussed here can only be reasonably assumed valid for pure fluid control tests or weak particle suspension, considerable further work is required for the mathematical determination of the behaviour of a densely populated particle suspensions.

4.3   Conclusions

In summary, two means of theoretically estimating the minimum dimension criteria for the continuum assumptions for fluid flow of gases at low pressures and liquids have been explored. The returned values for low pressure gases through both free transport models are equal. The values for liquids however are quite dissimilar, but are both smaller than values of L returned for gases. However, it is the most restrictive of these various criteria that should be used.

Fluid	small fluctuations)	bulk properties
Gas	1 μm	1 μm
Liquid	0.1 μm	3 nm

Table 4.2: estimates for minimum values of L for continuum transport models using bulk properties

Although empirical data for liquid micro-fluidic flows is scarce, the smallest dimension of a useful cell within a testicular biopsy sample is that of the head section of a spermatozoa, which is of the order of 3-5μm. According to the estimates in 4.2 fluidic channels and structures of such a scale to handle such cells are comfortably within continuum hydrodynamic flow territory, thus permitting the application of classical fluid mechanics principles for modelling the fluid flow.

Reducing characteristic dimensions have been shown to bring about a change from mass-driven flow sources to more slowly diminishing effects such as surface tension. The principal motive source in a microfluidics device is therefore likely to be induced by surface phenomena, as on capillarity. The pressures generated

as a consequence of these effects are strongly influenced by surface energies, manifested physically as contact angles, and interfacial areas. The Young-Laplace equation draws a simple relationship between mensicus radius and the pressure generated across the liquid-vapour interface by virtue of surface tension, a law that has been validated to sub-micron channel dimensions. The capillary model as a result of the energy balance across a filling capillary indicates that capillary driven flows cannot be solved as differential equations and therefore require discrete analysis, accomodating changes in boundary conditions.

The nature of a fluid flow can be determined by analysis of its Reynold's number: the ratio of flow velocity to dynamic viscosity. The small dimensions in microfluidic structures, and the low velocities bias Re to values of less than 10^3, comfortably within the laminar flow regime. This in conjunction with the rigid channels and incompressible fluid permit the assumption of Poiseuille flow.

Chapter 5

Modelling the Fluid Flow

5.1 Introduction

This chapter looks at the modelling of the fluid flow through the devices in order to characterise the behaviour of the fluid as it penetrates into a simple capillary or microchannel.

Prior work on microscale flows indicate a prevalence of capillary flow effects, it is consequently theorised that these effects will dominate until their influence is removed or the energies of the channel surfaces are balanced. It is therefore assumed that the flow will exhibit two stages of flow:

1. Capillary driven wetting - where the fluid is first introduced to the device and is driven through the system via capillary action.

2. Equalisation - fluid within the wetted capillaries is subject to a pressure imbalance induced by the surface tension of the reservoir, and the difference in gravimetric head or surface tension gradient across each wetted capillary, resulting in a bulk flow.

Modelling of the flow through the device, particularly during the wetting phase,

is necessary for identifying and predicting the source of flow velocities. Empirical measurement of any passive flows in comparison with those predicted mathematically permit the determination of flow sources, that may in turn be used for validating the passive flow concept, and the optimisation of further device designs and geometries for other applications using capillary driven flow in this way.

5.2   Concept Model

For the purposes of concept proof and evaluation the filter device can be approximated to two wells, an inlet and outlet, connected at the base via a shallow rectilinear channel (figure 5.1). A number of test devices were fabricated along with the device concepts to permit empirical evaluation of the model, and example of which is depicted in figure 5.2. A portion of the channel is populated with a number of filter structures serving to impede the progress of larger particles, briefly altering the effective hydraulic diameter of the channel and to analogise actual filtration components.
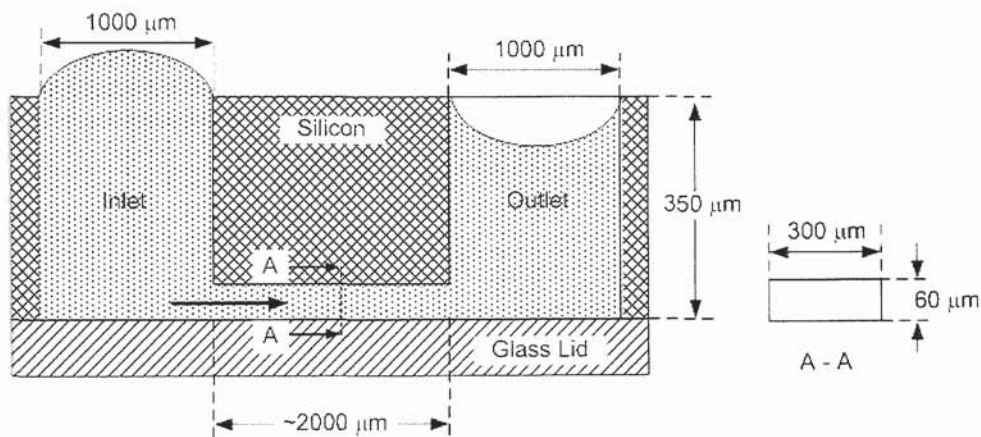
Figure 5.1: approximating the filter device to two wells etched in silicon and connected at the base by a shallow rectilinear channel
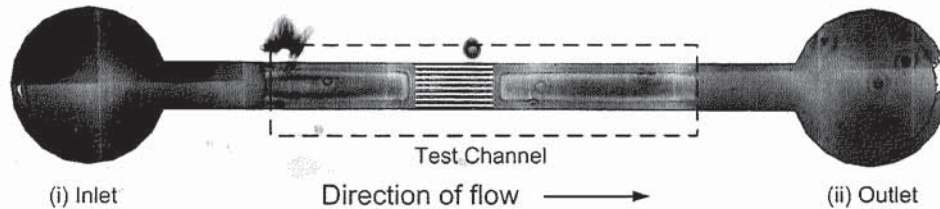
Figure 5.2: a test device as viewed from the glass underside. Comprising two of the shown channels. The channels are etched 60 μm into the surface of the silicon, and the inlet (i) and outlet (ii) are etched through the wafer. The test channel and direction of flow are indicated.

5.2.1 Capillary Action

A treatment of the mechanism behind capillary forces and effects may be found in section 4.2.2, but is summarised here. Capillary action can be considered to be a manifestation of the ratio of the cohesive to adhesive forces of a liquid. Where adhesive forces are dominant a meniscus is created across which a surface tension force acts to pull the bulk fluid in the direction of the adhesive forces. Different fluids have a different ratio of adhesive to cohesive force for given conditions and contacting surfaces, and as such the magnitude of capillary effect they produce will vary. Water, being well studied, documented and ubiquitous was chosen to serve as the basis of the fluidic models.

The majority of microfabrication and MEMS is based on the processing of silicon and its oxides [93], the proposed device is no exception to this and as such it may be assumed that the physical structure and contacting surfaces of the capillary and capillary networks as being comprised of clean silicon oxides and glasses.

5.2.2 The Capillary Model

For simplicity, the approaches to formulating capillary pressure and flow may be based on a one dimensional model comprising a single Newtonian fluid filled reservoir of finite size and capacity (ref.3 in figure 5.3), which discharges into a single linear, unobstructed microchannel (ref.2 in figure 5.3) of constant cross-section $w \times d$ and venting to atmosphere (ref.1 in figure 5.3). Surface energies of the interfaces are denoted by γ.
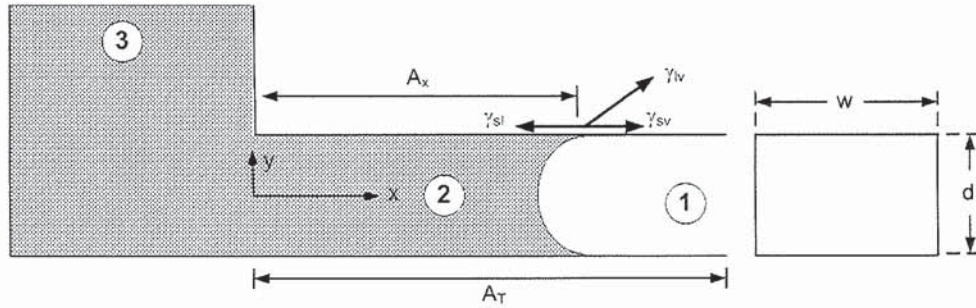
Figure 5.3: 1-dimensional model considering energies within a single capillary

5.2.3 Capillarity Induced Pressure

The Young-Laplace equation for pressure difference across an interfacial boundary between two fluids, for example a liquid and air vapour ΔP_{lv}, is

$$\Delta P_{lv} = \sigma \left(\frac{1}{R_1} + \frac{1}{R_2} \right) \tag{5.1}$$

where σ is the surface tension force acting along the boundary (N/m), and R_1 and R_2 are the two component radii which describe the liquid-vapour boundary surface (m) in figure 5.4

155
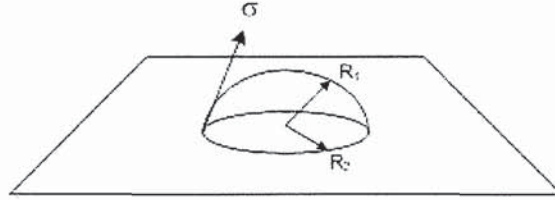
Figure 5.4: pressure across the interfacial boundary is a function of its radii and surface tension force

When considering a hemispherical boundary forming within a circular channel $R_1 = R_2 = r$ and so 4.6 reduces to

$$\Delta P_{lv} = \frac{2\sigma}{r}$$

which can be resolved in the direction of fluid flow to give the pressure across the boundary acting to advance the fluid flow front (figure 5.5 (i)).

$$\Delta P_{lv} = \frac{2\sigma \cos \theta}{r}$$

where θ is the meniscus contact angle. For cases where the droplet is enclosed within a non-circular boundary, such as a rectangular capillary, an approximation can be made where the characteristic dimensions (depth d and width w) of the boundary cross section can replace the radius term with an effective hydraulic diameter d_h (figure 5.5 (ii)) through the relation

$$d_h = \frac{4dw}{2(d+w)}$$

to give

$$\Delta P_{lv} = \frac{4\sigma \cos \theta}{d_h} \tag{5.2}$$

This enables the calculation of the pressure across the meniscus of the fluid flow front as a result of surface tension ΔP_{lv}, or *capillary action*. Since, for high aspect
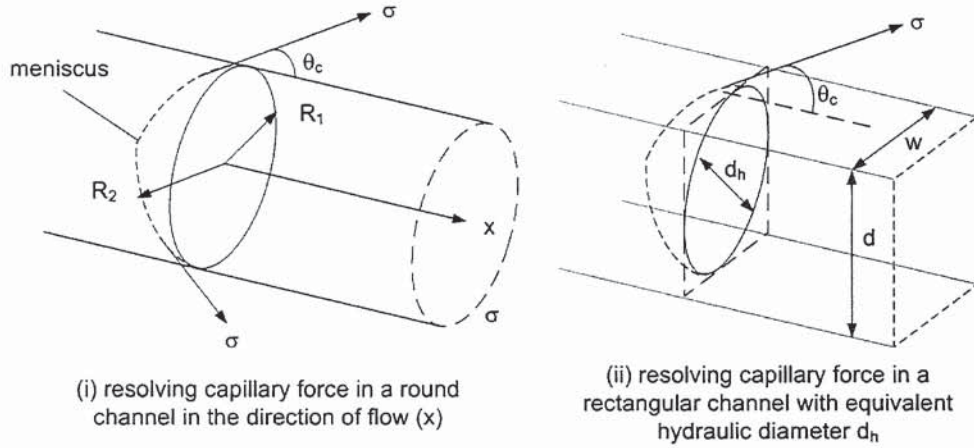
Figure 5.5: resolving the capillary force acting in the direction of flow for (i) round, and (ii) rectangular channels

ratio channels, the d_h can be aproximated to the smallest dimension, which in the case of the flow model is the depth of the etched channel (d). Allowing equation 5.2 to be rewritten as

$$\Delta P_{lv} = \frac{4\sigma \cos \theta}{d} \qquad (5.3)$$

5.2.4   Viscous Pressure

Given that an expression has been derived that describes the driving pressure of the fluid during the wetting phase (eqn. 5.3), an expression is now required that will describe the retarding pressure as a result of viscous losses.

Assuming the flow within the channel to be laminar, the pressure drop across a fluid plug of known dimensions as a result of wall shear forces ΔP_τ (N/m^2) can be determined from the Hagen-Poiseuille equation for flow between parallel

plates (equation 4.9).

$$\Delta P_\tau = \frac{12\mu l Q}{wd^3} \tag{5.4}$$

where μ is the dynamic liquid viscosity (m^3/s), l is the length of the liquid plug, Q is the volumetric flow rate (m^3/s) and w and d are the width and depth of the channel. The flow rate Q can be expressed in terms of fluid velocity $\dot{l}$ as

$$\dot{l} = \frac{Q}{wd} \tag{5.5}$$

returning equation 5.4 as

$$\Delta P_\tau = \frac{12\mu l \dot{l} wd}{wd^3}$$

$$\Delta P_\tau = \frac{12\mu l \dot{l}}{d^2} \tag{5.6}$$

5.2.5   Washburn's Equation for Capillary Imbibition

Widely applied in capillary [94] and microfluidic modelling is the Lucas-Washburn equation for capillary imbibition. Originally intended as a simulation model for the ingress of a fluid into a porous substrate the equation assumes a material to be comprised of a number of round capillaries of diameter d and considers the fluid progression as a function of time t. The Lucas-Washburn equation has found widespread application in the modelling of microfluidic capillary structures, and has spurred a number of derivations [37], [38], [41]. The momentum of a fluid flowing in a capillary can be written as

$$F(t) = \dot{m}(V_2 - V_1) \tag{5.7}$$

where F is the force exerted in unit time (t) producing the velocity change between V_1 and V_2 in a fluid element of mass flow rate $\dot{m}$. The force F can also be written as $P \times A$ where P is the pressure change induced by, or which induces, the velocity

change and A is the cross sectional area of the duct. Thus enabling equation 5.7 to be written as

$$F(t) = \dot{m}(V_2 - V_1) = (P_2 A_2) - (P_1 A_1) \tag{5.8}$$

Applying the principle of conservation of momentum to a rectangular channel of uniform cross sectional area (A), if we assume that when wetting at constant velocity $(V_2 = V_1)$ then the sum of the forces acting on the fluid, the capillary force across the liquid-vapour interface (F_{lv}) and the retarding viscous shear force (F_τ), is zero

$$F_{lv} - F_\tau = 0$$

which may in turn be rewritten as

$$\Delta P_{lv} A = \Delta P_\tau A \tag{5.9}$$

assuming A is constant the areas cancel enabling a direct substitution for equations 5.6 and 5.3 into equation 5.9. This gives

$$\frac{4\sigma \cos \theta}{d} = \frac{12 \mu \dot{l} l}{d^2}$$

which when rearranged for $l\dot{l}$ and integrated with respect to time t returns a modified version of the Washburn equation for fluid imbibition distance l into a horizontal capillary of rectangular cross section.

$$\int l\dot{l}\, dt = \int \frac{4\sigma \cos \theta d}{12 \mu}\, dt$$
$$\frac{1}{2}l^2 = \frac{\sigma d \cos \theta t}{3\mu} + C \tag{5.10}$$

when $t = 0$, $l = 0$, so $C = 0$ and thus equation 5.10 can be written as

$$l = \sqrt{\frac{2\sigma d \cos \theta t}{3\mu}} \tag{5.11}$$

159

This modified Lucas-Washburn equation indicates that providing the assumption of poiseuille flow is upheld, viscous and surface forces predominate over inertial forces, and there are no external forces acting on the fluid, then the penetration distance of the fluid into a channel is proportional to the square-root of time.

$$l \propto \sqrt{t}$$

5.2.6   Effective Contact Angle for Compound Structures

Microfabricated channels etched into bulk silicon are typically enclosed by bonding the wafer bearing the channels to another wafer of silicon, one of its many nitrides, or glass. As such, there are typically a minimum of two different surfaces contacting the fluid within a closed capillary (figure 5.6). Assuming the channels are etched into bulk silicon and sealed with glass, this introduces two different surfaces with differing surface energies and subsequently differing static contact angles θ_1 and θ_2. The static contact angles of these surfaces will contribute to an effective static contact angle θ_c to a degree commensurate with their area of fluid contact.
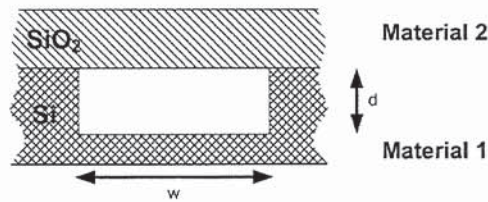
Figure 5.6: schematic diagram of a microfabricated channel in silicon

Considering the capillary section in figure 5.6, comprising a glass cover of width w and static contact angle θ_2, and a silicon trench of width w, depth d and static

160

contact angle θ_1, the cosine of the effective contact angle can be expressed as

$$\cos \theta_c = \frac{(2d + w) \cos \theta_1 + w \cos \theta_2}{2(d + w)} \tag{5.12}$$

which may be simplified by collecting terms for d and w and defining the coefficients α and β

$$\alpha = \frac{2d + w}{2(d + w)}$$
$$\beta = \frac{w}{2(d + w)}$$

returning 5.12 as being

$$\cos \theta_c = \alpha \cos \theta_1 + \beta \cos \theta_2 \tag{5.13}$$

which when substituted into 5.11 yields an equation relating capillary imbibition distance l with the surface tension force σ and the combination of the contact angles for the two adjacent materials.

$$l = \sqrt{\frac{2d\sigma(\alpha \cos \theta_1 + \beta \cos \theta_2)t}{3\mu}} \tag{5.14}$$

Yang *et al* [37] derive an expression with the intention of determining the internal surface properties of a micro-channel quantifying values such as γ_{sv} and γ_{lv} (eq. 5.15). Effectively a variation on the Washburn equation it differs in that it incorporates any possible head pressure as a result of filling the channel from an elevated reservoir, and extends its application to flow displacements and velocities at intermediate time steps. The Yang expression was derived from considering a one dimensional flow in a horizontal capillary, filling from an elevated source, with a parabolic meniscus profile (figure 5.7).

The Yang model introduces a diffusion coefficient, D, in order to calculate the meniscus progression from an initial position l_0 in a micro-channel in a time
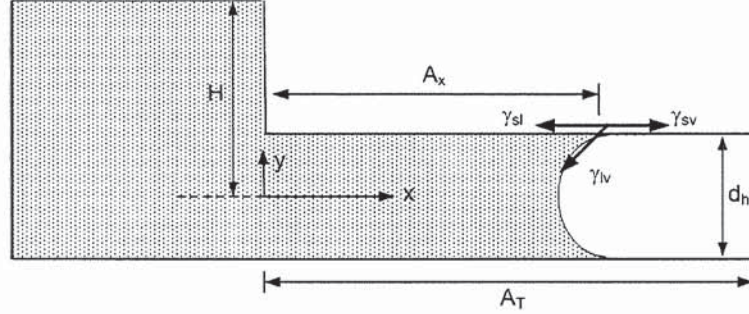
Figure 5.7: schematic diagram of the Yang model, with liquid from an elevated reservoir filling a uniform capillary: indicating surface energies, and areas.

interval t, with the addition of a gravimetric pressure term ($\rho g H$) (eq.5.15) where H is the height of the inlet fluid above the level of the channel.

$$l(t) = \sqrt{l_0^2 + Dt}; D = \frac{d_h^2}{4\mu}\left[\rho.g.H + \frac{2(\gamma_{sv} - \gamma_{sl})}{d_h}\right] \tag{5.15}$$

The model has been proven to hold for channels of high aspect ratio, i.e. where one dimension of the channel section is much greater than the other [37], and in such cases, it is sufficient to apply only the smaller of the dimensions as d_h rather than the equivalent hydraulic diameter. By this reasoning, if we substitute the D in equation 5.15 for the previously derived equation for flow between parallel plates (equation 5.11) we obtain a model for the wetting flow through a high aspect ratio channel.

$$l(t) = \sqrt{l_0^2 + Dt}; D = \frac{d^2}{3\mu}\left[\rho.g.H + \frac{2(\gamma_{sv} - \gamma_{sl})}{d}\right] \tag{5.16}$$

5.2.7 Applying the Modified Washburn Equation

Bouaidat *et al* also derive and apply a model similar to Yang, but rather than for finding surface properties it is used for the determination of flow parameters

in what is an unsealed microfluidic channel. The model incorporates the contact angles of the adjacent surfaces in a compound contact angle expression, as in equation 5.12.

As the Bouaidat model can be applied to the prediction of flow velocities, it is reasonable to assume that a similar relationship could be applied to determining the flow parameters of the device concept model. In the case of a sealed capillary, the surface energies γ_{sv} and γ_{sl} are not easily measured or determined. However a relationship may be derived from Young's law (eq. 5.17)

$$\gamma_{sv} = \gamma_{sl} + \gamma_{lv} \cos \theta_c \tag{5.17}$$

where θ_c is the static contact angle the liquid-vapour interface makes with the channel wall, which may be calculated from equation 5.12. Substituting 5.17 into 5.16 returns the following expression for D

$$D = \frac{d^2}{3\mu} \left[\rho.g.H + \frac{2(\gamma_{lv} \cos \theta_c)}{d} \right] \tag{5.18}$$

Since the volume of the channel in the proposed device is small in comparison to that of the inlet reservoir, and the radius of the inlet reservoir is greater than its height, H can be assumed constant. Which when finding for local velocity, $v(t) = dl/dt$

$$v(t) = \frac{D}{2\sqrt{l_o + Dt}} \tag{5.19}$$

where l_0 is the initial offset in meniscus progression at time $t = 0$.

Forming an expression that may be applied to serially model the device concept, with varying boundary conditions for d and l_0 in order to account for fluctuations in channel diameter as a consequence of geometrical changes. This model was adopted for the wetting model for evaluating the wetting induced flows within the microfabricated devices.

5.2.8   Validating the Wetting Model

Erickson *et al* indicates that the previously derived Washburn equation model (equation 5.11 in Section 5.2.5) predicts the total wetting time for imbibition of liquid into non-uniform capillaries despite local changes in velocity [40]. As such the rearrangement of eq. 5.20 for θ_c and substituting in the time taken for the fluid to progress to the end of the test device channel should provide an indication of the surface contact angle. This can then be used as an estimation for the purposes of the wetting model, avoiding the need to disassemble a device and attempt to measure the inner surface θ_c directly.

$$l = \sqrt{\frac{2\sigma d \cos\theta_c t}{3\mu}} \tag{5.20}$$

where l is the penetration distance within time t. Rearranging equation 5.20 for θ_c gives

$$\arccos(\theta_c) = \frac{3\mu l^2}{2d\sigma t} \tag{5.21}$$

Substituting published values for surface tension ($\sigma = 7.36 \times 10^{-2}$ N/m) and dynamic viscosity ($\mu = 1.005 \times 10^{-3}$ kg/ms) at $20°C$ [95] into equation 5.21, along with the experimentally measured imbibition time of 0.12 s gives an estimate for contact angle within a test device of the order of 86.5°. Published data on silicon contact angles is scarce as a result of its high variability and the degree to which it is affected by chemical agents. However, this is considerably higher than specific published values for DRIE processed silicon and glass of 9° and 25° respectively [96]. Native silicon oxides typically exhibit a higher contact angle of 20-30°, but other sources suggest values for θ_c for silicon as high as 70-75° [97].

The boundary conditions of the test device, shown in figure 5.8, were applied to the modified Washburn model (equation 5.19) in order to create a velocity profile of flow through the test device which would be comparable to empirically

164

measured flow velocities.
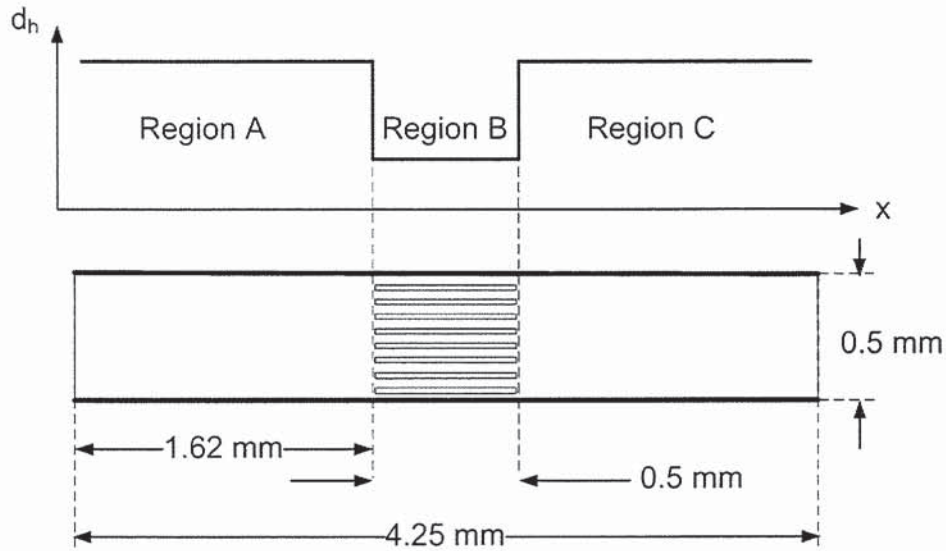
Figure 5.8: schematic of the test device showing changing geometric conditions with increasing 'x'

The velocity profile for the initial wetting period captured at an optimal capture rate of 86 Hz (11.6 ms intervals) returned the capillary wetting velocity profile as shown in figure 5.9. **The specific procedures for measuring flow velocities may be found in Section 6.3.** The plot demonstrates how the fine elements of the filter serve to slow meniscus progression suggesting that the change in meniscus radius is less than that in fluid friction. Comparing the measured meniscus velocity during the wetting phase with that calculated by the wetting model shows a strong agreement when substituting a contact angle of 86.5° (figure 5.9).

Comparing calculated meniscus velocity profile against measured velocity data
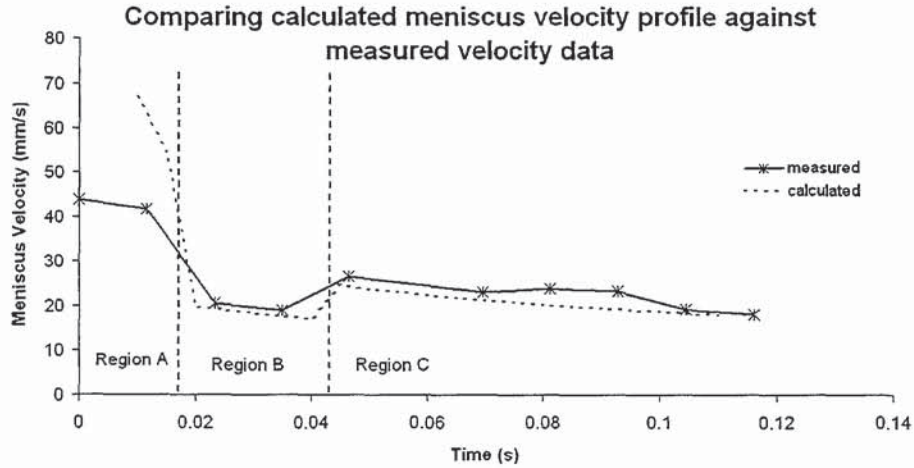
Figure 5.9: the velocity profile of the wetting meniscus subtended by the model shows a clear correlation with the experimental velocity profile.

The initially infinite velocity of the meniscus as predicted by the wetting model is a known flaw in the Washburn model, but the subsequent trend shows a good reflection of measured events in both velocity magnitude and timing, thereby validating the wetting model for the application of determining wetting velocity based on channel geometry.

5.3   Geometric Effects

5.3.1   Wetting

The wetting model indicates that changes in geometry can have a significant impact on the capillary wetting phenomenon. Through careful design of the bifurcating faces of a widening section of microchannel pressure barriers can be established that behave much like conventional stop or burst valves. Man *et al* [84] use the converging and subsequent axially widening profile of a $200\mu m$ wide

and $20\mu m$ high microchannel to establish a region of elevated interfacial pressure across the fluid meniscus which must be overcome mechanically or thermally in order to restore flow. According to the Young-Laplace equation 4.6 the pressure across a liquid meniscus is inversely proportional to its radius:

$$\Delta P \propto \frac{1}{r}$$

and so the smaller the radius of a droplet, or meniscus within a section of microchannel, the higher the pressure generated across it. This is a consequence of the surface of a fluid droplet striving to attain its lowest energy state, and is the same mechanism by which a fluid progresses into a capillary. It has already been established that a fluid will progress into a horizontal and uniform capillary structure providing the static contact angle is $< 90^0$. If a step change in the geometry of the capillary is introduced with respect to the fluid flow front that artificially increases the static contact angle through the introduction of an offset then a condition arises where the fluid will be arrested via a premature equilibrium state (figure 5.10).
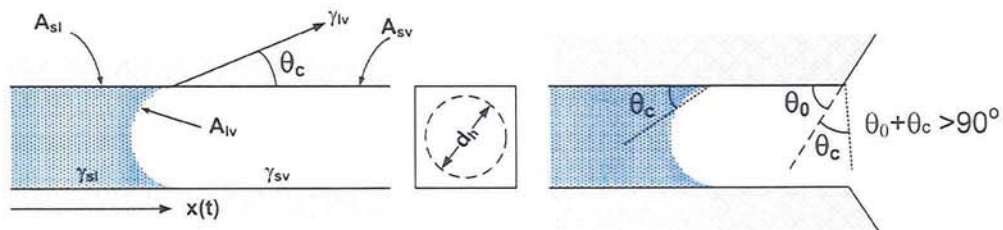
Figure 5.10: introducing a step change in capillary geometry can change the nature of the surface from hydrophilic to hydrophobic ($\theta_c > 90^0$)

167

The pressure inducing capillary uptake can be expressed as:

$$P = -\gamma_{lv} \cos \theta_c \left(\frac{dA_{sl}}{dV_l} - \frac{dA_{lv}}{dV_l} \right) \tag{5.22}$$

where A_{sl} is the area of the solid-liquid interface over which γ_{sl} acts, and A_{lv} is the area of the solid-vapour interface over which γ_{lv} acts. In uniform hydrophilic channels with $\theta_c \leq 90^0$, $A_{sv} - A_{sl}$ is constant, and hence a constant pressure across the meniscus P drives the fluid wetting process throughout the channel. If, however, the channel walls bifurcate and dA_{lv}/dV_l change at the same rate as dA_{sl}/dV_l then P will fall to zero and flow will stop until some additional externally acting force is applied. If dA_{lv}/dV_l increases at a rate greater than dA_{sl}/dV_l then the pressure will reverse and flow will be abruptly arrested and a much larger external pressure would be needed in order for flow to continue. Conversely, if the channel walls converge then the pressure will increase asymptotically, inducing a faster fluid progression. This will continue until such a point as when dA_{lv}/dV_L is negligible in comparison with dA_{sl}/dV_l.

5.3.2   Filter geometry

The geometry of the channel and filter elements also affect fluid flow beyond the wetting flow-front. Through studying the way that the fluid flows through the filter elements an optimal separation mechanism can be devised that minimises the opportunities for particles to be arrested within the filters, or within regions of stagnated fluid flow. In order to quickly assess a variety of flow paths, obstacle patterns and morphologies a series of Computational Fluid Dynamic (CFD) simulations were conducted to indicate flow and subsequently particle behaviour.

5.3.2.1   Pillars - size and packing density

Of initial concern was the identification of the attenuation of the fluid flow as a consequence of the introduction of filtration elements. An initial model was constructed of the fluid within a test device post-wetting, and the initial pillar elements of the 'A' concept device were incorporated into the flow path. The fluid was specified to be consistent with the bulk properties of water at $22°C$, and under the flow and boundary conditions as summarised in table 5.1. A data collection point was selected along the centre-line of the flow downstream of the filters and used as a reference flow attenuation as a consequence of the filter elements (figure 5.11).

Property	Value
Inlet velocity (m/s)	0.02
Fluid density (kg/m³)	998.2
Fluid viscosity (kg/ms)	1.007×10^{-3}
Inlet pressure (Pa)	0
Outlet pressure (Pa)	0
Bulk modulus (Pa)	2200×10^6

Table 5.1: fluid reference conditions for the filter packing density models
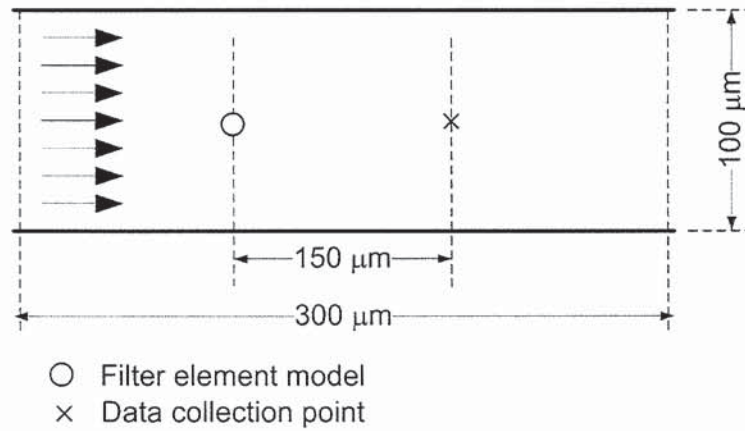
Figure 5.11: a simple microchannel model used to observe the effects of filter element size and packing density

Mesh independence was established for all CFD models, with a minimum of two different meshes being tested for consistency for each study. Table 5.2 shows the mesh independence results for the 5 μm element model as an example (V_x is the fluid velocity component at the data collection point parallel to the channel walls). An example mesh of that used in the studies is shown in figure 5.12. Firstly a single cylindrical filter element was located along the centreline of the channel and a number of CFD studies were made in order to evaluate the effect of the filter element size, representing up to 40% occlusion of the channel, on the downstream velocity. The study showed that there was an approximate linearly decaying relationship between downstream fluid velocity and element size (figure 5.13).

The effect on changing the pitch and spacing of successive arrays of filter elements within the channel was then studied. An appreciation of any negative effects of filter element population pitch and spacing would aid in the design of filter stages so as to offer the least hydraulic resistance to the wetted flows. A single linear array of circular filter elements was maintained at a constant diameter of 10 μm

170

number of elements	V_x at data point (m/s)
4801	0.0205
5125	0.0204
7195	0.0202

Table 5.2: the fluid velocity at the data collection point as collected with various element numbers to illustrate mesh independence.
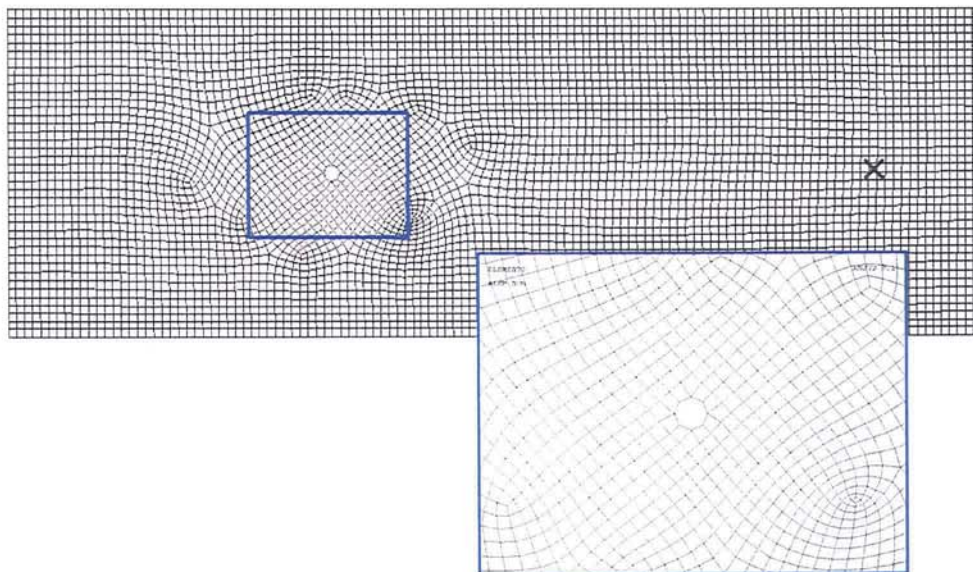
Figure 5.12: an example of the CFD mesh as employed in the single element diameter study.

171

Effect of the diameter of a circular obstruction on the downstream velocity of water in a microchannel
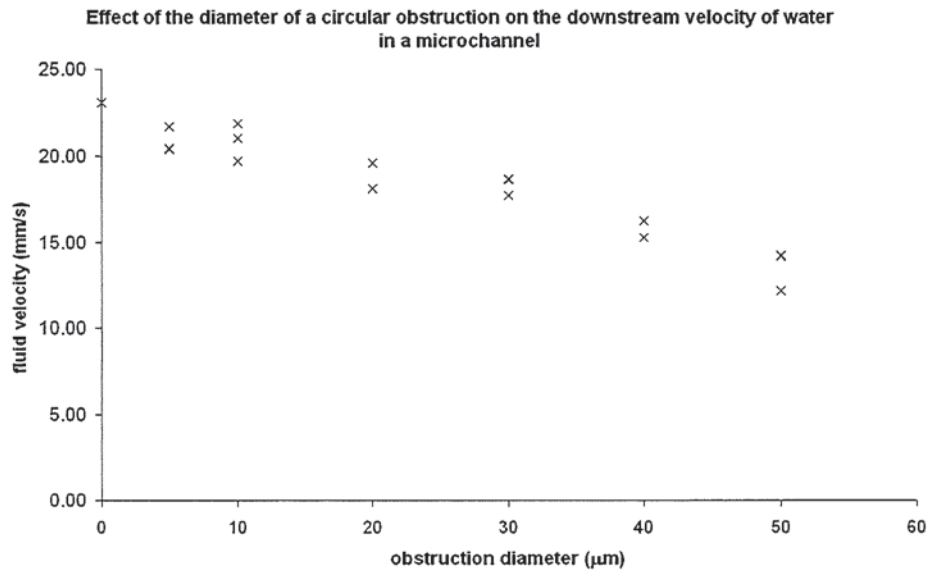
Figure 5.13: increasing the size of the filter element exhibits an approximately linear relationship with downstream peak velocity

and equally spaced across the width of the micro-channel. The results of this series of simulations are illustrated in figure 5.14.

Effect of the pitch between filter elements on downstream fluid velocity of water flowing through a microfilter
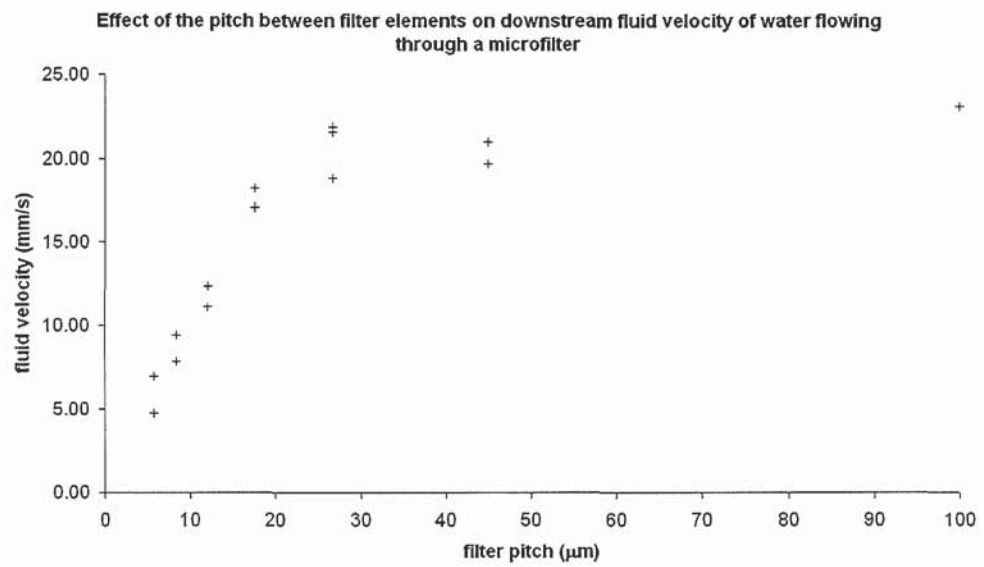
Figure 5.14: increasing the filter pitch above 20 μm illustrates a linear relationship between pitch and downstream velocity, lower interpillar spacings have a more pronounced effect

Finally, successive filter array spacings were studied on both the effect of the number of filter arrays, and the spacing between them using the adaption of the model as depicted in figure 5.15. A baseline, having been established with the previous element pitch investigation, was selected of 5 equispaced elements per column array, with each element being 10 μm in diameter. Multiple studies were then made of the flow through the channel with an increasing number of arrays at a regular spacing of 15 μm, and finally with 3 arrays at a variety of spacings. The results are summarised in figures 5.16 and 5.17.
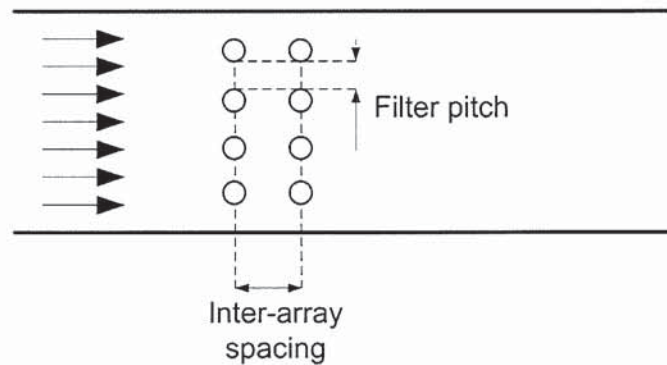
Figure 5.15: a variation of the CFD model with various numbers of filter arrays and inter-array spacings

From the CFD studies into the effect of changing the filter element packing density it is apparent that the most prominent effects come about as a result of the filter pitch and the element size. Increasing the number of arrays beyond two has negligible effect on the flow, but an optimal solution would have a single array as this offers a much higher downstream velocity. Smaller element sizes also offer less resistance to fluid flow than larger elements, but element size must be optimised against etch aspect ratio in order to ensure good manufacturing yield.

Effect of the number of filter arrays at 15 μm inter-array spacing on the downstream fluid velocity
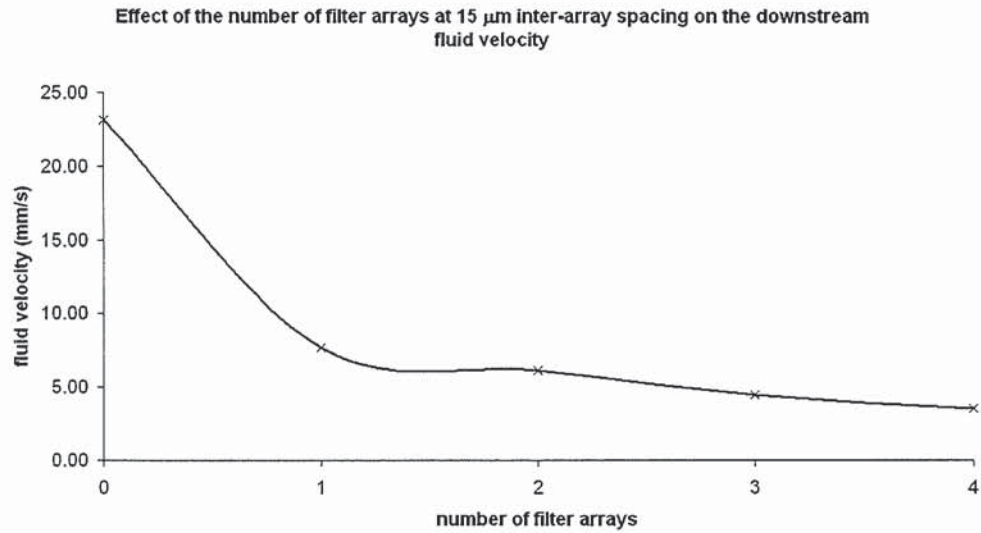
Figure 5.16: increasing the number of filter stages beyond two identical arrays with a separation of 15 μm has little effect

Effect of the inter-array filter element spacing on the downstream fluid velocity
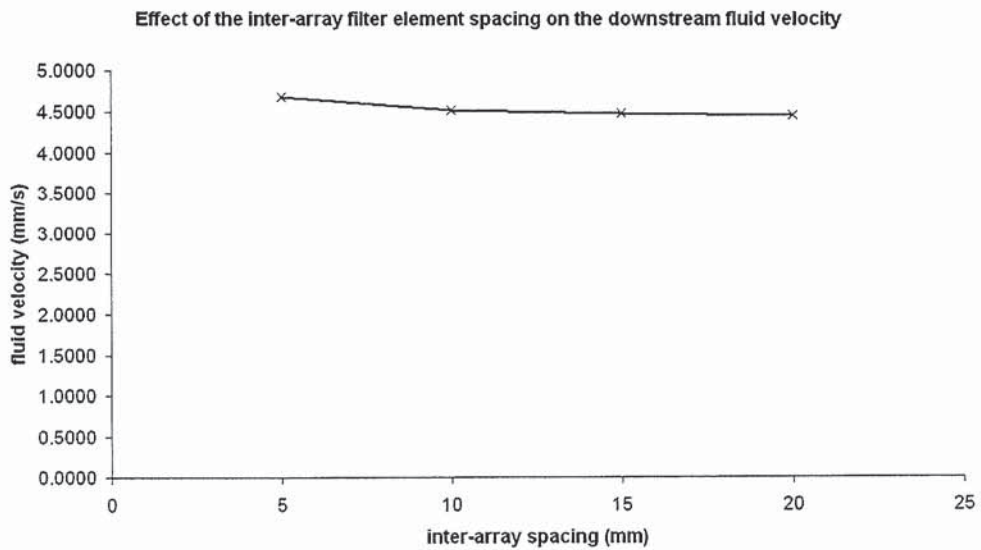
Figure 5.17: as the spacing between successive filter arrays is increased there is a gradual decrease in downstream velocity

5.3.2.2 Filter Element Morphology

Having established the effects of patterning or repeating a circular filtration element within the CFD capillary model further studies were undertaken in order to gain an appreciation of the way in which the fluid will interact with the individual elements and arrays of elements under expected flow conditions. Such analysis would yield indications of relative flow attenuation, and indicate regions of flow arrest that could potentially trap particles within solution.

The model was based on the test device, a single linear channel populated with an array of filter elements equispaced at 30 μm throughout the 500 μm centre section of the 1500× 300 μm channel. Filter elements representative of each of the device concepts were incorporated, and are summarised in table 5.3. The flow model and fluid environment were consistent with those used in the previous studies, however the velocity was attentuated to a steady flow of approximately 6 mm/s as suggested by flow rate experiments (Section 6.5.2). All walls and obstructions were given a no-slip zero velocity condition, since microfluidic flows are known to have negligible slip [47]. The model as employed for the first study, 'pillars_1', is shown in figures 5.18 and 5.19, and was modelled using ANSYS 8.1 Flotran with 2-D CFD elements. A coarse mesh of 15 μm elements was constructed across the model, which was locally refined to approximately 2-3 μm to give 24000 elements across each model.

Model	Concept	Description
pillars_1	A, A2, E, H	regular array of round pillars
pillars_2	B, B2	irregular array of round pillars
channels_1	C, C2, B3, H	equispaced linear walls

Table 5.3: CFD filter element models that were developed were intended to be representative of the concept devices
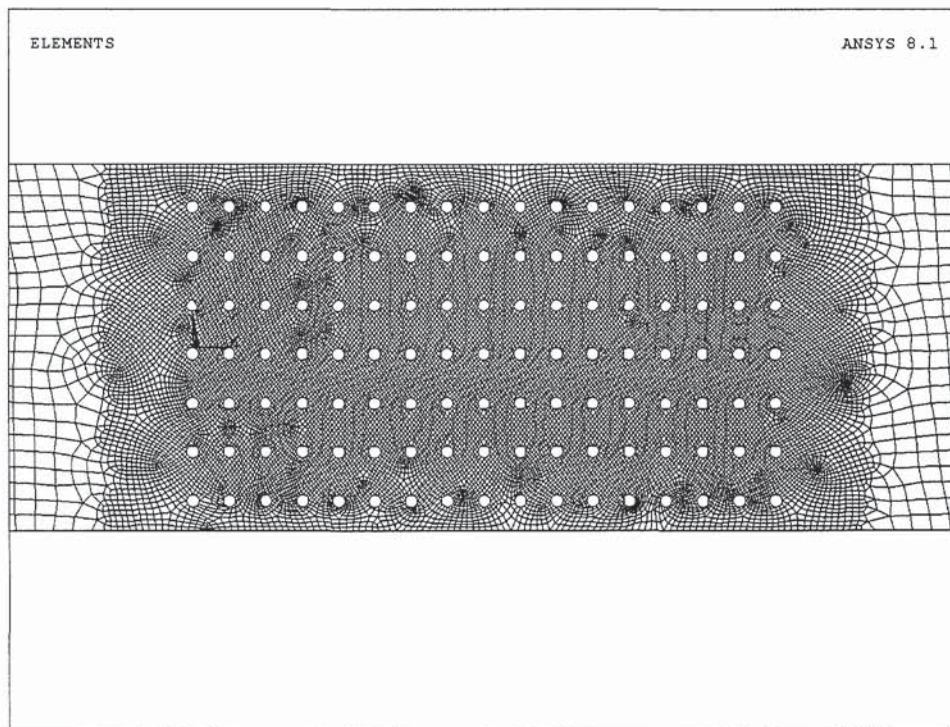
Figure 5.18: filter region of the pillars_1 model, showing the 10 μm diameter pillars within the channel
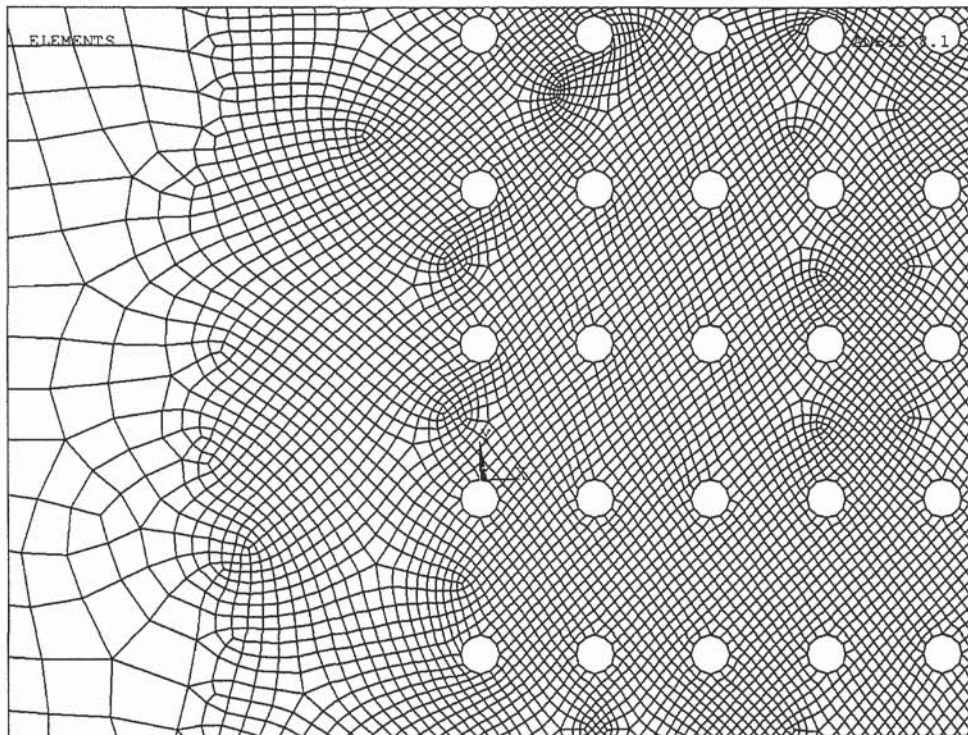
Figure 5.19: closeup of the pillars_1 model, with the coarse channel elements and the fine filter region elements

The velocity vector diagrams of each model produced by the solver were studied in order to identify regions of low flow velocity both through the filter and around each filtration element. Representative flow-field images from each study are shown in figures 5.20, 5.21 and 5.22.
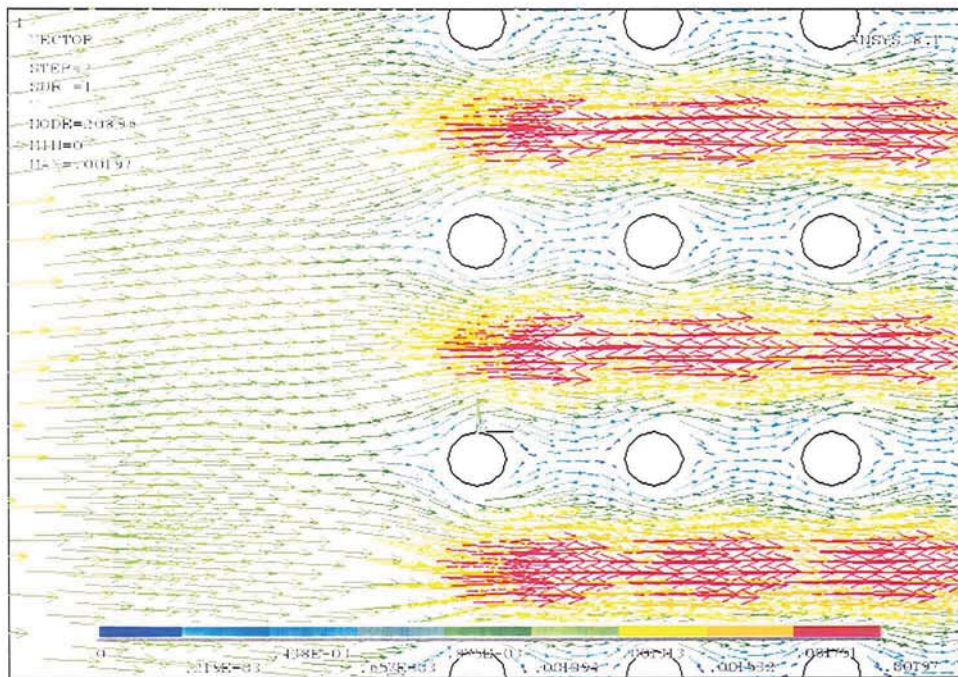
Figure 5.20: velocity vector field around the regularly spaced filter elements indicate low velocity regions after each pillar that could arrest and trap desired particles in suspension

The CFD analysis is by definition an approximation of actual flow, dependent as they are on the resolution of the elements comprising the fluid model, and the fluid properties and constraints applied, but this is even more so when non-Newtonian effects such as particulate flows are to be considered. However the
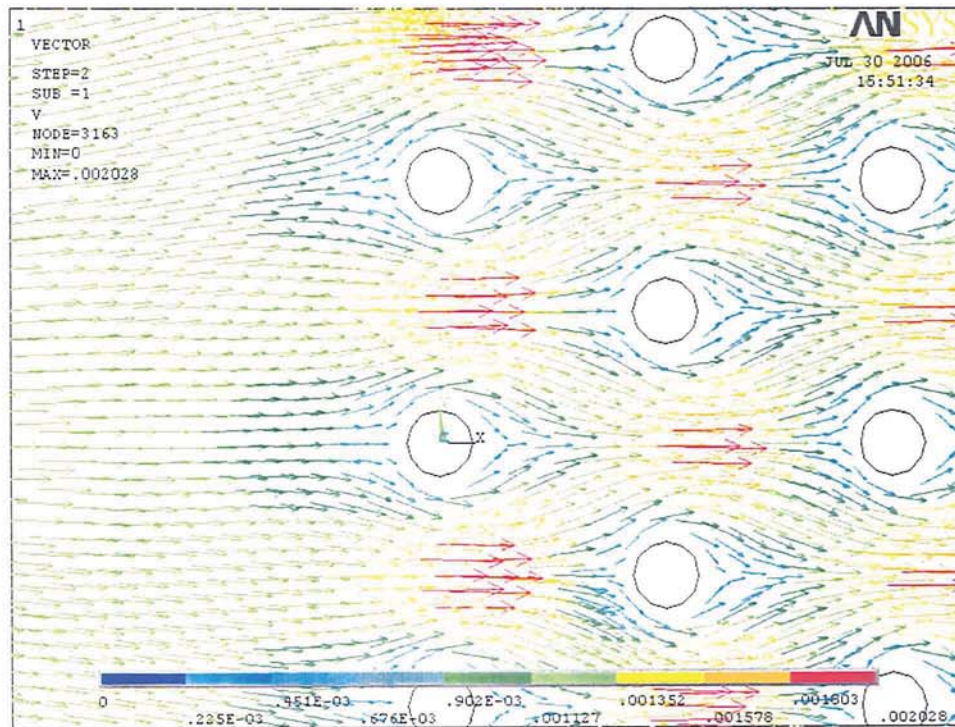
Figure 5.21: velocity vector field around the irregularly spaced filter elements show that a tortuous flow path with low velocity regions offer an increased probability of small particles arresting
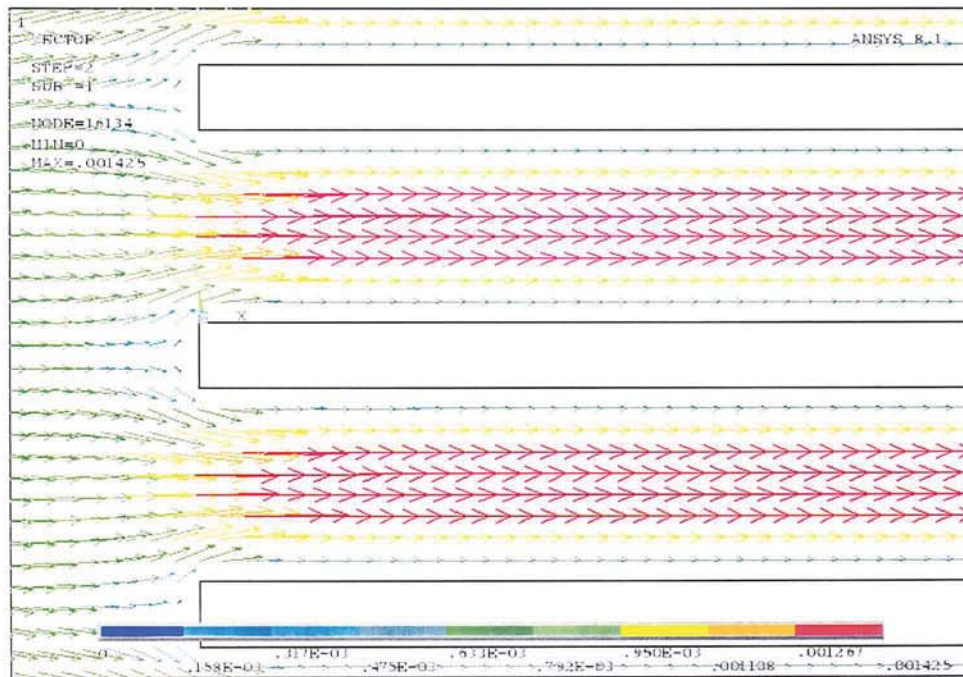
Figure 5.22: velocity vector field through the linear filter structures have a lower peak velocity but have a fewer low velocity regions for particles to slow and arrest

velocity vector fields around the elements within the studied models indicate that the previously preferred redundant fluid pathways offered by the discrete pillar element concepts may have considerable drawbacks in their application to an unpowered particle filter.

The studies illustrated regions of low velocity immediately behind the filter elements, equivalent to as much as 80% of the filter element diameter. In the case of the regularly arrayed elements in pillars_1 (figure 5.20) the entire region between successive filter elements was subject to a maximum of 22% of the peak flow velocity, with much of the region exhibiting less than 10% of the bulk flow velocity. The irregularly arrayed elements of pillars_2 (figure 5.21) showed attenuated flows of a similar degree but these effects were more localised to immediately around the elements themselves. However, the more tortuous flow paths through these elements increase the opportunity for particles in suspension to find their way to these regions.

This considered, the most effective filter morphology from the point of view of fluid flow would appear to be that of the linear channels featured in devices 'C2', 'B3' and 'H'. Thus providing a counterpoint argument to the increased opportunity for flow arrest through blockage in these devices. Despite exhibiting a lower peak velocity, there are few regions of low velocity and no slow moving fluid flows that could trap particles within the filtration elements (figure 5.22) thereby considerably reducing the chances of smaller particles becoming trapped within the filter stage, inaccessible to the user.

5.4 Gravity Driven Viscous Flow

Once a capillary system has completed the wetting phase the forces induced by the moving meniscus are no longer present, but this may not necessarily bring about a cessation of the flow as there are conditions under which the system are still unbalanced. According to the momentum balance equation 5.23 when the capillary force term is removed then the viscous retardation force is also zero. This force is caused by shear forces within the fluid as a result of differences in fluid velocity at the centre of the channel and at the walls of the channel. Cohesive bonds between the fluid particles act in opposition to the fluid flow, attempting to retard the flow until the flow is arrested. As such whilst the fluid is flowing there must still remain a viscous force component present acting on the fluid.

$$F_{cap} - F_{visc} = 0 \qquad (5.23)$$

5.4.1 Revising the capillary model

Considering a capillary that is supplied with fluid from an elevated reservoir and drains to an outlet port (see figure 5.23), or one that is subject to a gravimetric head then there is still a potential source of motive force. If a pressure balance of the system was taken about the capillary along the section line A-A there are the following components:

1. This is the hydrostatic head associated with the primary reservoir (1) wherein the fluid meniscus is at an elevation of h_1 above the channel. The pressure at A-A as a consequence may be found by

$$P_1 = \rho g h_1 \qquad (5.24)$$

where P_1 is the pressure component at A-A due to the fluid of density ρ being elevated to a height of h_1 above the channel against gravity g.
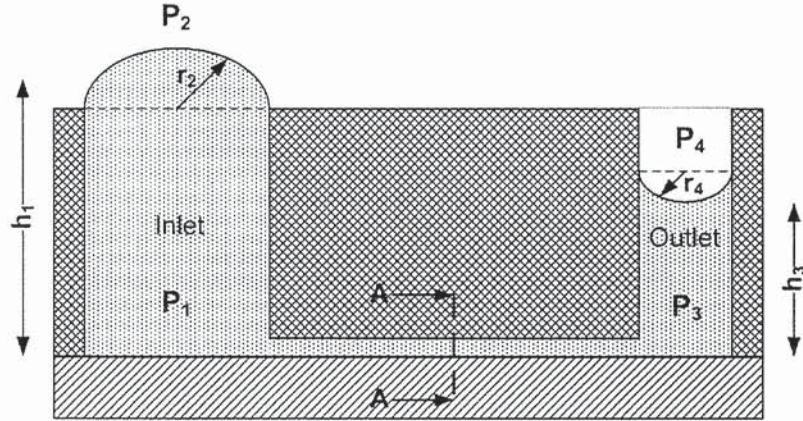
Figure 5.23: taking fluid pressure balance about a capillary section A-A between two fluid volumes

2. An additional pressure acts across the meniscus of the fluid as a consequence of the fluid surface tension as calculated by Young-Laplace (equation 5.25)

$$P_2 = \frac{2\sigma}{r_2} \tag{5.25}$$

where it is assumed the meniscus is hemispherical, r_2 is the radius of the meniscus, and σ is the surface tension force acting across the liquid-vapour interface.

3. As for P_3, this is the pressure component at A-A due to the elevation due to the meniscus being elevated a distance of h_3 above the channel subject to an acceleration of g - gravity.

$$P_3 = \rho g h_3 \tag{5.26}$$

4. Finally this is the pressure across the hemispherical meniscus of radius r_4 in the outlet port.

$$P_4 = \frac{2\sigma}{r_4} \tag{5.27}$$

Substituting these terms into an overall expression for the system about A-A

$$
\begin{aligned}
\Delta P_{A-A} &= P_1 + P_2 - P_3 - P_4 \\
&= \rho g h_1 + \frac{2\sigma}{r_2} - \rho g h_3 - \frac{2\sigma}{r_4} \\
&= \rho g (h_1 - h_3) + 2\sigma \left(\frac{1}{r_2} - \frac{1}{r_4} \right)
\end{aligned}
\tag{5.28}
$$

This suggests that there will continue to be a pressure difference across A-A (ΔP_{A-A}) until both ($h_1 - h_3$) and ($r_2 - r_4$) are zero. However, this can only hold if r_2 and r_4 are known to work in direct opposition and can both adopt the same radii.

5.4.2   Finding the nature of P_4

Capillarity theory indicates that a fluid will rise against gravity in a capillary until an equilibrium is found where the mass of raised fluid is equal to that of the capillary rise force (figure 5.24(i)). This force is calculated by

$$
F = \sigma \cos \theta_c \times \pi d_h
\tag{5.29}
$$

where $\cos \theta_c$ is the upward component of the surface the surface tension force σ acting at the static contact angle multiplied by the perimeter of the capillary ($\pi \times d_h$ - hydraulic diameter).

If we assume that the outlet port is simply a large capillary with hydrophilic sidewalls (figure 5.24(ii)). This translates to a maximum possible weight of fluid that can be raised up the outlet port through capillary action

$$
W = \rho g (\pi/4) d_h^2 h_4
\tag{5.30}
$$

where W is the weight of the fluid column and h_4 is the elevation of the meniscus above the outlet of the connecting capillary. Rearranged for h_4 and substituting
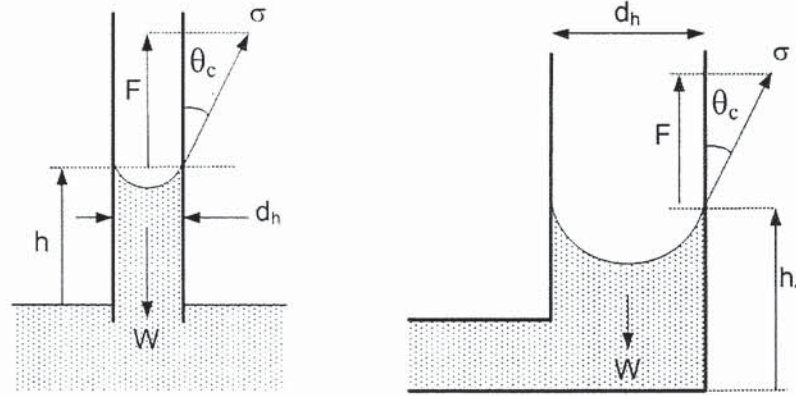
(i) capillary rise against gravity   (ii) outlet acts as capillary

Figure 5.24: (i) fluid will rise against gravity within a capillary as a result of surface tension, (ii) considering the outlet well to be an upright capillary will also result in fluid to rise against gravity

F for W this gives

$$h_4 = \frac{4\sigma \cos \theta_c}{\rho g d_h} \tag{5.31}$$

So, as the outlet port begins to fill it will be as a consequence of an assisting force F and the pressure differential due to $h_1 - h_3$ until either h_3 or h_4 is exceeded. After this time any further flow will be a direct consequence of P_4. In the event that h_4 cannot be exceeded then in order to obtain an equilibrium state the nature of P_4 will need to change from assistive to counteractive: it must work in direct opposition to the remaining pressure source P_1 (figure 5.25).

The mechanism by which this occurs can be found by referring back to the revised capillary model (figure 5.23). At the exit of the outlet well there is a change in port diameter that can be approximated to a step increase of infinite size ($\Delta d \sim \infty$) (figure 5.26). Assuming the static contact angle is constant for the capillary material, both within and on the surface around the capillary, there is
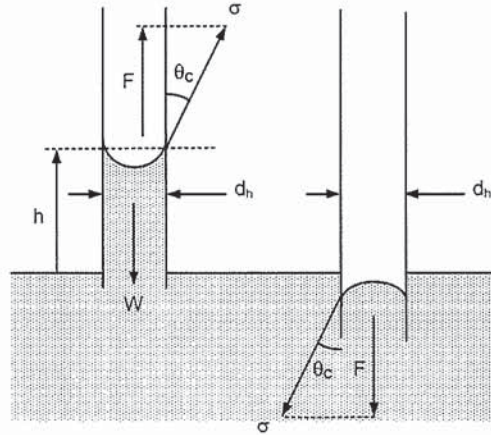
Figure 5.25: Contact angle affects the nature of the interfacial pressure, assistive and non-assistive

a geometrical offset in the static contact angle θ_c of 90^0 at the exit of the outlet.
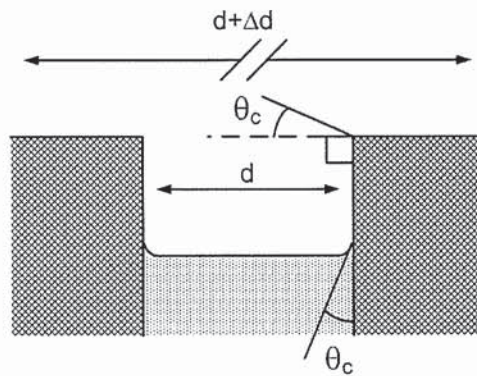
Figure 5.26: step increase in port diameter can be approximated to infinite step size: $\Delta d \approx \infty$

From equation 4.5, and the Young-Laplace equation 5.1, the $\cos \theta_c$ term dictates that introducing a 90^0 offset in the static contact angle has the same effect as making the material hydrophobic, halting the increase in area at the liquid-solid interface, A_{ls}, through reversing the direction of the pressure created across the

meniscus.

The introduction of an abrupt enlargement in the channel forces A_{lv} to increase more than A_{sl} for unit volume change resulting in a net negative pressure that halts the progress of the fluid.

The net result of these factors is a pressure difference across the capillary, and a subsequent fluid flow that is in turn retarded by viscous friction effects, as expressed by the previously introduced Hagen-Poiseuille equation 5.6.

5.4.3   Entrance Effects

If a laminar flow enters a pipe or orifice where it encounters a sudden change in flow boundaries it undergoes a change in profile. After such an event a certain distance of unimpeded flow is required before the laminar profile is restored, known as the entrance or development length. The development length for predominantly laminar flows can be estimated through the equation

$$L_d \approx \frac{d_h}{16} R_e \tag{5.32}$$

where L_d is the development length (m), d_h is the hydraulic diameter of the pipe or channel (m), and R_e is the Reynolds number of the flow. The familiar Reynolds number equation can be written as (equation 5.33)

$$R_e = \frac{\rho L \bar{u}}{\mu} \tag{5.33}$$

where ρ is the density (kg/m^3) and μ is the viscosity of the fluid media (kg/ms), $\bar{u}$ is the mean flow velocity (m/s) in a channel of characteristic length L (m). Substituting equation 5.32 into 5.33 gives an expression for development length based on flow velocity.

$$L_d \approx \frac{d_h \rho L \bar{u}}{16\mu} \tag{5.34}$$

In MEMS devices and micro-scale channels the diameter d_h tends to be sub-millimetre with low flow velocities $\bar{u}$ thereby returning very short and often negligible development-length effects [98]. Consider a flow entering a channel some 100 μm in length (l) and 25 μm in diameter (d_h) from a larger vessel, rearranging equation 5.34 in terms of $\bar{u}$ and substituting typical fluid property values of ρ and μ for water

$$\bar{u} \approx \frac{L_d 16\mu}{d_h \rho l} \approx \frac{1e^{-6} \times 16 \times 1e^{-3}}{25e^{-6} \times 1000 \times 100e^{-6}} \approx 6.4mm/s \qquad (5.35)$$

Indicating that for a development length of the order of 1% of the total channel length a flow velocity would be required in excess of 6 mm/s. This is supported by previous CFD analysis of the channel model. When considering the test device with a mean flow velocity initially of 6 mm/s at inlet, as the flow approached the linear channels as in the test device there was a clear disruption to the flow, however this disruption spans only 40 μm and stabilises too quickly to be visualised in a CFD flow velocity simulation (figure 5.27).
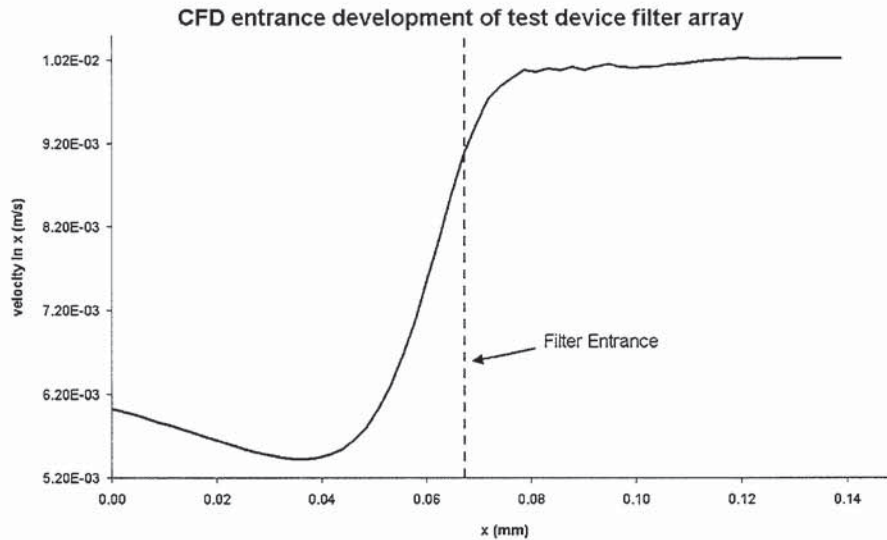
Figure 5.27: mid-stream fluid velocity increases before it enters the filter region of the test device, but settles rapidly after entry into the filter

5.5   Conclusions

Fluid flow within the test device, and subsequently the concept devices, is anticipated to be driven as a consequence of surface effects with an initial high velocity wetting effect, and a more gradual equalisation of forces. Wetting flow can be adequately modelled through a quasi-static approach using a derivation of the Lucas-Washburn equation (eqn. 5.11), modified for a non-circular capillary, a gravity driven head from an elevated reservoir, and boundary conditions that vary with imbibition distance. The calculated wetting velocities suggest that high image capture raes of the order of $85 - 100\ Hz$ will be required for imaging and recording the fluid imbibition.

The geometry of the filtration elements, and the capillaries themselves, have the potential to affect the wetting characteristics of the device through an artificial

190

elevation of the static contact angle. This could however be a potential failure mechanism in the devices if there are any changes or other sources of contact angle elevation within the capillaries themselves. This offsetting of the static contact angle is used to the advantage of the device in the formation of hemispherical droplets at the central reservoir and access wells when the system becomes saturated preventing the liquid from spreading without the need for hydrophobic coatings.

Early design attempts to improve the efficacy of the filtration mechanism at resisting blockage effects may serve to arrest small particles in free-flow conditions through the formation of low velocity regions around the filter elements. It was anticipated that using discrete pillar filter elements would offer greater flow-path flexibility in the event of a larger particle blocking a channel, but CFD models of the fluid flow show that this would create regions comparable in size to the filter elements where velocity would be as much as 90% slower than the bulk fluid. Small particles that became trapped in these stagnant flow regions would be unlikely to escape, and would also be inaccessible to the user of the device.

The complexity of the fluid flow path during the wetting and equalisation phases in the concept devices made direct simulation difficult, and as such no attempts were made to calculate the migration paths, positions or velocities of any fluid-borne particles. Device evaluation therefore relies upon empirical correlation between fluid and particle migrations.

Chapter 6

Device testing

6.1 Overview

The microfluidic devices detailed in the preceding chapters were subject to various levels of scrutiny in order to determine

1. success as a microfluidic device

   a microfabricated device capable of handling and processing fluids

2. success as a passive device

   requiring no external power or pressure sources in order to produce useful work

3. success as a statistical amplifier for non-biological particles

   capable of increasing the chances of finding particular particle types

4. success as a statistical amplifier for biological particles

   capable of increasing the chances of locating particular biological particle types

The final manufacturing batch comprised five complete wafers, each populated with a minimum of six copies of each device type. The wafers were graded according to their etched surface quality, appearance of debris, and the presence of uneven surfaces or damaged structures. The subsequently small number of potentially single-use devices required that the sequence for testing was clearly and carefully defined in order to maximise, where possible, device re-use. For example, the small size of the cells and particles used for testing, and the tortuous complexity of the fluid flow path in some devices offered little chance of complete cleansing and removal of all contaminants from a device. As such efforts were made to ensure that all non-polluting tests were completed before particles were introduced.

6.1.1 Device Identification

As a consequence of the manufacturing process there are fluctuations in quality and structural morphology that can occur between wafers in a batch, and between adjacent devices on a wafer. To help identify or discount variations in experimental data as a consequence of such variations an indexing system was used to record device use and origin. Each wafer was assigned a number indicating manufacture batch, and the wafer in the batch that it was taken from. Further to this a character was used to identify which type of device it was, and finally a suffix number indicating its original location on the wafer. An example of this indexing system is shown in figure 6.1.

6.2 Flow Testing

Herein are detailed the experimental details of how the flows of the devices were measured and compared against the model data in order to verify the source of

A2–2005–1.3 (A)

Device type —
Pre-fix

Channel
Identifier

Wafer Batch —

Device
number

Wafer
number
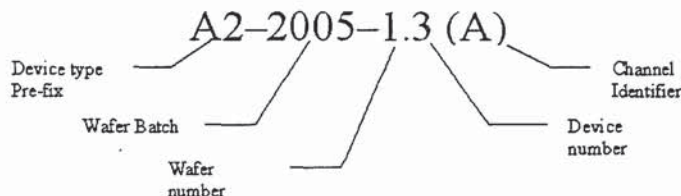
Figure 6.1: the device identifier reference system adopted in order to aid device history, tracking and origins

motive power during each phase of the capillary filling process.

6.2.1 Apparatus

The apparatus for each experiment type are approximately the same, with minor variations on application or processing. A list of fundamental equipment and methods is described here, with only the relevant variations shown in the subsequent experimental sections.

6.2.1.1 Device Loading - Contact Wicking

Device loading and manipulation is facilitated through the use of an electronic Eppendorf micromanipulation system with typically a left-hand mounted manipulator for handling and loading, and the right-hand manipulator employed for aspiration or injection. The micromanipulators, their configuration and positioning with respect to the device are shown in figure 6.2. For loading, an 'instant' delivery of 3 μl of liquid is required, too large a volume to be delivered quickly and precisely using conventional microinjection systems. Instead the micromanipulator was equipped with a 5 μl positive displacement syringe so that the fluid could be dispensed to form a droplet at the tip of the needle which when brought into contact with the device reservoir then promoted wicking of the droplet into

the device, supplying a precise volume of liquid with zero delivery pressure (figure 6.3). Using the programmable interface of the Eppendorf NI2 and NK2 micromanipulators permitted repeatable device loading with minimal variation in syringe positioning.
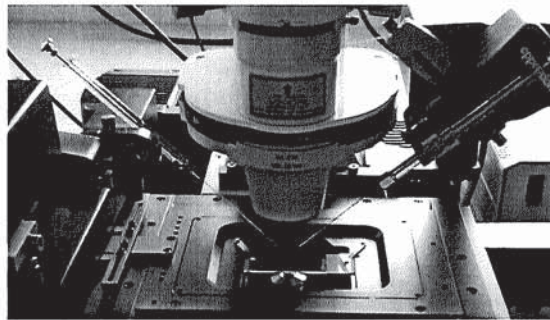
Figure 6.2: the inverted microscope equipped with positive displacement syringes mounted on micromanipulators

In order to avoid positioning errors as a result of device movement during the loading phase a jig was fabricated from glass on a glass microscope slide, thus avoiding impairing the image quality when viewed from below on an inverted microscope (figure 6.4). Due to the small volumes of fluid involved, even under relatively low levels of illumination the devices would be subject to localised evaporation, changing the dynamics of the pressure system involved in providing both capillary imbibition and the equalisation of fluid levels across the device. This process was slowed through applying a hermetic seal to the chip and fluid surfaces after loading by way of an 8 μl droplet of sterile mineral oil.
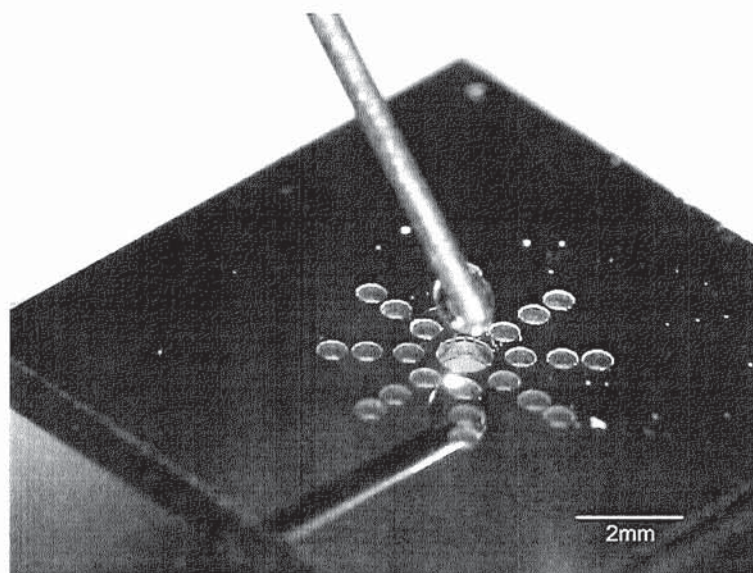
Figure 6.3: applying droplet of fluid to the device by using a syringe mounted on a micromanipulator, and bringing the droplet into contact with the device.

6.2.1.2 Imaging

Loading and imaging was conducted on a Zeiss Axiovert 200M MOT inverted microscope stand using 5×, 10× and 20× objective lenses (Zeiss A-Plan 5×/0.12 NA, Zeiss A-Plan 10×/0.25 NA Ph1, and Zeiss LD Plan-NEOFLUAR 20×/0.4 Ph2). Static images were collected through video stills capture via the right-hand sideport equipped with a JVC KY-F1030U digital camera. Static fluorescense and dynamic image series were obtained using a Carl Zeiss LSM510 Meta confocal microscope attached to the left hand sideport of the inverted microscope stand, permitting digital imaging with multiple channels and scanning whilst loading and aspirating. Images were typically configured to employ one or more fluorescense data channels for the imaging and tracking of fluorescing particles, and a reflective image data channel representing the fluid conduit and any landmark features for location identification. Illumination was provided by laser, the details of which,
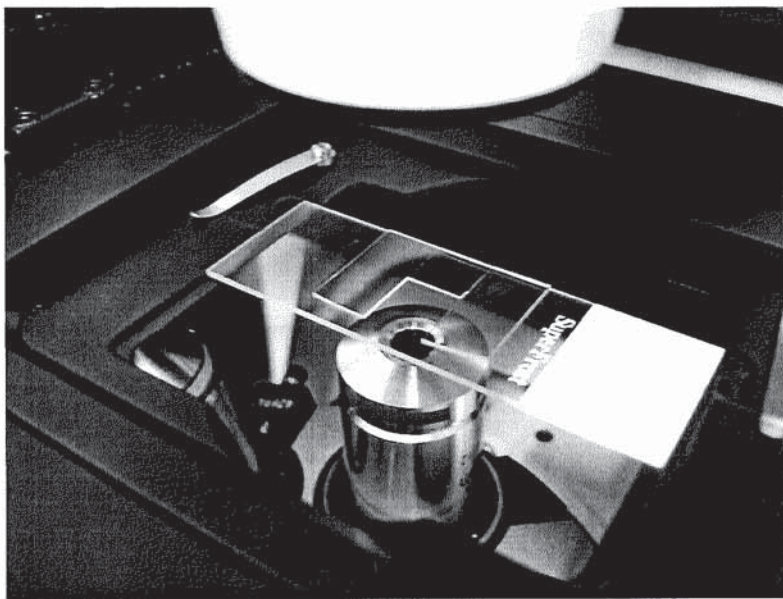
Figure 6.4: a jig was fabricated from glass in order to provide repeatable and secure device positioning on the motorised microscope stage

and those of the imaging filters employed are indicated in each experimental section.

6.3   Evaluating Wetting Velocity

In its most simple configuration the flow test consisted of loading a test device of simple linear capillary configuration with a known volume of liquid and imaging the fluid front at discrete time intervals as it penetrated the various regions within the device. Inter-wafer and intra-wafer variations could be observed and compared with expected values, based on the capillary wetting model (Section 5.2.7), returning baseline data with which to compare flow velocities within device dies.

6.3.1 Objectives

The objectives of this investigation were to determine the wetting velocity of various fluids through a simple microfabricated channel and compare them with velocities predicted by the wetting model.

6.3.2 Experimental Method

A number of test devices, two believed to be representative of each wafer, were installed on the microscope and loaded according to the loading procedure (Section 6.2.1.1) with a volume of between 0.5 and $5\mu l$. Imaging of the device was subject to the scanning speed of the confocal microscope. The speed of a single scan is dependent upon the number of sample points per data line, the data line length and the number of data lines. The scanning parameters were optimised for the highest scanning speed against minimum permissible data capture time in order to return the highest resolution data representative of the fluid flow velocity. Through configuring the microscope to image only the channel at 5x magnification a large potential area was available for imaging, affording more opportunities for recording the meniscus of the fluid. Images were taken based around the central filter region permitting the collection of data up and downstream of these potential peturbations to the flow. The image was divided into three discrete segments, and where possible, data was collected in order to identify the effect of location on the fluid velocity with respect to the filter elements (figure 6.5).

Images were collected reflectively using the confocal microscope with illumination by 543 nm HeNe laser and no optical filters. A scanning plane was selected some 30 μm from the base of the trench with the pinhole adjusted to give a depth of field equivalent to the depth of the channel. This provided a good quality image
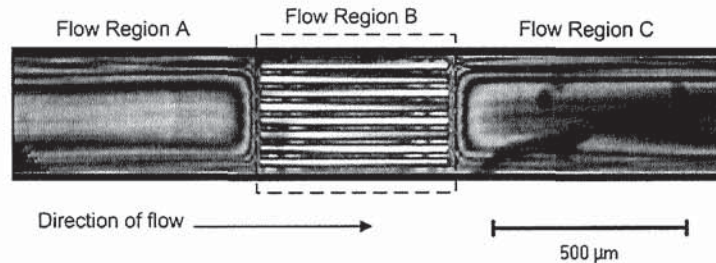
Figure 6.5: each test device channel was imaged as holistically as possible and divided into 'A' upstream of the filters, 'B' within the filters, and 'C' downstream of the filter elements

of the trench and filter structures with a heavy contrast between the wetted and non-wetted regions. Scanlines were aligned horizontally along a length of 512 pixels parallel to the channel walls. This produced an apparent angle in the wetting front (meniscus) providing intra-frame velocity information with a shorter scan interval equivalent to the period of each scanline.

The devices were each loaded a total of 3 times. In the first instance the load consisted of millipore filtered distilled water. The second instance was also distilled water. The purpose of the second fill was to corroborate previous data and to identify any potential effects of the device undergoing a re-wetting cycle. Finally the devices were loaded with a neutral Hepes buffer solution, such as would be used in later biological studies.

A series of timelapse images was collected of each device showing velocity and scale data in terms of inter- and intra-frame capture of the meniscus progress versus time. The sequential line scanning method employed by the confocal microscope permitted flowfront velocity measurement in two ways (figure 6.6).

1. Primarily each frame was completed within a defined frame capture period
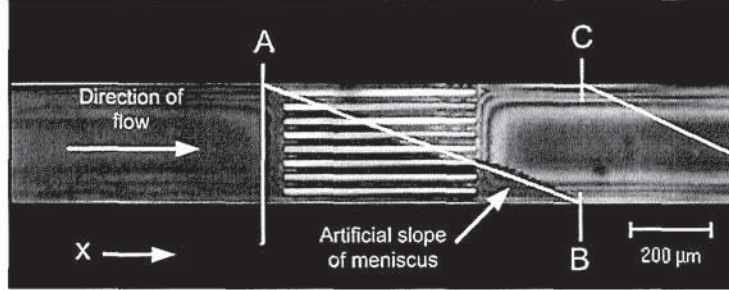
Figure 6.6: still frame of captured meniscus progression, showing linear progression between frames, and intraframe progression indicated by the apparent angle of the meniscus.

Δt_{frame} therefore the position of the flow-front could be imaged, and the distance the fluid had progressed within a single frame period (A-C) could be used to calculate a mean meniscus velocity v_m.

$$v_m = \frac{x_C - x_A}{\Delta t_{frame}} \quad (6.1)$$

2. The line-by-line nature of the frame imaging method provided a clearly defined time period between successive line image captures Δt_{line}. If it is assumed that the meniscus velocity is the same for both walls of the channel, then through taking the meniscus extents (A-B) and summing Δt_{line} across the number of scan lines l_n in the captured region then information could be obtained within a single frame as to the flowfront velocity: manifested by an artificial slope of the fluid meniscus (A-B).

$$v_m = \frac{x_B - x_A}{\sum_1^{l_n} \Delta t_{line}} \quad (6.2)$$

6.3.3   Results

The timelapse images collected in the course of the experiment were manually analysed and annotated in order to determine the meniscus displacement in a

set time period, and hence the wetting velocity of the fluid in the mid-region of the channel. Figure 6.7 shows the collated results of initial wetting velocity for the tested devices, indicating some minor variation in magnitude but no clear evidence of velocity deviations as a result of device wafer origin, or location on the device wafer, or between the two channels on each test die. The data shows a mean meniscus velocity of the order of 32.7 mm/s during initial wetting with a standard deviation of 3.23 mm/s, so fast that velocities could not be distinguished for the different flow regions. No trends suggesting correlation between wafer location, die number or die channel were observed.

Velocities of initial wetting with distilled water by device
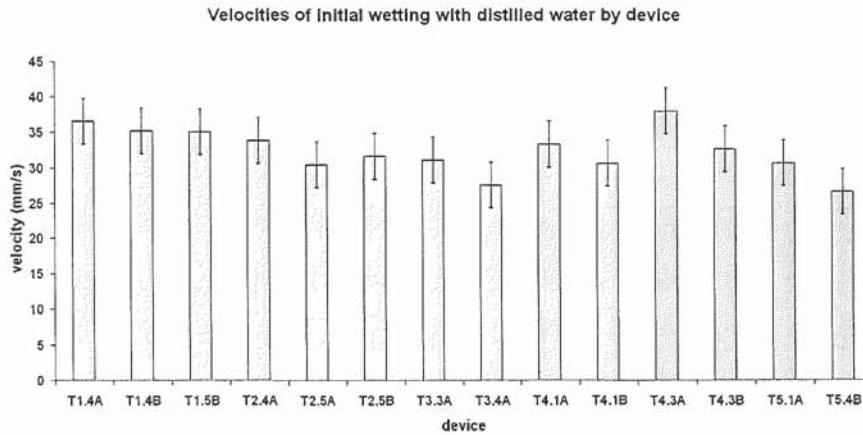
Figure 6.7: the wetting velocities for a range of test devices do not substantially vary between differing wafer batches and location on the wafer.

When the dies were rewetted the most notable observation was the significantly reduced wetting velocity. The devices had been left for approximately 24 hours at room temperature in order to completely dry the internal surfaces without risking changing surface chemistry through thermal heating, cooling, or the application of dehydrating chemicals. The reduced device velocities are shown in figure 6.8, and appeared to show the same apparent variation in velocity between devices,

but the reduced mean velocity makes these fluctuations all the more prominent. A control device was freshly unsealed and tested along with the re-wetted devices and showed the same order of wetting rate as previously observed, eliminating environmental changes as a possible cause of this attentuation.
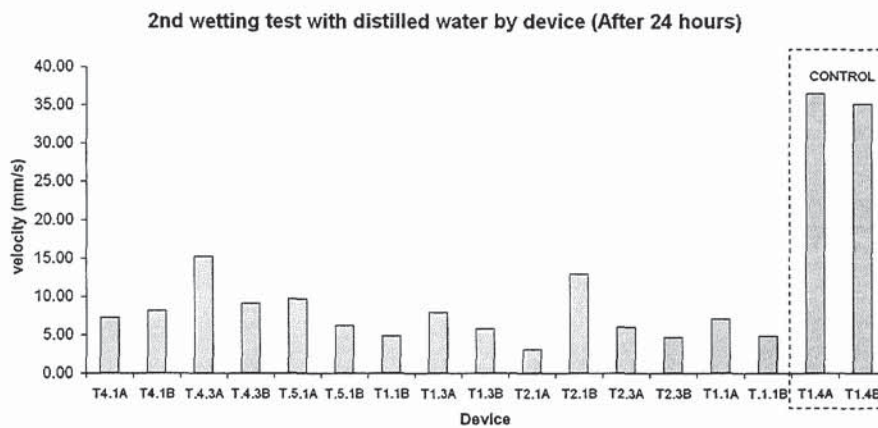
Figure 6.8: drying and re-wetting a number of test devices shows a consistent significant reduction in the mean wetting flow velocity across all devices tested in comparison with the control device

In figure 6.9 it is possible to see the die re-wetting velocities in the different regions of flow, permitted by the reduced imbibition rate of the aged devices, with the majority of devices demonstrating mild fluctuations in wetting flow rates. The results are generally consistent in showing a reduced wetting-front velocity through all regions of the device. In an attempt to determine the source of velocity attenuation in subsequent wetting cycles a number of control dies were used, initially exposed to the air for 24 hours before use, and then allowed to dry prior to re-use over varying time periods. In this way it was possible to identify whether the change in velocity was a consequence of residues left by evaporation or some other effect. These control dies were wetted by the same process and

their mean velocities were recorded and are represented in (figure 6.10).
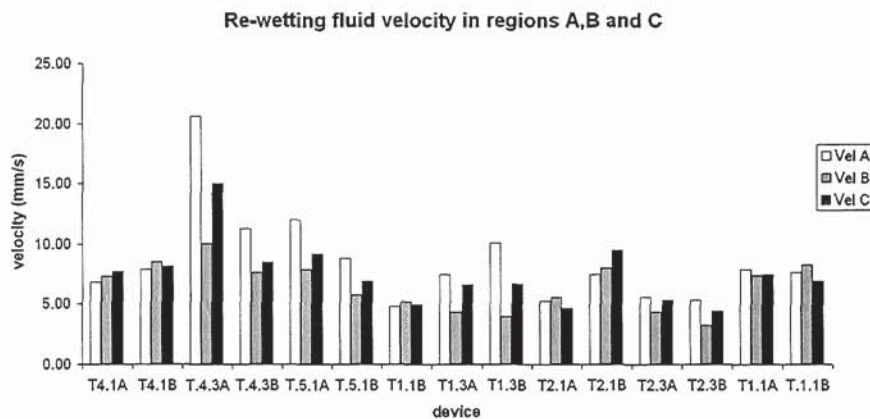
Figure 6.9: the local velocities recorded in regions A, B and C in the rewetted devices

The devices that were unsealed for 24 hours before use suffered the expected wetting attenuation, but devices that were wetted and dried for a short period appeared to exhibit the same velocity as the freshly opened devices. Devices that were wetted and dried for an extended period, of the order of 24 hours, were found to return to the attenuated state as observed in the 'aged' devices. These observations could be interpreted as suggesting that the attenuation is a consequence of dehydration of the device, implying that the sealed devices have some degree of moisture trapped inside.

A further test was conducted in order to verify that this change in wetting velocity was not as a consequence of the number of wetting cycles, two devices were subjected to a third wetting cycle, one of which had been unsealed more than 24 hours prior to testing, the other had been unsealed within a few hours of the test. Both devices however had been given the same 4 hour period in which to

204
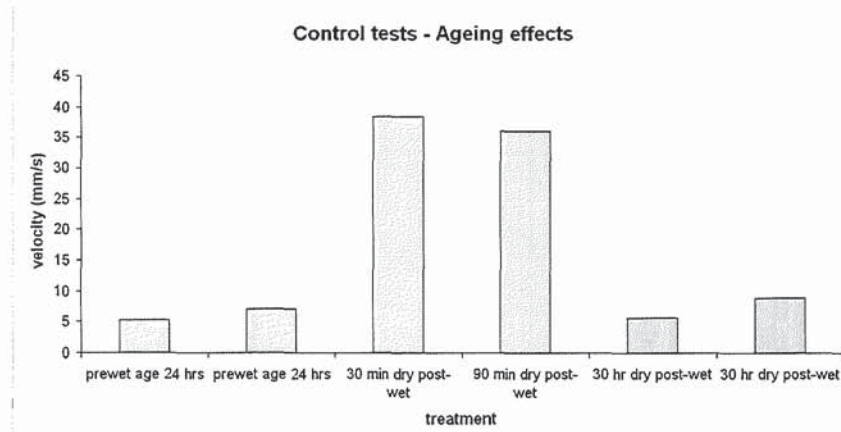
Figure 6.10: preparing devices differently returns differing wetting velocities. Attenuation of wetting flow rate appeared to be a consequence of the period over which the device was exposed to atmosphere.

dry from the preceding wetting cycle. The results of the test are illustrated in figure 6.11 and clearly show a discrepancy between the two dies, with the 'older' devices (exposed in excess of 24 hours) suffering from a diminished re-wetting velocity in comparison with those unsealed and tested within a period of a few hours.

Finally, an evaluation was made of the effect of device loading volume on the capillary wetting velocity. Throughout the experiment a number of devices were subjected to different loading volumes during the second wetting cycle (figure 6.12). The results possibly suggest a linear relationship between loading volume and wetting velocity, particularly in the region upstream from the filter array, but these fluctuations are not beyond those observed during the second wetting test and the dataset is too small to be conclusive proof of a correlation.

Freshly wetted devices after ageing
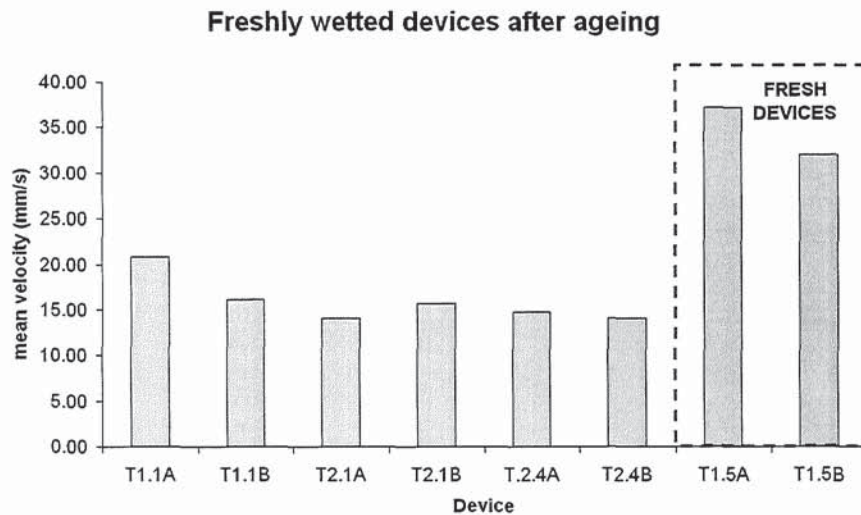
Figure 6.11: comparing the re-wetting velocities of dies following 3 wetting/drying cycles after exposure to air for various periods demonstrates a clear attenuation of the wetting velocity in the 'older' die

Loading volume vs velocity
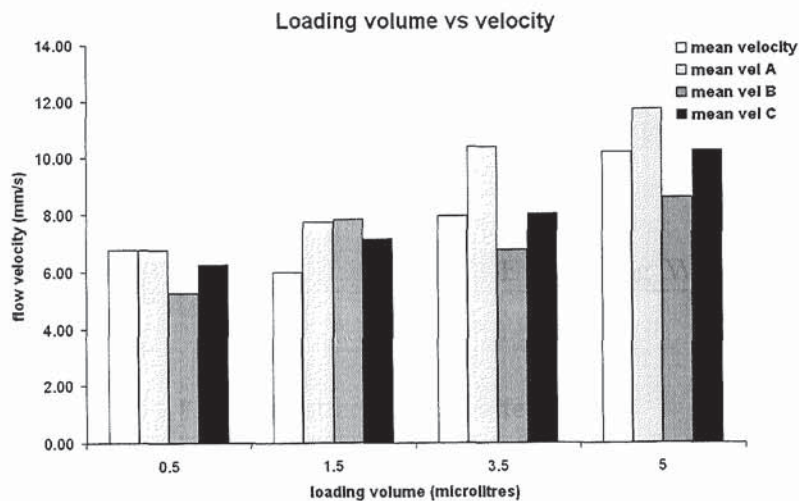
Figure 6.12: loading volume tests results suggest a linear relationship between loading volume and flow velocity, but are inconclusive

206

6.4   Determining Flow Velocity

Finding the fluid velocity was a simple proposition whilst the channel was wetting and the meniscus of the fluid was in sight. This was not so once the fluid had progressed beyond the imaged region of the capillary. The simplest alternative was to image some neutrally buoyant particles that would be swept along the channel with the fluid as it progresses throughout. These particles were required to be large enough to image whilst maximising the visible region of the channel and as such the velocity range that could be studied. In order to achieve this a number of larger channels were fabricated through which particle suspensions could be pumped at known flow rates without the risk of blocking. A small range of channel sizes, and a number of particle sizes, were studied to identify the behaviour of the particles and the conditions under which they could be used to return fluid velocity information.

6.4.1   Objectives

The main objective was to find the nature of the relationship between particle and channel size as they apply to the indirect determination of fluid flow rate through imaging particle movement. Through establishing a relationship between fluid-borne particle velocity and fluid velocity then the pressure across the fluid system and subsequently the source of fluid propagation can be proven. This relationship could then be used to validate the use of larger particles for PIV within microfluidic flows.

6.4.2   Apparatus and Method

A number of surface channels, of rectangular section with varying depths and widths, were fabricated from Accura Si10, an optically transparent photo-setting

resin, using a 3D Systems Viper Si2 Stereolithographer (SLA). The channels were then inverted and bonded to glass microscope slides. The confocal microscope was used to image the channels after bonding in order to determine the cross sectional area in light of the possible dimensional limitations of the SLA (figure 6.13). The inlet of each channel was connected to a 2.5 ml syringe via 2 mm diameter catheter tubing and loaded with a particle suspension. The syringe was mounted on a K.D. Scientific model 210 infusion syringe pump permitting the repeatable and precise control of the fluid flow rate. An arbitrary suspension of fluorescent particles comprising 1 and 10 μm green and 3 μm red micro-spheres was prepared in distilled water and mixed in a vortex mixer for 10 minutes in order to ensure a homogeneous suspension.
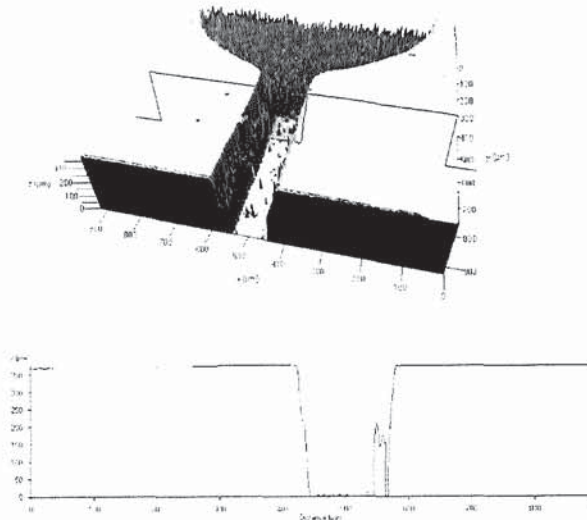
Figure 6.13: image of a channel section taken with a confocal microscope. Optically sectioning the channel offers clear indications of channel depth and width.

The suspension was loaded into the syringe and the channel was primed before

loading into the pump. The channel was mounted on the confocal invert microscope and the focal plane aligned to image the central region of the channel, thus minimising the appearance of boundary effects, whilst the fluid was pumped through at constant flow rates ranging from 0.01 - 0.04 ml/min. The red particles were excited with a 543 nm HeNe laser and the image data was filtered using a 560 nm long-pass filter and collected using a spectral photomultiplier (meta-detector), the green particles were stimulated with a 477 nm Argon laser using a 505-530 nm band-pass filter stimulating a standard photomultiplier, and a transmission image was obtained with a transmission photomultiplier. The strong emission of the green particles permitted the partial closure of the pinhole in order to select only light from a shallow field of view, however the lower emission of the 3 μm red particles and longer beam path of the meta channel required a wider pinhole and thus was marginally less selective over the depth of the viewing field. The red channel meta pinhole was adjusted to 83 μm or 0.95 Airy units (equivalent to 1.1 μm field depth), and the green channel pinhole was adjusted to 63 μm or 0.98 Airy units (equivalent to 0.8 μm field depth). Time lapse images were captured and analysed in order to determine the distance traversed by the discrete particles within known time periods returning inter-frame velocity data. The artificial angle of the meniscus also provided intra-frame velocity.

6.4.3   Results

Through the application of the above process it was possible to derive an approximate correlation between the velocity of the fluid within the channel and that of the particles moving in suspension. The combined data is presented in figure 6.14. Plotting the observed particle velocities against the known fluid velocity it can be seen that at lower velocities the data points are closely aligned and describe an approximately linear relationship. As the fluid velocity is increased there is

an apparent spreading of the data points either side of this line which increases commensurately with the fluid velocity.
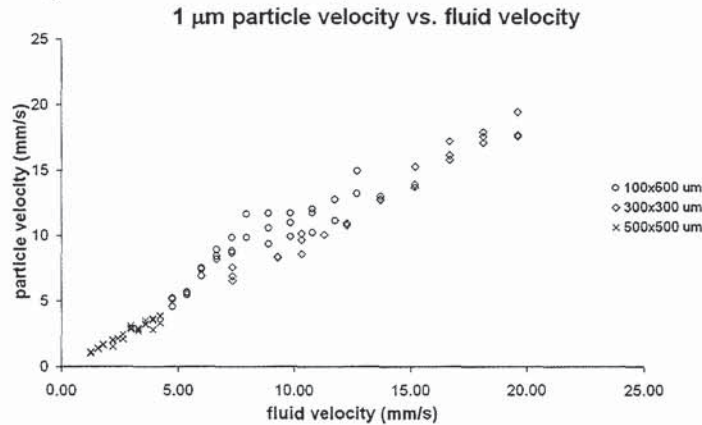
Figure 6.14: 1 μm microsphere particle velocity distribution against fluid velocity for a range of channel sizes showing a positive linear correlation.

Considering the data from an individual channel (figure 6.15) illustrates that the spread of these velocities is not reflected in each dataset, but rather an effect of differing channels. Since the linear velocity of the fluid is a function of the ratio of volumetric flow rate to the cross sectional area of the channel it is inherent that the smaller channels will exhibit higher fluid velocities than the llarger channels at the same flow rate. Similarly, the smaller channels will have less spatial separation between the theoretical maximum fluid velocity, which lies in the centre of the channel for laminar flows, and the channel boundaries. As such boundary effects will become more prominent in the observed flows of smaller channels, with a greater range of like particle velocities visible within the imaged region.

With this consideration it may be said that there is an approximately linear relationship between the fluid and particle velocities in the range of 1-3 μm and as such the velocities of these particle may be used as an indication of approximate

fluid velocity in micro-channels. Smaller channels should be subjected to greater scrutiny in order to effectively identify velocity maxima so as to minimise the chance of misidentifying the fluid velocity as a result of boundary effects.

Mixed particle velocity in 350x85 μm channel
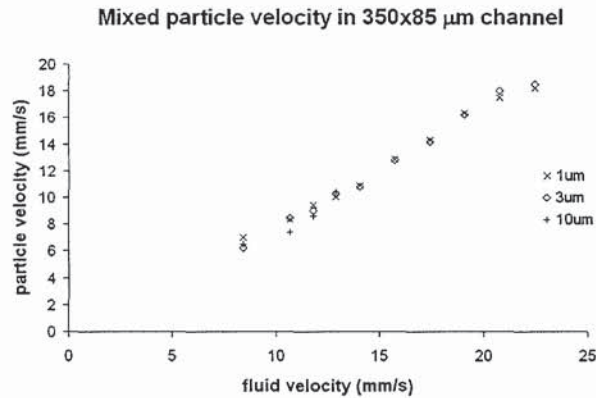
Figure 6.15: mixed particle velocity distributions within a single channel. All particle sizes appear to show a clear linear relationship.

6.5 Particle Effects

Through observing the particle velocities throughout the filling of the test die from empty to saturation it is possible to approximate the fluid velocity bringing about this particle motion, facilitated by an understanding of the effect of fluid velocity on particle velocity. Comparing the actual velocity throughout the filling of the device will aid the determination of the source of fluid power at each stage in the filling process.

6.5.1 Characterising Fluid Flow in the Model Capillary

A test die, comprising two discrete and identical channels some 500x60 μm in cross section and 5 mm in length, was loaded with 3.5 μl of distilled water containing

an arbitrary suspension of fluorescent microspheres of 1 and 3 μm diameter. A series of discrete image captures were taken of the particles at intervals of 11 ms as they progressed through the channels in order to generate a transient velocity profile. The time-lapse images were interrogated and the progression of a small sample of particles was measured within each time period in order to return the velocity estimates. Where possible, particle velocity data was collected upstream, within, and downstream of the filter array: these flows were labelled A, B and C respectively (figure 6.16).
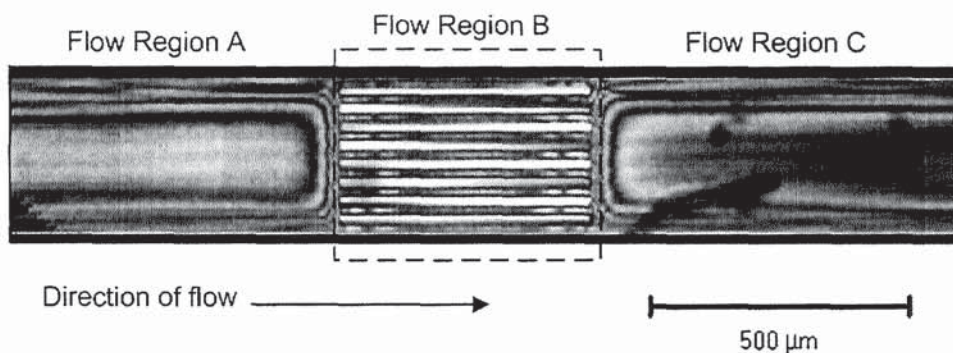
Figure 6.16: particle velocity data was collected within three discrete regions (A) upstream, (B) within filters, and (C) downstream of the filter array

The 1 μm microspheres were pigmented with a green fluorescein stain which was stimulated with a 477 nm Argon laser and the emitted radiation was filtered with a 505-530 nm band-pass filter-set. The 3 μm particles were stained with a red fluorescing rhodamine stain, stimulated with a 543 nm HeNe laser and the emission filtered with a 560-615 nm band-pass filter. An additional reflective image was obtained from the 543 nm reflected light which was used for returning reference landmark information.

6.5.2 Results

The wetting model of the capillary predicts a sharp initial increase in fluid velocity which rapidly diminishes in asymptotic fashion as a result of hydrodynamic drag and terminates abruptly as the channel wetting is completed. This was in agreement with the data recorded in the experiment where particles were seen to follow the wetting of the channel rapidly and then quickly slow when wetting is completed within approximately $0.1s$. Figure 6.17 shows how the fluid wets quickly throughout the channel and does not arrest completely when it reaches the outlet, but rather continues to flow steadily at approximately 6-8 mm/s until it begins an asymptotic decline with time.

Repeating the experiment for a shorter period but at a higher temporal resolution illustrates a clear distinction between flow region velocities indicating that continued particle motion is due to continued fluid fluid flow (figure 6.18). This serves as evidence that a secondary equalisation flow phase is influential post-wetting and although not as dramatic as the initial wetting velocities, it can still be harnessed to do useful work. Particle migration was observed to fall to negligible levels after a period of some 25 seconds, with particles moving at speeds of below 80 $\mu m/s$. It should be noted that the first data point does not occur at position $x = 0$, but after an initial position offset of $x_0 = 200$ μm.

6.6 Evaluating Flow Mechanism

After proving the capillary driven wetting and flow mechanism it remained to observe what effects promoted flow completion, and evaluate which forces encouraged flow to continue once the wetting phase was finished. The period in which the fluid advances and completes proved too small to image whilst collat-

Particle velocities within test channel
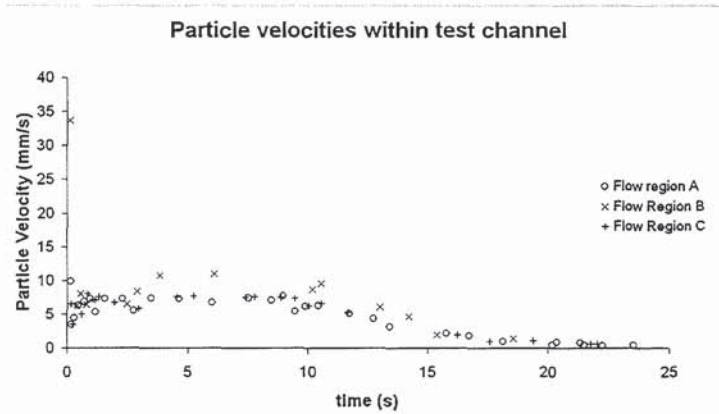
Figure 6.17: particle velocity transients within a test device for flow regions 'A', 'B' and 'C', demonstrate a high initial velocity, with gradual decay after approximately 10 s.

Particle velocity vs. time for 3 regions of flow
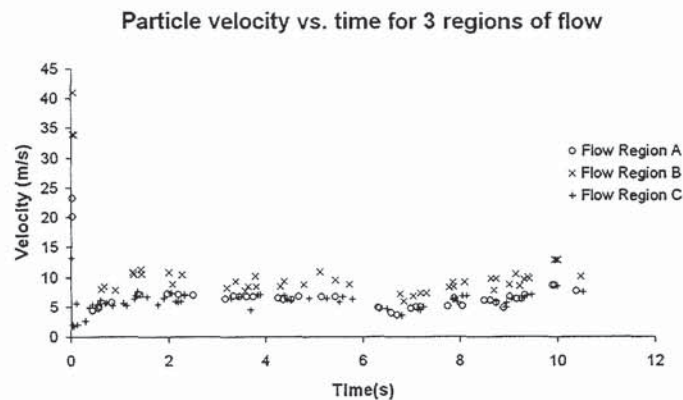
Figure 6.18: velocity data from particles flowing within the first 10 seconds of the wetting a test device. There is clear agreement between up and downstream velocities (regions 'A' and 'C') whilst mid-filter particles exhibit higher velocities indicative of particle movement due to fluid flow.

ing any meaningful data, and rather than attempt to retard the flow artificially and bias the results it was simplest to image the fluid retreating. Assuming that there is negligible hysteresis in the fluid forces during the loading-unloading cycle then through loading devices with distilled water and allowing the fluid to slowly evaporate naturally then dominant fluid forces could be discerned.

6.6.1 Hypothesis

Providing the assumption that equalisation is a result of the predominant surface tension effects then when evaporated the fluid would preferentially remain in the smaller access wells and would appear to be removed from the inlet reservoir alone. As a consequence the fluid level in the central reservoir would decrease whilst being retained in the access wells.

Conversely, if at any stage the dominant effect is that of hydrostatic pressure head and a pressure differential induced across separate but linked free surfaces then the fluid levels in all wells would appear to fall at the same rate. The access wells combined to provide a considerable surface area in comparison with that of the central reservoir, whereas the central reservoir comprised a larger single volume of fluid providing a larger thermal reservoir. Whichever of the two was subject to the largest mechanism of evaporation is inconsequential as the hypothesis would still hold: for hydrostatically dominant effects any difference in fluid level as a consequence of evaporation would result in a net fluid flow from one fluid source to another in order to equalise fluid levels.

6.6.2 Method

The post-wetting flow mechanism was observed through loading a device with $2 \ \mu l$ of distilled water by the standard method, allowing the water to saturate

and then partially evaporate. The partial evaporation acted to gradually remove fluid from the device, an effect which would reveal the dominant equalisation mechanism by influencing the direction of fluid flow.

These principles were explored in three device formats (figure 6.19), all with a common large central reservoir, one type with wells that increase in diameter with increasing radial position (i), another with wells that decrease in size with increasing radial position (ii), and the final type with a constant or uniform well diameter (iii). Through applying a volume of fluid to these devices and imaging a line crossing a line of wells over time it is possible to visualise the order in which the wells are emptied, and the rate at which it occurs.

(i) E concept   (ii) A concept

(iii) B concept

⊢ 2 mm ⊣
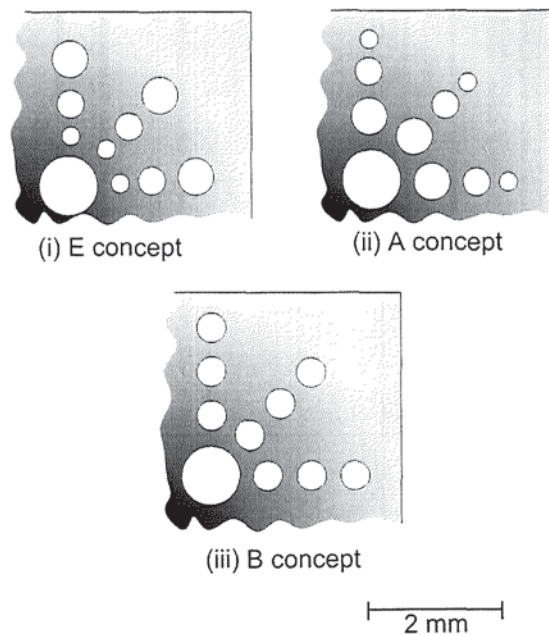
Figure 6.19: dies were designed with access wells of (i) increasing diameter, (ii) reducing diameter, and (iii) constant diameter in order to assess wetting dynamics

The devices were loaded on the inverted microscope and imaged using the LSM 510 Meta confocal scanning module. A 5x objective lens was used to produce an image of a complete device channel at a time, and the device was illuminated using a 543 nm HeNE laser with no filter set. The focal plane was aligned to the glass/liquid interface within the device, this exploited the differences in refractive index with the glass-air interface reflecting the incident light, whilst the glass-liquid interface refracted the light away from the objective. A line-scan image was taken of the centre of the channel crossing all wells, and the line images were composited together in order to produce an 'x' versus 't' plot. Atmospheric conditions at the time of the experiment were recorded as being 26°C with an estimated RH of between 40 and 50%.

Figure 6.20 shows the collected data from three devices representative of the differing well morphologies. In the majority of cases the largest central reservoir is the first to be emptied, followed by the remaining wells in order of descending diameter. In addition, an extended dataset taken of an 'E' type device, shows a region of internal reflection induced by the formation and collapse of the fluid meniscus as it passed the level of the silicon substrate (figure 6.21). During this region it is worth noting that the same effect is observed across the wells and the reservoir at the same time, suggesting that the governing force at this time is gravimetric in nature.

6.6.3 Results

The results of the test support the idea that the surface forces were as dominant in the post wetting flow as they were in the wetting process, concurring with the hypothesis. Initial evaporation yielded a net reduction in the level of the fluid meniscii until a minimum energy condition was subtended. After this, the fluid
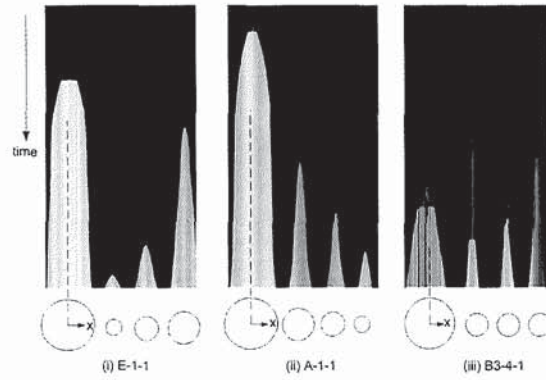
Figure 6.20: intensity versus time plots for a line scan of each concept type. (i) and (ii) show wells emptying in order of descending well diameter, (iii) shows emptying in random pattern with a smaller delay between adjacent wells.
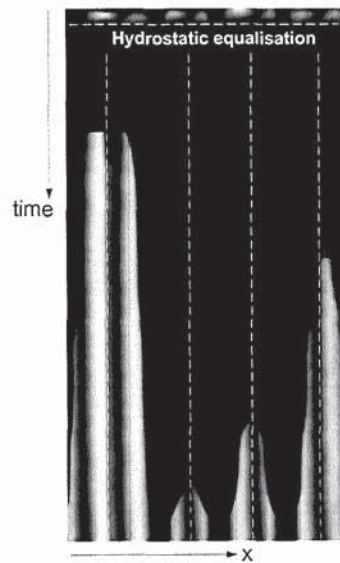
Figure 6.21: E-1-1 device capture shows hydrostatic equalisation at the silicon surface, followed by surface force control over fluid loss within wells

218

level within the central reservoir lowered quickly with evaporation, whilst the access well levels were unaffected till the central reservoir was largely emptied. This indicates that the meniscii of the outlet access wells, being of smaller radius than the inlet reservoir, retained their fluid level against any gravity driven influences. Further to this, the size of the access well had an impact on its ability to retain the fluid against hydrostatic pressure gradients, with the smaller well diameters being more effective at retaining fluid.

This information can be used in tailoring device designs to different applications, with different working fluids and different operating principles. Through controlling the size of voids or wells fluid devices could have their evaporative or wetting characteristics enhanced in order to promote flow, or preferential loss of fluid, or to delay evaporation in a principal site through incorporating sacrificial sites.

6.7   Particle Image Processing

In order to monitor distributions and ultimately measure how effective the devices were by considering the terminal locations of the tested particles it was necessary to conduct a series of constituent particle counts. If attempts were to be made to test with populations comparable to those of testis biopsies it would be impractical and inefficient to count the imaged particles manually: a means of automating this was required. The false colour capabilities of the confocal imaging process would prove to aid automation of this process considerably.

The captured images were captured with 2 or more data channels, with a data channel representing the particles of interest and another imaging the devices themselves and placing the particle data into context. The particles were false coloured according to their stain, for example fluorescein emission was false

coloured green, and the rhodamine fluorescing particles were false coloured red. The context image data was selected as white on black. The data was combined into a full colour image and exported from the Carl Zeiss AIM software LSM data format in tagged image file (tif) format.

6.7.1 Particle Counting

The image data was imported into MATLAB and separated into its constituent red, green and blue colour channels. As there was no blue false colour it was assumed that the blue data would be representative of the non-fluorescing image, and by subtracting the blue data from the captured red and green channels a cleaner image solely consisting the fluorescing particles would result. The particle image data was then passed through a filter in order to obtain monochromatic image data which could be analysed by image processing tools.

The particle image data was processed using the MATLAB image processing toolbox to identify particle pixel areas and centroid locations. The simplest means of determining the number of particles within the image was to sum the total area of illuminated pixels and divide by the mean particle area. This operates on the assumption that all particles are in the viewing field, and that only whole particles are visible: there are no partial images or fragments. This method offered no means of returning particle location for distribution analysis, instead requiring that devices were imaged in discrete segments.

Alternatively the centroid data could be used to count the number of unique particle centroid positions. This operates on the same assumption that there are no fragments of particles visible, but also makes the further assumption that no particles are immediately adjacent to one another in the image.

Ultimately a compromise between both methods was employed in the development of a robust counting algorithm, capable of determining distributions across a tilescan image of an entire device.

6.7.1.1   Counting Algorithm

The images were analysed in order to return centroid position and the pixel area surrounding each of the identified centroids. Of the identified centroids a mean area was taken, and all regions smaller than 25% of that mean were ignored as being fractious reflections, out of focus information, or noise. The remaining areas were arranged into an order of decreasing size, and a region was selected that could be considered to be representative of the majority of the cell pixel areas. Since the regions were in some instances comprised of more than one particle image, a simple average area could not be considered representative (figure 6.22).
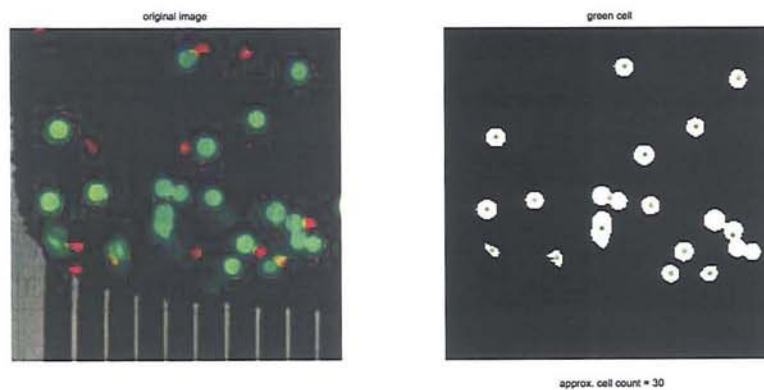
Figure 6.22: some image areas were comprised of more than one particle, only a single area and centroid was returned for a multiple of particles

However, based upon the assumption that the majority of particle images would be of single particles, and that following the previous small image filtration process, these images would comprise the smaller of the detected areas, it was considered reasonable to arbitrarily select one of these images as being representative of a single particle image area. The optimal pixel area was chosen, based on empirical evaluation, to be within the lowest third of area sizes (figure 6.23). Example output of the processing algorithm is presented in figure 6.24.
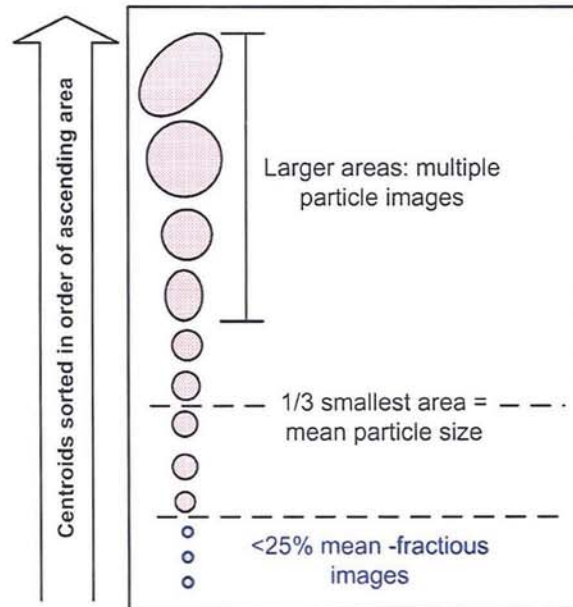
Figure 6.23: the counting algorithm sorts individual particle images by pixel areas, discards the images of fragments and selects an arbitrary threshold as the mean size of a single particle.

Colour Image (RGB)   Red Image Channel   Cleaned Red Image

Green Image Channel   Cleaned Green Image
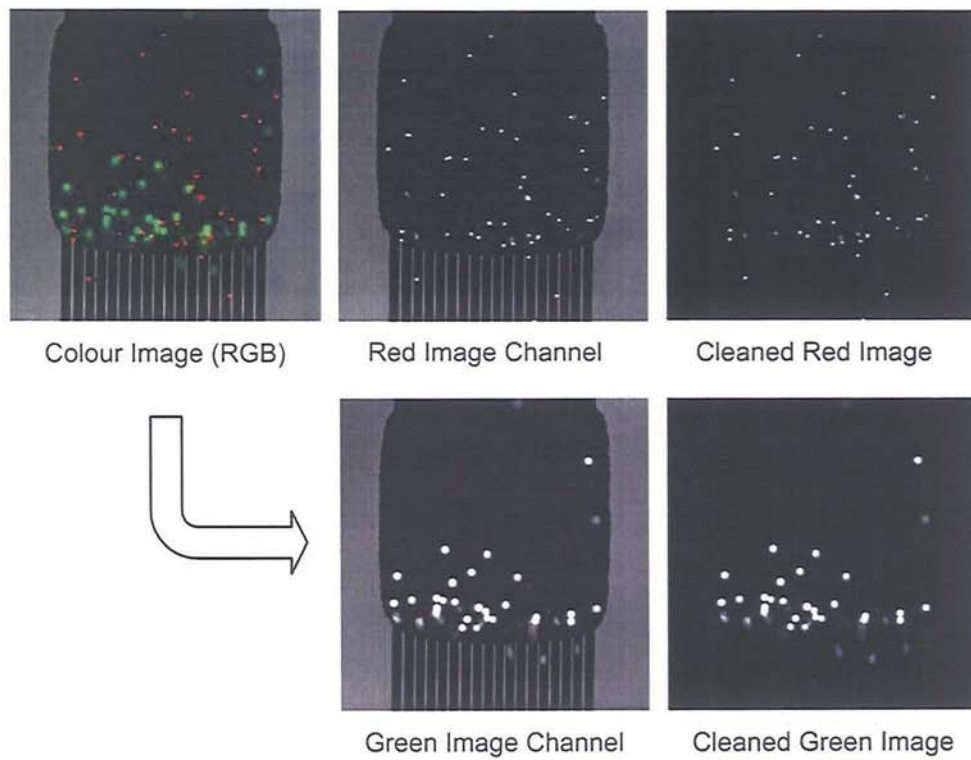
Figure 6.24: colour data from the images were separated, cleaned and devolved to binary bitmaps for area counting

6.7.1.2   Testing the Algorithm

The counting algorithm was refined and evaluated with a number of sample images taken from tested devices, by way of direct comparison with manual and electronic counts. The results of this comparison are shown in figure 6.25 for $3\ \mu m$ red particles, and figure 6.26 for $10\ \mu m$ green particles. The output of the algorithm was found to be in good agreement with the manually counted populations, with average errors of the order of $\pm 5\%$ and $\pm 3.5\%$ for red and green population estimations respectively.
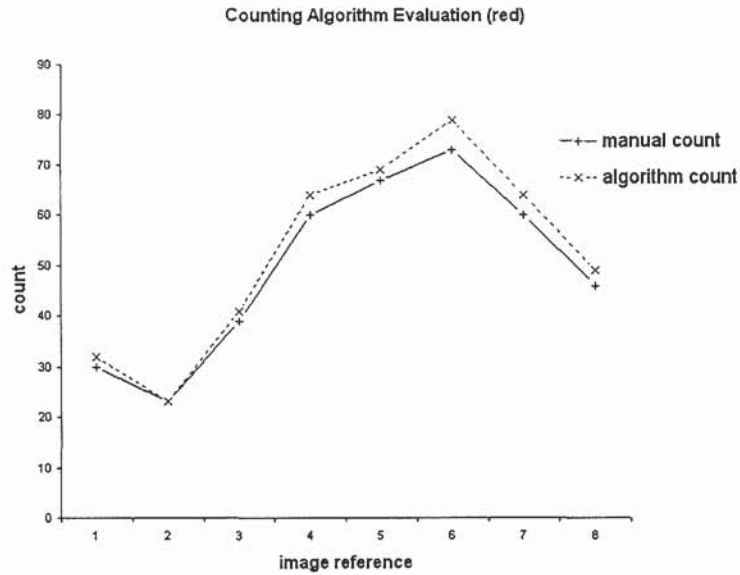
Figure 6.25: evaluating the red particle counting algorithm indicates a strong agreement between automated and manual particle counts for a range of sample images
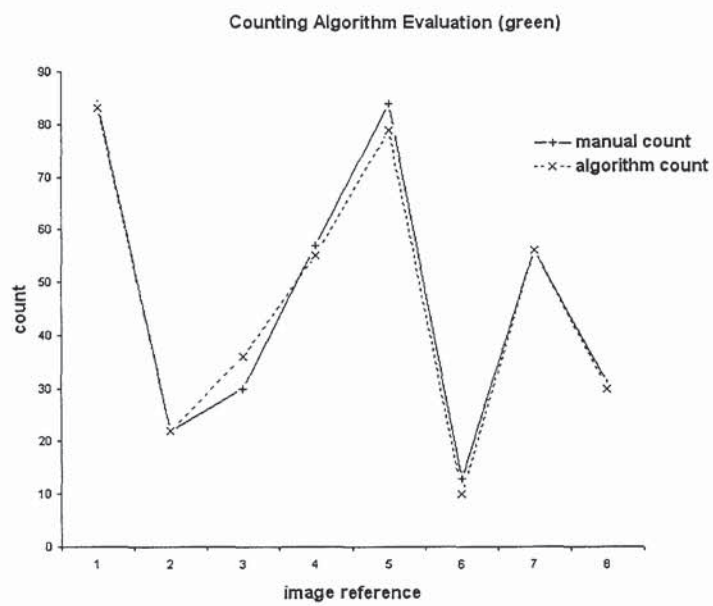
Figure 6.26: evaluating the green particle counting algorithm indicates a strong agreement between automated and manual particle counts for a range of sample images

6.7.1.3   Beyond the Count

The optics of the microscope limit the size of the imaging region, however the motorised scanning stage of the Axiovert 200M MOT permitted the generation of composite tiled images, enabling the entire device to be imaged. As the majority of devices have rotational symmetry about the central reservoir, and the counting algorithm was capable of excluding extraneous image data and locating the position of particles and particle accumulations a method was required that would compress the data into a readily analysed and comparable form. This was achieved by transforming the data from the captured cartesian coordinate format into a polar co-ordinate system centred on the middle of the loading reservoir (figure 6.27).
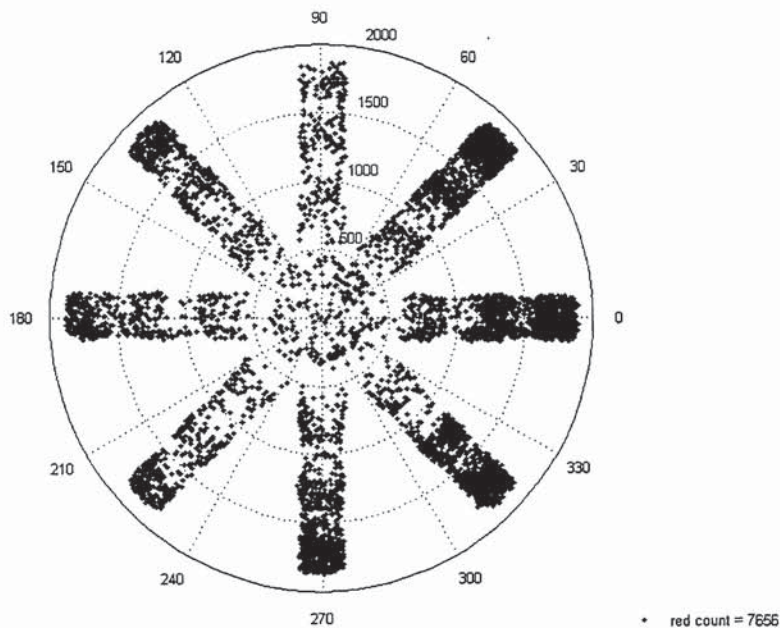
Figure 6.27: converting the data from a cartesian coordinate system to polar coordinates centred on the loading reservoir to reveal a centroid density plot

After translation of the data population the location was described by a reference angle (θ) and a radial distance (r). For the most part particle migration was only of interest in terms of the radial distance and so all angle data could be disregarded and the data compressed by summing the device particle population by unit radius. The data could then be presented graphically. Finally the data was normalised between successive experiments by expressing the population data in terms of the percentage of visible particles per unit radius (figure 6.28).

Percentage particle distribution by radius for B3-4-6 device
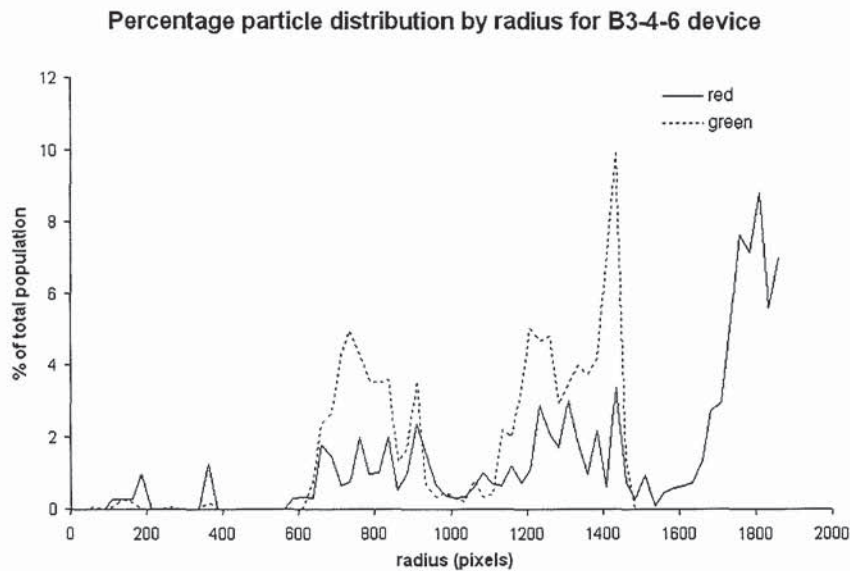
Figure 6.28: graphically displaying the percentage population distribution for simple comparison between devices

6.7.1.4   3D distributions

The 3-dimensional time-lapse imaging of a device access well following loading with 3 μm particles demonstrated that the majority of particles within the well settle over a period of minutes to the bottom of the well (figure 6.29). Population

gradients were taken across the wafer both immediately after loading, and at some time after loading was completed. This indicated that the actual population can be as much as 200% of the initial count, but the particle population gradient is consistent when cells are both in suspension and after settling (figure 6.30).

(i) plan image of well   (i) side projection image of well
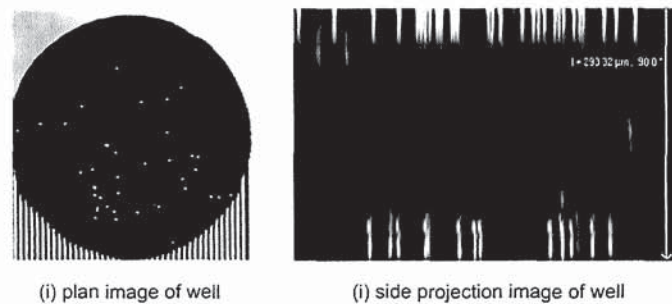
Figure 6.29: (i) plan image and (ii) a side-projection of a final stage collection well illustrates how the majority of cells occupy the lower part of the chamber, that nearest to the glass and filtration chambers.

A random selection of 3-dimensional scans of a number of devices and samples tested with a mixture of particle distributions returned an observation that the majority of suspended particles will occupy the region closest to the glass within a few minutes of loading when not prevented from doing so by physical obstruction. As such when considering the distribution it was surmised that a representative majority of the population of a well could be observed by scanning only the near-glass region.

6.8   Load/Flush Ratio

When loading a passive device with a particle suspension only the fluid-borne particles that pass through the filtration elements as a consequence of their motion within a bulk fluid flow will undergo separation. That is to say that any particles

Comparing 3 μm particle distribution after settling period
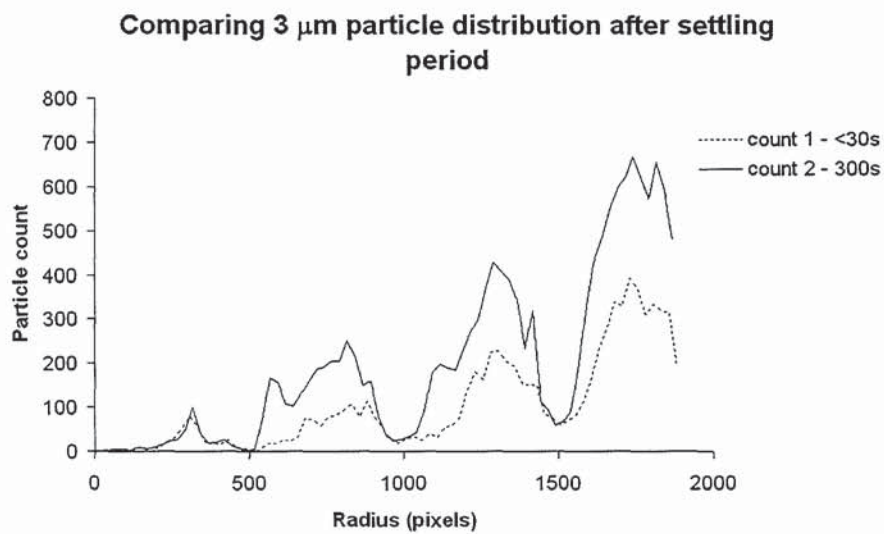
Figure 6.30: comparing the population distribution across a device (count 1) less than 30s after loading and (count 2) after a period of 5 minutes indicate an overall increase in visible particles, but a consistent proportion of the total population of particles across the device

contained within the latter part of the fluid dose will not be induced to flow to the ends of the fine capillaries from the central reservoir unless more fluid is added afterwards, and a bulk flow is induced.

The loading of a device therefore requires a minimum of a two-stage process, an initial loading and wetting cycle and a subsequent flushing cycle to saturate the channels to capacity. Previous work illustrates that correct design can influence selective fluid retention, so that fluid can be discouraged from accumulating in certain regions. In the case of the standard die format employed the larger central reservoir will be drained at the cost of filling the smaller wells. A fortunate consequence of this is that any cells borne into this fluid will also migrate, where possible, into these channels and not accumulate in the central reservoir.

However, once the wells have filled there is no longer a source of bulk fluid flow from the central reservoir. In the event of the end-most well being filled, any added fluid will only flow to fill the central reservoir and other wells that are not filled to capacity. Consider a single channel from a die in 2 dimensional section having been wetted, and filled to capacity with water at 25°, such that the pressures across the meniscii are equal. If additional fluid is added to the central reservoir, instantaneously increasing the local gravimetric head it can be seen that the greatest flow is observed in the first filter region, and flow into the subsequent wells is considerably less (figure 6.31).

It follows that if the end of the channel network, the final access well, is by some mechanism maintained at a lower pressure then flow between this and the central reservoir and any intermediate stages will be much higher (figure 6.32). Nonetheless, any bulk flows will be small in comparison with the initial wetting and saturation phase of flow.
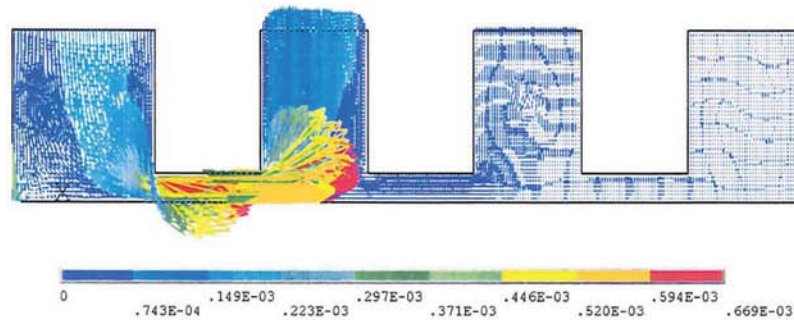
Figure 6.31: adding fluid to the central reservoir after saturation generates the highest flow velocity from the reservoir to the first access well. Other flows are negligible.
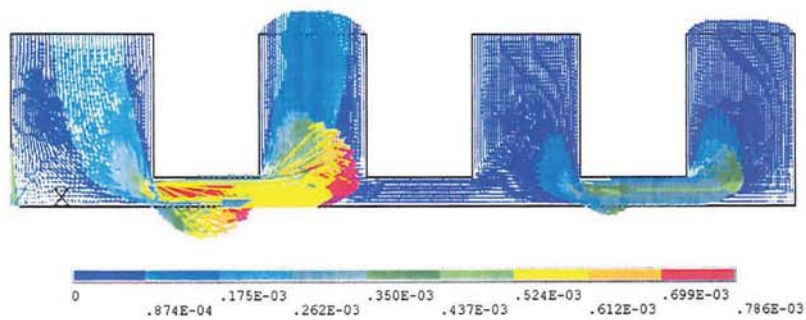
Figure 6.32: maintaining a lower pressure in the end well encourages flow throughout the channel, but flow rates are still low in comparison to wetting flows.

6.8.1 Hypothesis

Therefore filling the device beyond saturation holds little benefit as it applies to particle migration or flushing. As such it follows that for optimum separation, the full volume of fluid, comprising both sample and flushing media, offers little separation advantage if it exceeds the total capacity of the device.

The experiment involved applying a constant volume of 3 μm particle suspension, followed by adding successively increasing volumes of flushing media, in many cases beyond the maximum volumetric capacity of the structure. Limited device numbers meant that it would be inappropriate to use good quality devices for this baseline study. So in order to test the hypothesis an experiment was devised that used poor quality devices of the same configuration. The devices (or dies) used were judged to be of a poor quality as a result of their filter element morphology, having incomplete structures or overetched features, and were suitable for the study as the particles used in the tests were selected to be a size smaller than the finest filter stage.

6.8.2 Method

The 'B3' dies were loaded with a controlled volume of 3 μm red fluorescent particles at an arbitrary concentration in an aqueous suspension using a 1 μl positive displacement syringe mounted on the right-hand micromanipulator of the inverted microscope. Varying volumes of distilled water were subsequently applied to the device using another syringe mounted on the left-hand manipulator, and once all loading was completed the dies were sealed with an 8 μl droplet of sterile mineral oil which was manually aplied using a micropipette. The dies were imaged using the confocal microscope collecting both reflective and rhodamine red data as in previous studies.

The particle distribution across the entire device was measured using an image processing algorithm within MATLAB. The data on the population count was determined per unit radius from the centre of the main reservoir and normalised between images as a percentage of the total visible population. The initial particle suspension load was kept constant at 0.5 μl and the flush volume was increased in 0.5 μl increments up to and beyond saturation.

6.8.3 Results

Collating the data from a number of tests, in which the number of 0.5 μl flush cycles was increased and the subsequent particle distribution was compared, it was apparent that, as anticipated, batches without any flushing media had a consistent homogeneous distribution of particles. Also, it was observed that across all tests the number of particles within the filter regions, although incomplete, exhibited a considerably lower population than the access wells (figure 6.33), perhaps as a consequence of the smaller volumetric capacity of the filter regions.
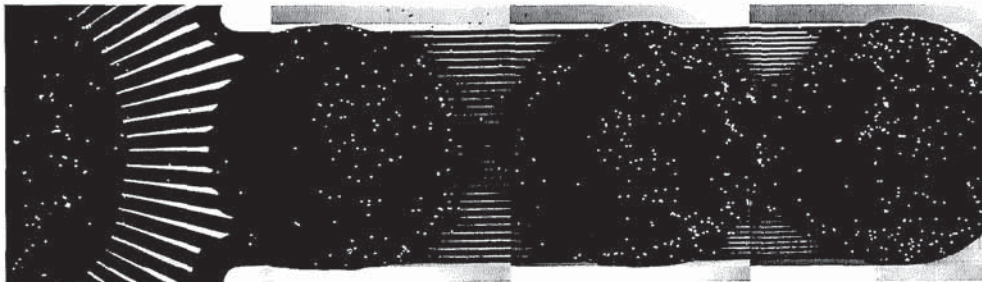
Figure 6.33: particle population (shown in white) in filter regions across all tested 'B3' devices was consistently lower than the population within access wells.

Repeating the test with flush media, and an increasing number of flush loading cycles initially returned a significant improvement over the test without flush

media. This effect, however, was not continued and soon plateaued (fig. 6.34). Comparing the final particle distributions an optimal distribution was observed when there was a 1:1 ratio of loaded suspension to flush media comprising total device capacity. Data suggested a slightly increased degree of migration with higher flush proportions however these increases were negligible when considering the required reduction in volume available for load sample.
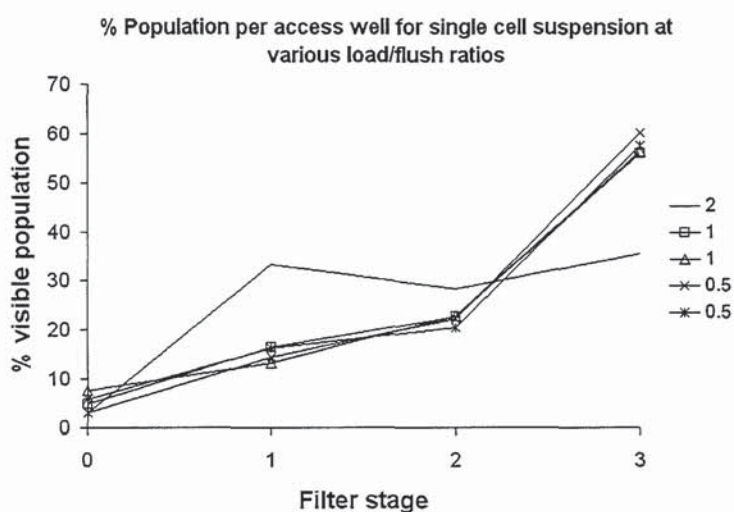
Figure 6.34: improvements in particle migration as a result of increasing the volume of flush media quickly plateaued to negligible levels.

Adding flush beyond the device capacity, following brief partial evaporation cycles, had little effect in improving particle migration. This is a consequence of the fluid in the central well preferentially evaporating, and as such any subsequent fluid additions beyond saturation and evaporation served only to refill the empty central reservoir. It can therefore be surmised that for optimal performance the sample load and flush volume should not exceed the total device capacity in its given configuration.

6.9 Particle Distribution

A working knowledge of the principles involved in flow within the test structures could then be applied to actual devices so that a fair assessment could be made of the filtration efficiency of the devices. Questions important to evaluating the performance of the micro-filter and its use for cell separation include:

- where do particles go: where do they accumulate?

- in what quantities/proportion of the original dose can they be found?

- how do the component particle types impact the migration of other particles?

6.9.1 Baseline

All previous tests had been conducted with arbitrary particle populations and concentrations. With any separation or filtration mechanism there is a limit to the concentration of particulates that can be tolerated before blocking results and there is a detrimental effect on the fluid flow. Attempts were made in order to determine the particle populations at which this would occur in order to firstly, determine whether the device could adequately handle the suspensions as found in a testis biopsy, and secondly to provide a baseline on which separation comparisons could be made.

Particle distribution testing was to be undertaken with three representative particle sizes, as identified in section 3.1, and summarised in table 6.1. Starting with the largest particles, and those most likely to cause blocking within the channels, the maximum population of 23 μm ragweed pollen was estimated. Two estimation methods were immediately apparent:

- blocking based on volumetric channel capacity

- and blocking based on filter channel capacity

It was surmised that through performing approximate calculations on each method then a suitable conservative estimate could be reached. Previous tests indicated that the devices with the best etch characteristics and subsequent separation performance were the 'B3' type devices, so all initial tests would use these as their subject.

filter stage	particle diameter	particle type
1	$\approx 23\ \mu m$	ragweed pollen
2	$\approx 10\ \mu m$	microsphere (fluorescein)
3	$\approx 3\ \mu m$	microsphere (rhodamine)

Table 6.1: particles used for distribution testing

Considering the 'B3' device, the channel dimensions were some 300 μm wide and etched to a nominal depth of 60 μm, yielding an approximate cross sectional area of 18,000 μm^2. Assuming the ragweed pollen grains to be approximately spherical with a nominal diameter of 23 μm, then whatever their orientation they would offer an obstruction of an area of 415 μm^2 to the direction of flow. Thus implying an individual channel would become blocked at a population of 43.3 particles, extending to some 347 particles in order to block all 8 capillary branches.

Now if the filter channel capacities are considered, there are 14 individual large cell channels with a nominal clearance of 20 μm. Etched to a depth of 60 μm each filter channel can accomodate some 2.6 particles before blocking. Considering all 8 channels the blocking population can therefore be approximated to:

$$\frac{60}{23} \times 14 \times 8 = 292 \tag{6.3}$$

The more conservative of these estimates is the filter channel capacity, assuming that all particles are arrested at the initial filter array. If a number of particles were able to progress onto the next stage then this estimate would of course be erroneous and the ultimate capacity would be higher.

6.9.2 Nominal Populations

These estimation methods were then applied to the smaller particle sizes, and the results for each method are presented in table 6.2 and table 6.3 respectively.

Particle Diameter	channel capacity	device capacity
23 μm	43.3	$\approx$ 347
10 μm	229	$\approx$ 1833
3 μm	2546	$\approx$ 20370

Table 6.2: estimated capacities of 'B3' device according to channel cross section

Particle diameter	channel number	channel capacity	total
23 μm	14	2.61	$\approx$ 292
10 μm	30	6	$\approx$ 1440
3 μm	45	20	$\approx$ 7200

Table 6.3: estimated capacities of 'B3' device according to filter channel size

The conceptual limitations of the 'B3' device were estimated, based on the channel sizes, the number of filter channels for each stage and the approximate capacity. The dimensions of the channels fluctuate according to the quality of the etch, with overetched features permitting passage to over-sized particles. The particle sizes themselves are also subject to mild variation. Assuming variations in both channel and particle size to be small in comparison with the overall channel sizes these estimates serve to assist in the generation of an upper limit of cell population

for use within a 'B3' device. From these estimates it is clear to see that the device is unlikely to block as a consequence of the 3 μm particles until concentrations in the 1-2 μl loading volume approach extremely high levels. Blocking is more likely to occur as a result of the 23 μm particles, the operational range of which should not exceed the order of 300-500 particles per μl.

6.9.3 Separating Single Cell Types

The initial stage from which cell separation efficacy could be evaluated was that of monitoring the behaviour of the particles from a suspension comprising a single cell size. This would then serve to demonstrate the maximum separation that could be achieved as any flows would be unhindered by larger particles or groups of larger particles. This test would also address the initial concern of the star-shaped device layout, that of particles flowing in suspension failing to reach the end of the filter branches.

An additional benefit from this process was to be the identification of the more effective device types and wafers at performing the separation, as a result of surface properties or physical filter morphology.

6.9.3.1 Method

Two suspensions were prepared, one comprising solely 3 μm and the other solely 1 μm particles. The particles were prepared in concentrations not exceeding the previously established limits and applied to the centre of a variety of device types of apparent good etch morphology. The suspension was added to the central reservoir on the inverted microscope stage, as in previous studies, using a 1 μl positive displacement syringe mounted on an eppendorf NI2 injectman micromanipulator mounted the left of the stage. A right-hand mounted syringe contained

distilled water as flushing media and was subsequently used to flush the suspension through the die. Each device was then sealed with a 8 μl droplet of sterile mineral oil.

The counting algorithm described in Section 6.7.1.1 was employed to analyse a composite tilescan image of the device, taken at 20× magnification, and return population data based on their radial distance from the centre, permitting simple comparison between devices. Summing particle counts in all access wells based on discrete annuli radiating from the central reservoir allowed non-directional relationships to be observed.

6.9.3.2 Results

Separation, whilst providing access to the filtrate, was best achieved by the devices populated with linear channels, where a single threshold or barrier is supplied and employed to retard over-sized particles. In the pillar based studies it was observed that the multiple flow paths offered not only more opportunities for smaller cells to progress, but more opportunities for larger cells to deform and negotiate the obstacles, and more chances for the particles to be arrested within the filter array as opposed to within an access region.

With this consideration it would appear most effective if the channels were comprised of linear filter channels but etched to a much greater depth, providing more resilience to blocking by offering taller channel sections as opposed to alleviating the blocked condition through offering paths around blockages.

Optimal separation achieved with 3 μm particles in a single particle type suspension was found to be 52.25% of the total population being located within the 8 relevant collection chambers, which were those located at the ends of the capil-

lary branches, equating to approximately 450 particles of the initial load of 6620 being located in each end well. The optimal results for the separation of a single particle suspension are shown in table 6.4 and graphically in figure 6.35.

Separation for the 10 μm was evaluated by the same method, with the measure of effectiveness being the concentration of particles within the second filter stage. Since the larger particles were not intended to pass throughout the filter channels the test served to identify the better devices at prohibiting the particles from breaching the end filter stage. The device that performed best was the 'B3' device, ensuring almost 100% obstruction of the 10 μm particles (figure 6.35).

Filter Stage	3 μm population	3 μm %	10 μm population	10 μm %
0	200.5	3.0	89.8	2.6
1	958.3	14.5	1557.8	44.7
2	1985	30.0	1819.4	52.2
3	3457	52.5	18.2	0.5

Table 6.4: separation of 3 μm suspension using *B3-5-5* device and 10 μm suspension using *B3-4-5* device.

In all instances the devices offered little resistance to the 23 μm particles through the initial phase, this was unexpected in the case of 'B3' as it was specifically designed to arrest these particles. The fact that it did not implies that the undercutting of the channels was a minimum of 1.5 μm on either wall. The failure of the 8 μm filter stages in 'C2' to arrest the 10 μm particles supports this (figure 6.36). Also in support of this is the considerable loss of the fine 5 μm diameter filtration pillars populating the 'A' and 'B' concepts.
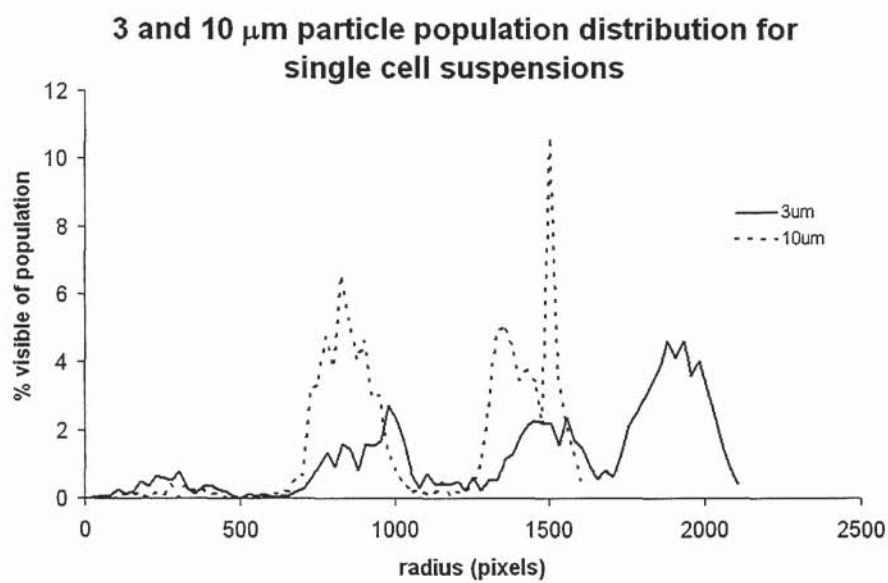
Figure 6.35: graph of optimal 3 μm and 10 μm particle separations within 'B3' filter devices with peak concentrations in final, and second collection wells respectively

10 μm particle distribution within device C2-5-7
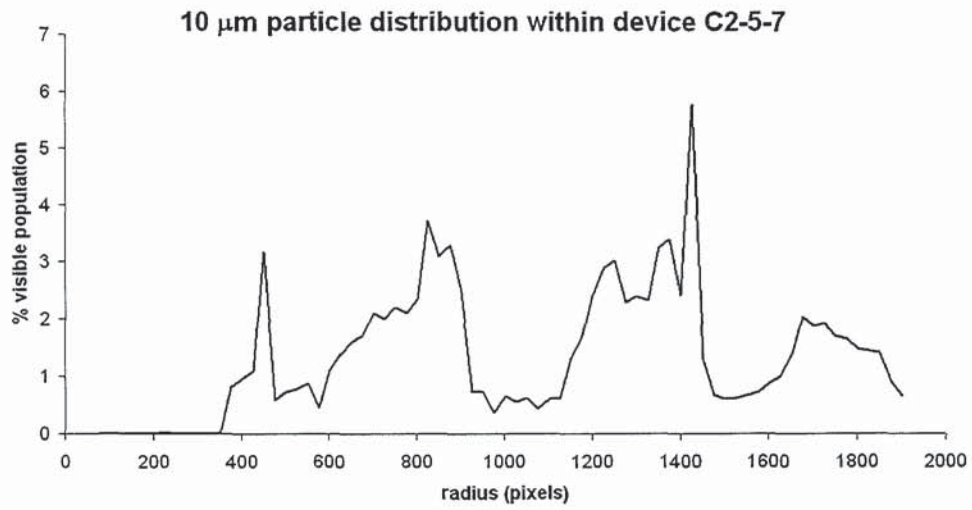
Figure 6.36: population distribution within 'C2' shows a large population of the green 10 μm particles reaching the final access well as a result of oversized filter pitch

242

Unfortunately no devices suitable for 10 μm particle testing were produced of types 'A','C' or 'D', with the majority suffering from considerable pillar attrition. However, the results for 10 μm particle migration are summarised in table 6.5.

Concept	stage 0 (%)	stage 1 (%)	stage 2 (%)	stage 3 (%)
'A'	N/A	N/A	N/A	N/A
'A2'	0.72	30.85	57.68	10.75
'B'	1.15	31.19	59.06	8.6
'B3'	3.03	14.48	29.99	52.5
'C'	N/A	N/A	N/A	N/A
'C2'	0.96	17.72	45.15	36.18
'C3'	0.98	15.61	46.31	37.1
'E'	0.17	10.87	46.44	42.52

Table 6.5: 'B3' and 'C2' concept separation performance, generous undersizing of finer filter pitch offered best separation

6.9.4 Separating Particle Types from a Binary Mixture

For this experiment a two-part mixture was prepared comprising 3 μm and 10 μm microspheres within a suspension of distilled water. A correctly functioning device should permit the flow of the smaller particles through to the ends of the channels, whilst retarding the 10 μm particles at the final filtration stage. From the previous test this was most reliably found to be a 'B3' device.

6.9.4.1 Method

The particles were fluorescently tagged with red and green stains respectively, permitting imaging of each particle type independently, and irradiated with 543 nm HeNe and 488 nm argon lasers. Additional unfiltered reflective image data was taken in order to place the particles into the context of the device under test.

Particles were prepared in approximately equal dilute populations not exceeding $4 \times 10^6/ml$, significantly higher than those occuring within the testis biopsy (table 3.1)[7] in order to ensure enough particles for clear imaging across the device. Populations were counted and verified using an improved Neubauer Haemacytometer according to standard cell counting protocols. Previous testing indicated that a suitable load-flush ratio of 1:1 was adequate and as such each device was loaded with 1 μl of particle suspension, and then immediately flushed with 1 μl of distilled water prior to sealing with an 8 μl droplet of sterile mineral oil. Loading was conducted as previously through the use of independent 1 μl positive displacement syringes.

6.9.4.2 Results

Loading a number of 'B3' devices with the binary suspension and following the flush protocol demonstrated that the device was capable of segregating the smaller

3 μm particles with the exclusion of the larger 10 μm when loaded within the the-
oretical limits of the die (figure 6.37). Also, the 10 μm particles were concentrated
within the appropriate filter access well in order that they may be preferentially
selected. Optimal concentrations of particles within their appropriate collection
wells were found to be of the order of 50% and 84% for the 3 μm and 10 μm
particles respectively, averaging 6.3% and 10.5% per individual well (table 6.6).
There was observed an almost 100% exclusion of the larger 10 μm particles within
the final access well.

Filter Stage	3 μm % population	10 μm % population
0	1.42	0.41
1	14.99	15.55
2	35.41	83.96
3	48.18	0.08

Table 6.6: separation of a mixed suspension of 3 μm and 10 μm micro-spheres
using *B3-3-6* device.

6.9.5 Separating a Mixed Population

Having previously demonstrated the capabilities of the device when using only 2
particle types, this investigation was intended to evaluate the impact of adding a
population of larger cells with the capacity for arresting and negatively impact-
ing the migration of smaller particles comprising the filtrate. Particle suspensions
were prepared in basic volumes of 300 μl in order to provide suitable quantities
of particles for use, but large enough volumes to provide adequate and complete
mixing.

Binary mixture of 3 and 10 μm particles: % population distribution
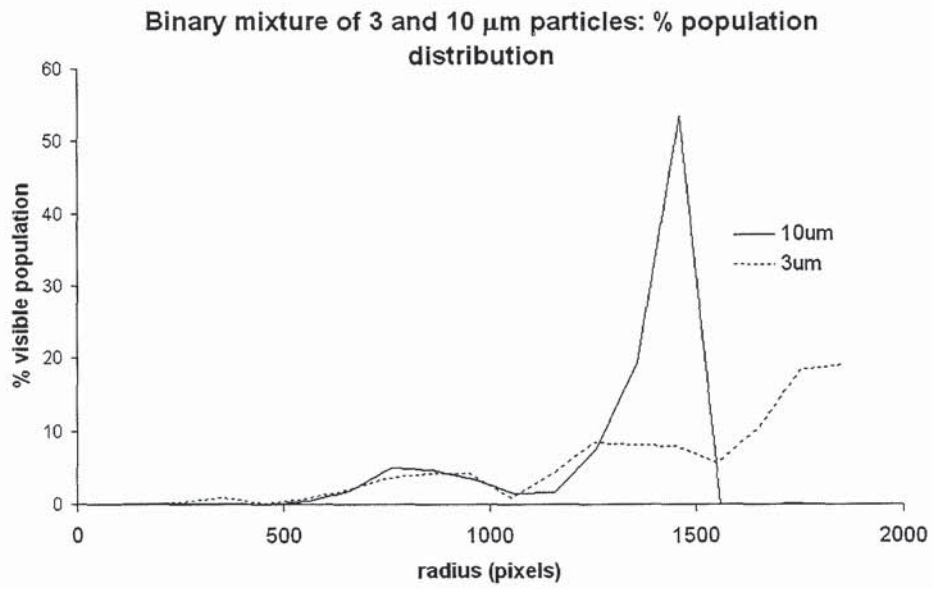
Figure 6.37: graph showing the percentage distribution of 3 and 10 μm particles across a 'B3' device after the addition of a binary mixture.

A series of cell suspension batches were prepared that contained a base population of 3 and 10 μm microspheres consistent with the acceptable populations of table 6.2, but with varying levels of 23 μm spores, as detailed in table 6.7.

batch	3 μm (red)	10 μm (green)	23 μm (unstained)
MP4-	2875	1950	900
MP3-	2875	1950	750
MP2-	2875	1950	0
MP+	2600	3200	1300

Table 6.7: three component suspension constituent populations according to batch

A control test was also conducted that contained no larger particles, denoted 'MP2' in order to identify and eliminate environmental changes or influences. Suspensions were applied through the previously presented method with a 1:1 load-flush ratio with up to the 2 μl fluid capacity of the device. After bulk particle migration was observed to have arrested the die was sealed with an 8 μl droplet of sterile mineral oil. Two tile-scan imaging cycles were executed with an interval of approximately 10-15 minutes in order to observe any settling effects. The images were processed using the particle distribution algorithm 'stagecalc.m' and compared between filter batches in order to identify the effects of larger cell populations on fluorescent particle migration.

6.9.6 Results

The control test was consistent with the results of the binary mixture separations test, and provided a clear baseline against which the obstruction results could be compared. It was observed that although being larger than the initial 20 μm filtration stage in the 'B3' devices, a number of larger particles were still able

to deform slightly and pass into the next stage. This may also be influenced by the quality of the etch, with potential undercutting of filter channels resulting in the filter stages being bigger than their design size (figure 6.38). The vast majority were however arrested as anticipated at the second filter stage for all tested populations. As the concentration was increased towards and beyond the calculated saturation level for the larger particles there was an apparent impact on the the migration patterns of the red and green particles.
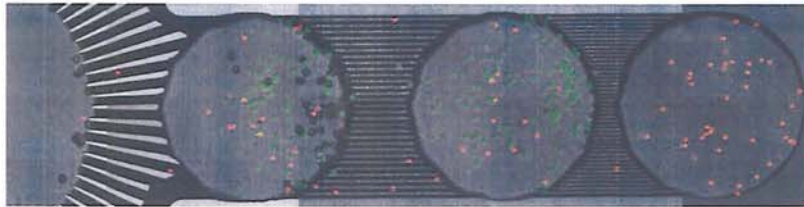
Figure 6.38: undercutting of initial filter channels result in 23 μm particles (shown as dark, round particles) passing through the 20 μm filter stage.

Applying a mixture of smaller particles that contained no larger particles (MP2) provided pronounced migration of the particles to the filter channels, with clear arrest of the 10 μm particles in the penultimate access wells. The smallest particles were spread across the entire channel, but with the highest visible concentration in the final collection chamber. Adding the theoretical upper limit of the largest particles (MP4) had the most pronounced effect on the migration of the green 10 μm particles, which were highly focussed into the second access well, but became more dispersed upstream. The highest concentration was still located at the desired well radius, however the margin over other well populations was significantly reduced. The smaller 3 μm particles did not appear to be directly affected by the addition of the larger 23 μm spores, but were indirectly affected at higher concentrations when the 10 μm distribution was significantly altered (figure 6.39).

It may therefore be concluded that the addition of larger particles with the current configuration and separation strategy does have an impact on the separation of smaller particles. An impact that increases as the added population of large particles approaches the capacity of the device. In the case of the exaggerated numbers of batch 'MP+', with elevated numbers of both 10 and 23 μm particles, the impact on particle distributions was considerable.

6.10 Discussion

6.10.1 Fluid Flow

The nature of the fluid flow was postulated to be of a quasi-static nature comprising two distinct flow stages, an initial rapid wetting and a slower assymptotically decaying equalising flow. This hypothesis was confirmed experimentally with initial wetting velocities through the test device capillary model being in close agreement with the modified Yang quasi-static marching velocity model (Section 5.2.7). This was corroborated with both the directly imaged mensicus position over time, and the motion of particles suspended within the wetting fluid.

Considering the overall imbibition time for the fluid into the capillary model with published data of the properties of water and substituting into the Washburn equation it became apparent that the static contact angle within the devices was not in line with values typical to the processed surfaces. Published data for the contact angles of raw silicon, silicon oxide and glass is scarce and vague. This is possibly a consequence of its high variability in light of chemical processing, but the values calculated from the Washburn equation imply only mild hydrophilicity

249
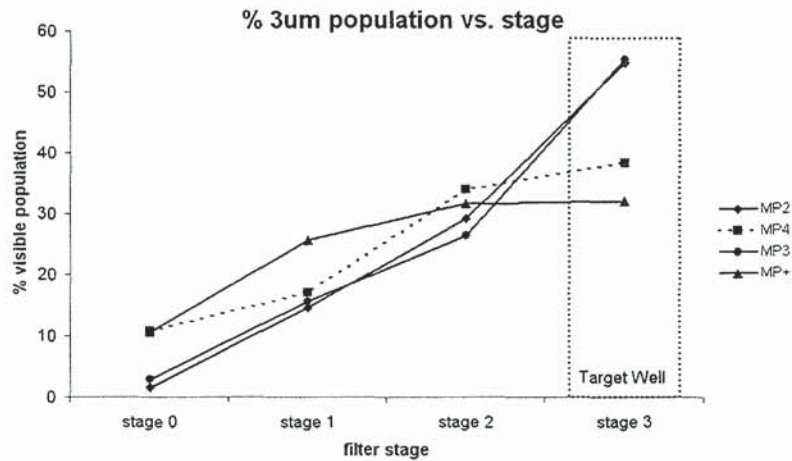
(i) Localised percentage populations of 3 μm particles
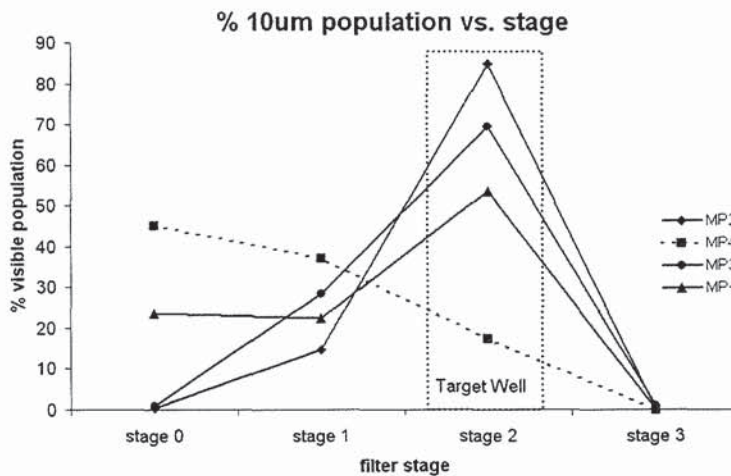
(ii) Localised percentage populations of 10 μm particles

Figure 6.39: graph illustrating the effect of increasing 23 μm particle population on (i) the distribution of 3 μm and (ii) 10 μm particles within a 'B3' device. 3 μm particles are largely unaffected, whilst the effect on 10 μm particle distribution is pronounced.

with a static contact angle of approximately 88°. It is expected that this elevated contact angle is a consequence of incomplete removal of the hydrophobic sidewall passivation applied during the manufacturing process.

As devices were aged with exposure to the air there was an apparent slowing and, in some instances, a retardation of the wetting process, with a clear distinction between freshly tested devices and those aged in excess of 24 hours. Observation of the flow as it arrested at the outlet of the test device demonstrated that it was the glass lid that was responsible for flow arrest, as opposed to the silicon substrate. This was most apparent in the wetting of the outlet well where fluid was observed to follow the walls of the well prior to spreading across the glass well base (figure 6.40).

The preferential evaporation of fluid from the devices was employed as an analogy of the wetting mechanism to illustrate the dominance of surface forces over gravimetrically induced forces. This was illustrated by the order in which collection wells were emptied throughout the evaporation process. The results indicated that access wells of a smaller diameter retained their fluid at the expense of the larger wells, until insufficient fluid remained within the system to support the meniscus. This was in agreement with the hypothesis that according to Young's Law, meniscii formed with a smaller diameter will exhibit a greater interfacial pressure than larger meniscii, that, providing surface forces to be dominant, would exceed any contributing forces as a consequence of gravimetric pressure differentials across the device.

6.10.2 Particle Distribution

The most successful device format, was that of the 'B3' type. Particle separation capabilities were observed to be consistent when using populations within the
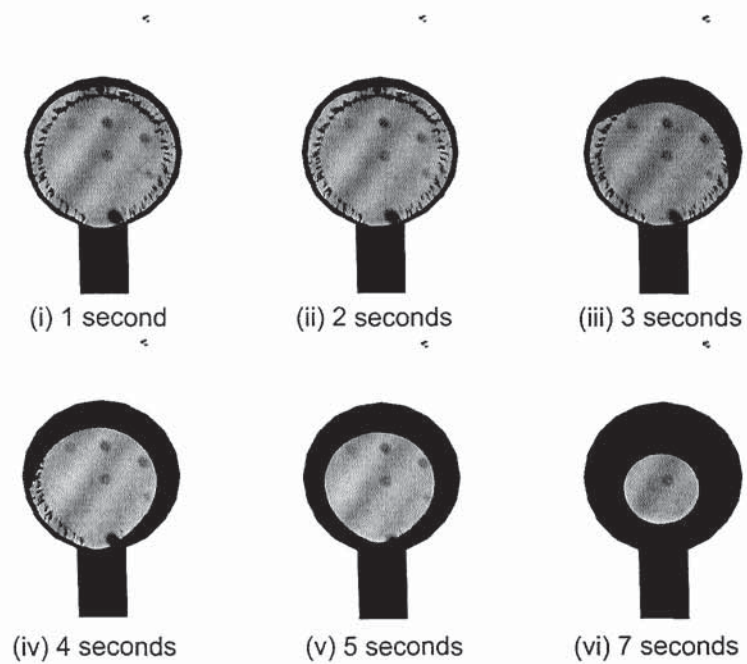
Figure 6.40: the stages of the Wetting of the outlet of an aged test device over time demonstrates the preferential wetting of the silicon walls over the glass well bottom

design limit for mixtures of 1, 2 and 3 differing particle sizes. As the design limits were approached and exceeded the efficacy of the separation process deteriorated, with lower concentrations being available in the target collection chambers, and higher populations being found in other collection chambers upstream.

The 'B3' device consistently delivered particle populations in excess of 50% of the visible cell population within the target collection wells for both 3 and 10 μm particles when using dose populations within the theoretical limits of the device. Increasing the quantity of the larger 23 μm particles appeared to primarily affect the smaller 10 μm particles, and hindered the 3 μm particles indirectly after the maximum population.

When comparing the performance of the 'B3' device with other concepts few others were capable of separating the 3 and 10 μm particles. From images taken of the last filter region, populated with filter elements of 8 μm pitch it is clear that this is a result of the poor morphology of the elements (figure 6.41). The fine filter section of the 'B3' die pattern is some 3 μm smaller than the other tested formats, offering a greater tolerance to etch and particle size variability. Thus the improved separation of the finer particles is not a reflection of a better etch morphology but rather of the final filter stage being designed under-size with sufficient capacity to accomodate undercutting effects whilst still adequately arresting the 10 μm particles.

The inability to separate the 3 and 10 μm particles was not limited to the pillar based device geometries, but was also observed in the other linear designs of 'C2' and 'H' (figure 6.42(i)). Despite being designed some 2 μm smaller than the mean particle diameter the cumulative effects of etch and particle size variability, coupled with a degree of suspected undercutting of the filter elements, results in

(i) B-2-5: close match between particles and filter pitch

(ii) E-2-1: large clearance between filter pillars unable to arrest larger particles
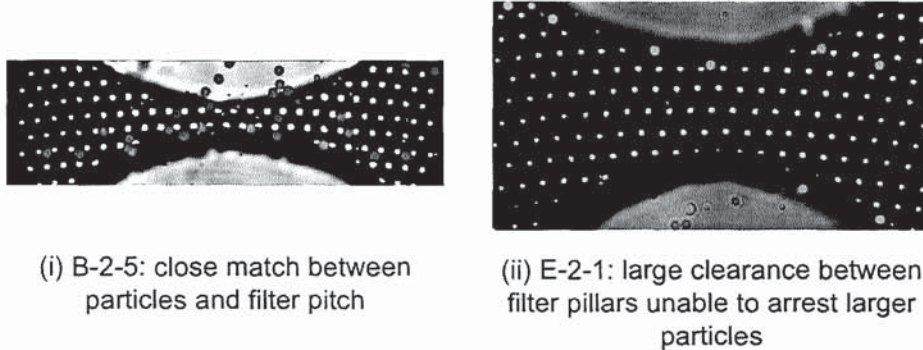
Figure 6.41: (i) the final filter stage showing the clearance between the filter pillars and the 10 μm particles in an 'E' die, and (ii) the last stage of a 'B' type die, with a smaller filter pitch but still failing to arrest the larger particles.

an over-sizing of the separation channels. This is consistent with the unexpected progress of the 23 μm particles in the 'B3' dies beyond the initial 20 μm filter to the second filter stage (figure 6.42(ii)). Pillar undercutting can be clearly seen in micrographs of some failed devices, observed as tapering of the cylindrical filter elements.

The 23 μm particle saturation limit was consistent with that estimated based on the channel capacity, as opposed to the lower figure of ≈ 250 as implied by the individual first stage filter capacity. This is as a consequence of the under-cutting of the filter elements providing passage to the oversized particles. This is a known effect of the application of DRIE to deep trench etching, which can be mitigated through improved process control and slower etch rates permitting optimal aspect ratios of 100:1 [79]. The fair evaluation of other design concepts with respect to particle separation properties would require further manufacture batches with greater attention paid to avoiding undercutting, or through the use of a larger series of particles.
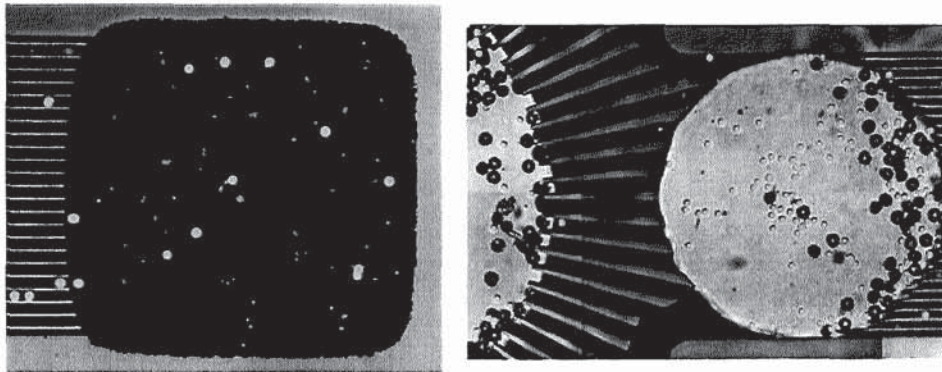
(i) final stage channels in 'C2' device   (ii) final filter stage in B3 device fine
cannot arrest larger particles   enough to arrest 10µm microspheres

Figure 6.42: (i) final filter stage in 'C2' appears to have good morphology but does not arrest the larger particles, (ii) which is consistent with the passage of 23 μm particles beyond the under-sized first stage.

Increasing the larger particle populations beyond capacities resulted in a reduction in the exclusivity of well populations, with smaller particles becoming more widely dispersed upstream of their target well. However, in the majority of cases when using a mixed population comprising three particle types or sizes, and complying with the developed loading and flushing protocols, there was consistently an elevated number of desired particle types within target wells.

Chapter 7

Discussion and Conclusions

7.1   Concluding Remarks

Through the application of microfabrication tools and techniques the potential of the self-powered single use microfilter device has been demonstrated. Exploiting the dominant surface effects of discrete micro-fluid flows a technique has been developed that can increase the probability of isolating and separating, and ultimately locating individual particle types from a homogeneous mixture based on their size and morphology within an optimal accumulation in excess of 50% of the total population.

A repeatable, discrete, unpowered flow mechanism was developed, mathematically modelled and validated, and proven to be a consequence of surface effects such as capillarity both during the initial wetting phase, and the post-wetting flow phase. The technique requires no additional fluid or power sources in order to produce useful work and can be optimised and employed for a variety of discrete fluid transport or analysis processes. The variations in flow observed between different device types and between different manufacture batches are indications of the versatility of the technique, permitting the geometrical redesign and tailoring of the wetting and flow properties.

A system was realised that required no additional parts or processes other than that required to load and image the device, permitting simple and rapid deployment of the concept within a laboratory or field environment without supplemental tooling or equipment. The technique relies upon the discontinuous nature of the sample being processed, and the subsequent sealing of the device in order to mitigate evaporative effects and as such is suitable for processing only small volumes, of the order of 1 μl.

A new approach to particle image velocimetry was developed, proven and employed to observe wetting flow-front velocities, and wetting induced particle velocities. The technique, employing conventional confocal microscopy techniques, was demonstrated to be capable of reliably imaging large areas of fluid flows with an imaging frequency in excess of 80 Hz, but at a restricted magnification and resolution.

Finally a device was developed, and evaluated with optimal use protocols, that is capable of segregating particles of similar sizes within a homogeneous suspension of mixed components in concentrations in excess of 1×10^7. Segregation was repeatably achieved, localising particle populations in proportions exceeding 50% of the total added population within seconds of loading a device.

7.2   Manufacture

The manufacture process yielded mixed results as a consequence of the procedurally taxing concept format and designs. The resulting wafers returned information on process limitations, design flaws and potential improvements of the device layout in order to make the manufacturing process more robust and the devices more resilient to variations in wafer location and etch recipe.

Through observing the wetting flow velocity of the microfabricated test structrues and subsequent determination of the static contact angle it appeared that the hydrophilicity of the channels was somewhat over-estimated, θ_c being of the order of 88°. This being the case only a slight change in channel geometry or surface energy is required in order to halt the wetting process and arrest surface tension induced flows. This was observed directly in the testing of devices exposed to the air for periods of greater than 24 hours.

As there are no other agents being applied to the surfaces it is reasonable to assume that this is a consequence of the residual polymeric sidewall passivation employed in the DRIE or Bosch process. Although this strongly hydrophobic material is intended to be removed through 'ashing', it is apparent that further efforts are required in order to reduce the presence of stubborn residues. It is perhaps, however, a testament to the robustness of the concept and comparative magnitude of the surface tension force at this scale that, despite the weak hydrophilicity of the devices, the fluid is imbibed into the device within seconds and complete flow arrest is achieved in less than a minute.

7.3 Design

Although a variety of different device concepts were developed (Section 3.7) few entirely survived the manufacture process, either as a consequence of poor process control or process limitations. Particular casualties were the 'A', 'B' and 'D' dies, with none of the latter being yielded in a condition suitable for testing. Across the devices with the best apparent etch morphology only the 'B3' devices demonstrated appropriate separation characteristics in at least some of the test particles. All devices demonstrated a degree of undercutting during manufacture, but it was the 'B3' concept that incorporated an allowance for this in its geometry,

with the latter filter stages being considerably under-sized. Consequently, these stages were closer to the intended filter pitch upon manufacture, whereas the manufactured filter stages of the other concepts were considerably over-sized. This is supported by 'B3' concept performance data as summarised in table 7.1, which illustrates correct accumulation of 3 and 10 μm particles, whilst the larger 23 μm particles progressed further than intended.

Filter stage	design size	arrested particle size
'B3' 1	20 μm	N/A
'C2' 1	25 μm	N/A
'B3' 2	10 μm	23 μm
'C2' 2	15 μm	23 μm
'B3' 3	5 μm	10 μm
'C2' 3	8 μm	N/A

Table 7.1: 'B3' and 'C2' concept separation performance, generous under-sizing of finer filter pitch offered best separation

These effects are reflected across all devices tested. However, if an improved or refined manufacturing process were applied , as opposed to the exploratory methods that were used, then it is conceivable that other device concepts could provide better separation characteristics. Further testing would be required with higher quality devices in order to determine this. Nonetheless it may be said that for the most robust device, with the least sensitivity to the DRIE manufacture process, the filter pitch should be several microns smaller than the particles they are intended to arrest in order to accomodate variations in aspect ratio (undercutting), particle size and potential for particle deformation.

259

7.4   Concept Evaluation

The optimal design solution from the perspective of cell segregation and subsequent retrieval comprised linear channels of fixed section. Although providing fewer pathways for fluid flow when compared with pillar based devices, the linear walls significantly reduced the chance for cells arresting within the filter section where they are inaccessible to the user. In the event of the changes to device surface chemistry through pollution or oxidation a multitude of discrete pillars can serve to obstruct flow by creating a multitude of severe geometrical changes that adversely alter the effective contact angle.

The radial array of filtration channels was significant to the design in that they offered redundancy, thus allowing flow to continue in the event of a blockage, whilst providing a minimal loading reservoir volume. Also important to the flow was the size of the access wells being less than that of the inlet reservoir, ensuring the fluid is drawn from the centre to fill these outer wells.

The small volumes of fluid inherent in microfluidic systems will always be strongly influenced by ambient effects, most specifically temperature. In such applications, unless a means of mitigating evaporation is incorporated, fluid will be lost rapidly due to fast evaporation. Without the addition of a large fluid reservoir there is little option but to either continuously feed the device with more flushing media, or to apply a viscous coating that will sacrificially evaporate at a lower rate in order to prevent loss of the working fluid.

The multiple flush cycles facilitated by the evaporation and subsequent flush mechanism is limited in its efficacy as a consequence of the geometry of the devices themselves. The central reservoir, having the single largest continuous liquid-gas interface, is the site at which evaporation principally occurs. The

smaller access wells having smaller interfaces with higher surface tension forces suffer from this effect much more slowly. As a result, the bulk of fluid is lost from the central reservoir during evaporation and there is little migration of fluid from the access wells till the central reservoir is empty. Adding flush media to the central reservoir after evaporation principally serves to refill this reservoir with only a comparatively small amount of fluid being imbibed into the other wells. In the majority of the observed cases after the initial flush cycle is completed and the device is saturated there is little subsequent fluid and particle migration as a consequence of flushing.

In order for more effective flushing cycles to be facilitated evaporation must be more strictly controlled such as to restrict evaporation to the outer access wells, or to providing additional drains beyond the outer access wells encouraging the flow of more fluid and fluid-borne particles beyond the final filter stage.

7.5 Potential Applications

Beyond the application for which the devices were initially designed the techniques developed may be appropriate for a number of other situations or problems. The most clearly apparent applications are those centred on discrete sample particle separation where a passive mechanism is required for propelling a fluid and separating fluid-borne particles. However, the fluid imbibition principle could be applied to a vast array of bio-MEMS technologies requiring rapid and discrete fluid flows with minimal external influences.

The filtration technique, aside from cell segregation, could be readily applied to the preparation of finely filtered liquids for lab-on-chip devices, drawing raw fluids from field studies into increasingly fine capillary networks till it is clean enough

to be imaged or interrogated by chemical sensing techniques.

A strength of the process can be considered to be its ability to rapidly handle small volumes. In the case of in-the-field preliminary testing where 100% accuracy is not required, tools based on the microfilter could be used as indicators as to whether further laboratory-based testing is required, such as in the case of water quality testing. For instance, rudimentary blood analysis could be achieved in front-line or point-of-care situations, and the separated cells could then be preserved and subsequently aspirated for further analysis to be conducted on samples displaying unusual morphology. A clear example of this technique would be to use the separation of key components within blood in order to detect elevated white blood cell levels in the diagnosis of infection, or platelet populations in the diagnosis of disorders such as thrombocytopenia (Mr. D. Proops[1], personal communication, 2006).

Simililarly there is capacity for the device to be employed in the brewing and fermentation industry. Yeasts are aged based on the number of cell divisions that they undergo, with virgin cells being undivided and daughter cells having undergone several divisions. Yeasts, typically *Saccharomyces cerevisiae*, have a useful life as they apply to brewing, with older cells being of little use to the fermentation process. It is understood that for optimal fermentation conditions an even balance of yeasts of all ages should be used to produce consistent product[99]. As yeast cells undergo cell divisions they undergo morphological changes, budding scar formation and an overall increase in size, with the oldest cells being volumetrically six times larger than first division 'mother' yeasts [100]. The devices and technologies developed in this study could be readily applied in the rapid front-line testing of small sample volumes for the observation of yeast population

---

[1]Queen Elizabeth II Hospital, Birmingham

distributions within a brewing process with little modification.

The devices are self-contained, but providing access to the filtrate as necessary, with the default state being to encapsulate the filtrate within the structure of the device. The volumes involved are small, held in place within the wells of the die by the surface tension of the fluid, so the opportunities for filtrate leakage upon disposal are few. This considered, disposal of the die and its contents are suited to conventional biohazardous waste protocols.

7.5.1 Biochemical staining

An alternative application for which the devices have been successfully applied is in conducting micro-volume biochemical stains with low cell populations. The fine filtration structures were successfully employed as a means of immobilising unfixed fungal cells for the purposes of viability staining and imaging of cell populations of the order of $1 \times 10^3/\mu l$.

Living and dead Candida wild type cells were suspended in Hepes buffer solution and added in a 1 μl droplet to the end collection chamber of a type 'H' device. A 1 μl droplet of stain prepared in buffer solution was added immediately afterwards and added to the same well. The process was repeated with both live and dead stains from the Fungalight Yeast Viability Kit (Molecular Probes), comprising SYTO 9 and propidium iodide (PI) stains respectively. Both stains were excited at 488 nm with argon laser light and imaged at 500 and 650 nm along with a contextual reflective image. In-situ staining results were compared against prestained and unstained samples in order to qualitatively compare the efficacy of the method. The resulting scan-images are presented and summarised in figure 7.1, and illustrate that even when applied to devices showing relatively

poor filter morphologies, the use of the devices as a technique for trapping cells and serially processing them with multiple stains is one of considerable potential.

(i) Control: Unstained cells in buffer

(ii) Control: Pre-stained (PI) dead cells in buffer

(iii) dead cells in buffer stained (PI) on device

(iv) Pre-stained (SYTO 9 + PI) live cells in buffer

(v) live/dead mixture in buffer stained (SYTO 9 + PI) on device
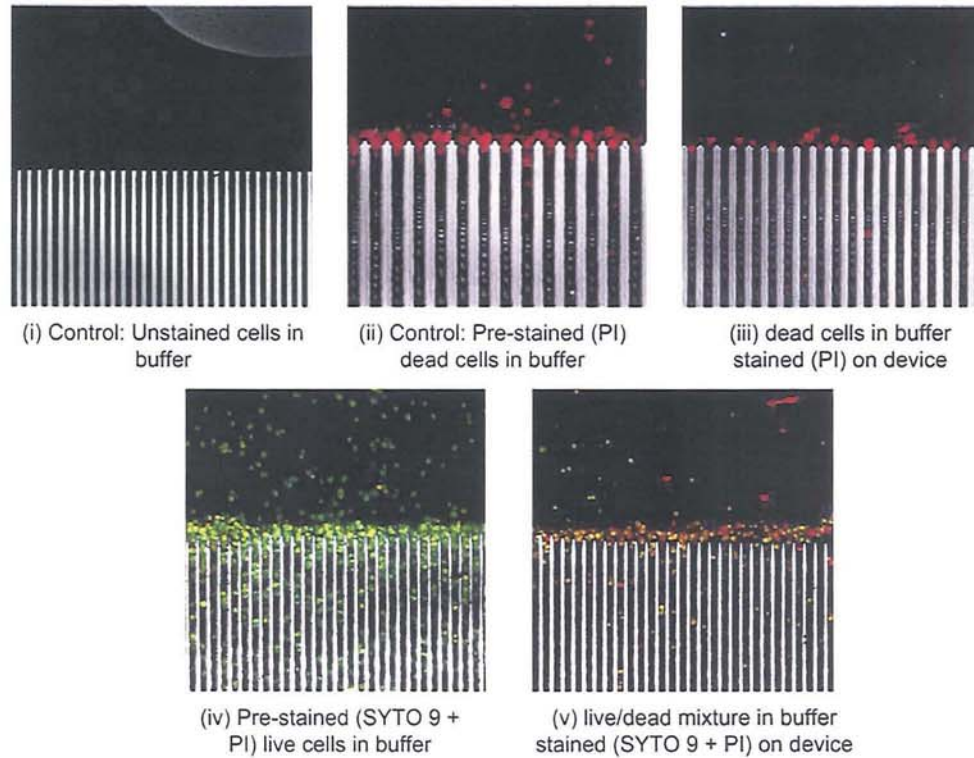
Figure 7.1: (i) unstained cells have no fluorescent or reflective visual signature, (ii) prestained dead cells can be clearly seen arrested at filter elements, (iii) and dead cells stained with PI are also readily imaged. (iv) prestained live cells are also clearly visible, (v) both stains are seen in the mixture of live and dead cells stained sequentially with SYTO 9 and PI on the device.

Applying stains using the filtration device as an immobilisation technique offers considerable advantage over conventional preparation and staining techniques in that it offered considerable reductions in

analyte volume: smaller volumes of both sample and staining reagents were required in order to provide a positive or negative result from the viability test

processing population: a reduced processing volume offers potential for a direct reduction in the sample population to be processed. This translates to a time advantage for rare samples as a result of a reduced need to cultivate large populations as would conventionally be required.

processing time: in addition to reductions in preparation time there is less requirement for extended periods of incubation for the stains to be provided access to the cells. The flushing of the stains past the trapped cells offer equal access for the stain to all cells for the same period. In the case of the Fungalight viability stains imaging was possible immediately after the application of the stain to the device.

imaging considerations: immobilising un-fixed cells through cellular accumulation at filtration elements permitted slow, high resolution scanning of the cells without the need to bias results through artificial fixing methods. The cell accumulation also assists in the rapid location and identification of cells although it can limit the opportunities for imaging single cells or small cell groups if required.

7.6 Limitations of the Technique

Although quick, repeatable and simple, access to individual separated cells and particles is partially hampered by the structure of the device itself such that the cells are aspirated as a component of the bulk fluid. Although sound in principle, the available fluid is finite when sealed by the oil, thereby limiting the amount

of fluid that can be aspirated without risking contamination of the sample and device by oil ingress.

Further to this, although the device principles may reduce the operational skill required in isolating or locating a cell within a suspension, the dies in their current incarnation do not de-skill the task of aspirating or acquiring the cells from the filtrate. The fine scale of the devices affect the loading and handling of the filtrate. Dexterity and confidence with micromanipulation equipment is still necessary for harvesting useful cells from the relevant regions within the chip. It is not possible to load the devices by hand using a fine syringe as the 800 and 300 μm diameter access wells are too small a target for reliable loading. As such it is a requirement that loading and aspiration are conducted using micromanipulation techniques or perhaps through bespoke loading/unloading jigs or apparatus.

The small volumetric capacity of the dies limit the processing volume to a maximum of $2\mu l$ including any flush media. This can be increased through incorporating incomplete evaporation cycles into the process, however experimentation and analysis corroborate that flushing beyond a load-to-flush ratio of 1:1 shows limited improvement in particle migration, and that flushing after initial saturation of the device only serves to clear debris from the central reservoir.

A further limitation of the technique is in the preparation of the filtrate. Although not requiring fine filtration, the prior removal of larger particles and accumulations significantly improves the efficacy of the process at separating the desired cells. Blockages upstream in the more effective concept designs have been demonstrated to severely impede smaller particle progression up the filter channels.

A complication as a result of the scale and complexity of the separation elements mean that cleaning of a device, that is the guaranteed removal and cleansing of

any polluting tissues or cells, is not possible. Although intended for single use, multiple uses, if desired, are not advisable. Multiple washing cycles in an attempt to remove debris and contaminants resulted in the damage of the fine intrachannel walls or filtration elements, and the repeated use of solvents and cleansing agents proved ineffective at completely removing particulates from the device.

Perhaps a consequence of incomplete cleaning and preparation of the filter walls, the side-walls of the devices exhibited the remains of hydrophobic coatings that although unharmful to biological matter, caused a number of inconsistencies in the flow of fluid through the devices as a result of fluctuations in the static contact angle.

More limitations arise as a result of the chosen manufacturing process. DRIE has an effective feature or trench size limitation of the order of $1\mu m$, consequently for finer filtration to be achieved then further post-etch modifications are required to the wafer, for example applying or growing inorganic or biological wall coatings.

7.7 Suggested Further Work

Further work is suggested prior to the deployment of the device into a clinical environment for the target application of valuable spermatogenic cells, and is summarised as:

1. Aspiration studies, quantification of the proportion of particles that may be successfully liberated post-separation from the collection chambers.

2. Evaluation of the separation mechanism in clinical trials with eukaryotic cells, and comparison with non-biological tests in order to assess any possible different requirements such as surface adherence or cellular interaction

(accumulating and clogging).

3. Further development of the concept is required in order to subtend a reliable deployable clinical device.

4. Refinement of the die morphology is required for both making a more robust manufacturing method, and a more effective flow and separation strategy.

5. The inclusion of larger volume processing, a larger loading well to facilitate easier loading with percolation elements to provide more effective initial filtration without obstructing individual channels.

6. The addition of a drain in order to extend the period of flow beyond the last filtration stage thereby increasing the opportunities for cells to migrate up the channels and subsequently reach their desired destination. The drain itself could take the form of a long meandering capillary extending from the final channel filter stage such that any drawn fluid is sealed harmlessly within the substance of the die. Alternatively, but much less desirably, the drain could be to an external reservoir filled with absorbant media. This would add to the complexity of using the devices, but would maintain the small size of die.

7. There is potential for manufacturing the device from a polymer such as PDMS at a considerably lower cost, forming it from a silicon master. This would of course require other bonding strategies and perhaps die reinforcement, as well as suitable surface energy modification through chemical methods such as etching with Hydrochloric acid. This would in turn need investigating for biocompatibility and the effective 'shelf-life' of the surface properties.

References

[1] J.P. Brody, T.D. Osborne, F.K. Forster, and P. Yager. A planar microfabricated fluid filter. *Sens. and Actuators A*, 54:704–708, 1996.

[2] H.E. Reiss. *Reproductive Medicine: from A-Z*. Oxford University Press, USA, 1998.

[3] anon. image courtesy of saad specialist hospital, accessed 2005. URL http://www.saadmedical.com/.

[4] P.N. Schlegel, G.D. Palermo, M. Goldstein, S. Menedez, N. Zaninovic, L.L. Veeck, and Z. Rosenwaks. Testicular sperm extraction with intracytoplasmic sperm injection for non-obstructive azoospermia. *Urology*, 49:435–440, 1997.

[5] Institute for Reproductive Medicine and Science of Saint Barnabus, accessed 2006. URL http://www.sbivf.com/male_surgeries.htm.

[6] N.T. Nguyen and S.T. Wereley. *Fluid Mechanics Theory in Fundamentals and Applications of Microfluids*, pages 16–9. Artech House Inc., Boston, fourth edition, 1998.

[7] I. Aslam, A. Robins, K. Dowell, and S. Fishel. Isolation, purification and assessment of viability of spermatogenic cells from testicular biopsies of azoospermic men. *Hum. Reprod.*, 13(3):639–645, 1998.

[8] P. Vanderzwalmen, M. Nijs, R. Schoysman, G. Bertin, B. Lejeune, B. Vandamme, S. Kahraman, and H. Zech. The problems of spermatid injection in the human: the need for an accurate morphological approach and selective methods for viable and normal cells. *Hum. Reprod.*, 13(3):515–519, 1998.

[9] D. Levran, H. Nahum, J. Farhi, and A. Weissman. Poor outcome with round spermatid injection in azoospermic patients with maturation arrest. *Fertil. Steril.*, 74(3), 2000.

[10] M.J. Madou. *Fundamentals of microfabrication: the science of miniaturisation. Second Edition.* CRC Press, London, 2002.

[11] C-S Lia, G-B Lee, H-S Liu, T-M Hsieh, and C-H Luo. Miniature rt-pcr system for diagnosis of rna-based viruses. *Nucleic Acids Res.*, 33(18), 2005.

[12] M. Srinivasan, D. Sedmak, and S. Jewell. Effect of fixatives and tissue processing on the content and integrity of nucleic acids. *Am. J. Pathol.*, 161(6):1961–71, 2002.

[13] R.T. Mansour, A. Kamal, I. Fahmy, N. Tawab, G.I. Serour, and M.A. Aboulghar. Intracytoplasmic sperm injection in obstructive and non-obstructive azoospermia. *Hum. Reprod.*, 12(9):1974–1979, 1999.

[14] E.N Tavmergen Göker, F. Sendag, R. Levi, H. Sendag, and E. Tavmergen. comparison of the ICSI outcome of ejaculated sperm with normal, abnormal parameters and testicular sperm. *Eur. J. Obstet. Gynecol. Reprod. Biol.*, 104:129–136, 2002.

[15] R. Bernabeu, N. Cremades, K. Takahashi, and M. Sousa. Successful pregnancy after spermatid injection. *Hum. Reprod.*, 13(7):1898–1900, 1999.

[16] G. Palermo, H. Joris, P. Devroey, and A.C. Van Steirteghem. Pregnancies after intracytoplasmic injection of single spermatozoon into an oocyte. *Lancet*, 340:17–8, 1992.

[17] G. Verheyen, E. Crabbé, H. Joris, and A. Van Steirteghem. Simple and reliable identification of the human round spermatid by inverted phase-contrast microscopy. *Hum. Reprod.*, 13(6):1570–1577, 1998.

[18] R.W. Applegate and J. Squier. Optical trapping, manipulation and sorting of cells and colloids in microfluidic systems with diode laser bars. *Optics Express*, 12(19):4390, 2004.

[19] A. Ashkin. Optical trapping and manipulation of neutral particles using lasers. *Proc. Natl. Acad. Sci. USA*, 94:4853–4860, 1997.

[20] S.C. Kuo. Using optics to measure biological forces and mechanics. *Traffic*, 2:757–763, 2001.

[21] C. Gosse and V. Croquette. Magnetic tweezers: Micromanipulation and force measurement at the molecular level. *Biophys. J.*, 82(6):3314–3329, 2002.

[22] C.K. Sun, Y.C. Huang, P.C. Cheng, H.C. Liu, and B.L. Lin. Cell manipulation by use of diamond microparticles as handles of optical tweezers. *J. Opt. Soc. Am. B*, 18(10):1483–1490, 2001.

[23] H. Lee, T.P. Hunt, and R.M. Westervelt. Magnetic and electric manipulation of a single cell in fluid. *Mat. Res. Soc. Symp. Proc.*, 820, 2004.

[24] M. Diop and R. Taylor. Soft trapping and manipulation of single cells in fluids by use of a stable microbubble generated at the tip of an optical fiber probe. 2005.

[25] M. Diop and R. Taylor. Soft trapping and manipulation of cells using a disposable nanoliter biochamber. *Biophys. J.*, 90:3813–3822, 2006.

[26] N. Chronis and L.P. Lee. Electrothermally activated su-8 microgripper for single cell manipulation in solution. *J. Microelectromech. S.*, 14(4):857–863, 2005.

[27] Leonard. A. Herzenberg, D. Parks, B. Sahaf, O. Perez, M. Roederer, and Leonore. A. Herzenberg. The history and future of the fluorescence activated cell sorter and flow cytometry: A view from stanford. *J. Clin. Chem.*, 48(10):1819–1827, 2002.

[28] M. Gad el Hak. *Flow Physics in The* MEMS *Handbook*, pages 4–5. CRC Press, Boca Raton FL, 2002.

[29] D. Erickson and D. Li. Integrated microfluidic devices. *Anal. Chim. Acta.*, 507:11–26, 2004.

[30] B.H. Weigl, R.L. Bardell, and C.R. Cabrera. Lab-on-a-chip for drug development. *Adv. Drug Delivery Rev.*, 55:349–377, 2003.

[31] B.H. Weigl. Microfluidics-based lab-on-a-chip systems. *IVD Technology Magazine*, Nov/Dec, 2000.

[32] J.W. Judy. Biomedical applications of MEMS. *Measurement Science and Technology Conference, Anaheim, CA*, pages 403–414, January 20-22, 2000.

[33] C. Hansen and S.R. Quake. Microfluidics in structural biology: smaller, faster... better. *Curr. Opin. Struct. Biol.*, 13:538–544, 2003.

[34] C.J. Kim. MEMS devices based on the use of surface tension. Charlottesville, VA, Dec 1999. International Semiconductor Device Research Symposium.

[35] S. Bouaidat, O. Hansen, H. Bruus, C. Berendsen, N.K. Bau-Madsen, P. Thomsen, A. Wolff, and J. Jonsmann. Surface-directed capillary system; theory, experiments and applications. *Lab Chip*, 5:827–36, 2005.

[36] E.W. Washburn. The dynamics of capillary flow. *Phys. Rev.*, 17(3):273–283, Mar 1921. doi: 10.1103/PhysRev.17.273.

[37] L-J. Yang, T-J. Yao, and Y-C. Tai. The marching velocity of the capillary meniscus in a microchannel. *J. Micromech. Microeng.*, 14:220–225, 2004.

[38] N.R. Tas, J. Haneveld, H.V. Jansen, M. Elwenspoek, and A. van den Berg. Capillary filling speed of water in nanochannels. *App. Phys. Lett.*, 85(15): 3274–76, 2004.

[39] F. Kemling. The effect of surface roughness on capillary imbibition. Master's thesis, Lulea University of Technology, Department of Mathematics, 2003.

[40] D. Erickson, D. Li, and C.B. Park. Numerical simulations of capillary-driven flows in nonuniform cross-sectional capillaries. *J. Coll. Int. Sci.*, 250:422–430, 2002.

[41] V. D. Sobolev, N. V. Churaev, M. G. Velarde, and Z. M. Zoriny. Surface tension and dynamic contact angle of water in thin quartz capillaries. *J. Coll. Int. Sci.*, 222:51–54, 2000.

[42] D.J. Beebe B. Zhao, J.S. Moore. Surface-directed liquid flow inside microchannels. *Science*, 291(5506):1023–6, 2001.

[43] H. Andersson, W. van der Wijngaart, P. Griss, F. Niklaus, and G. Stemme. Hydrophobic valves of plasma deposited octafluorocyclobutane in DRIE channels. *Sens. Actuators B*, 75(1):136–141, 2001.

273

[44] N. Tas, T. Sonnenberg, H. Jansen, R. Legtenberg, and M. Elwenspoek. Stiction in surface micromachining. *J. Micromech. Microeng.*, 6:385–97, 1996.

[45] D.C. Duffy, H.L. Gillis, J. Lin, N.F. Sheppard, Jr., and G.J. Kellogg. Microfabricated centrifugal microfluidic systems: Characterization and multiple enzymatic assays. *Anal. Chem.*, 71:4669–4678, 1999.

[46] M. Gad el Hak. The fluid mechanics of microdevices - the freeman scholar lecture. *J. Fluids Eng.*, 121:5–33, 1999.

[47] J. Koo and C. Kleinstreuer. Liquid flow in microchannels: experimental observations and computational analyses of microfluidics effects. *J. Micromech. Microeng.*, 13:568–579, 2003.

[48] J.I. Molho, A.E. Herr, T.W. Kenny, M.G. Mungal, M.G. Garguilo, P.H. Paul, M. Deshpande, J.R. Gilbert, P.M. St. John, T.M. Woudenberg, and C. Connell. Fluid transport mechanisms in microfluidic devices. volume 66. ASME International Mechanical Engineering Congress and Exposition, 1998.

[49] D.J. Laser and J.G. Santiago. A review of micropumps. *J. Micromech. Microeng.*, 14:R35–64, 2004.

[50] S. Devasenathipathy, J.G. Santiago, S.T. Wereley, C.D. Meinhart, and K. Takehara. Particle imaging techniques for microfabricated fluidic systems. *Exp. Fluids.*, 34:504–514, 2003.

[51] K. Shinohara, Y. Sugii, A. Aota, A. Hibara, M. Tokeshi, T. Kitamori, and K. Okamoto. High-speed micro-PIV measurements of transient flow in microfluidic devices. *Meas. Sci. Technol.*, 15:1965–1970, 2004.

[52] D. Sinton. Microscale flow visualization. *Microfluid. Nanofluid.*, 1:2–21, 2004.

[53] S-H. Chao, M.R. Holl, J.H. Koschwanez, R.H. Carlson, L-S. Jang, and D.R. Meldrum. Velocity measurement in microchannels with a laser confocal microscope and particle linear image velocimetry. *Microfluid. Nanofluid.*, 1:155–160, 2005.

[54] A.G. Koutsiaris, D.S. Mathioulakis, and S. Tsangaris. Microscope PIV for velocity-field measurement of particle suspensions flowing inside glass capillaries. *Meas. Sci. Technol.*, 10:1037–46, 1999.

[55] M.M. Mielnik and L.R. Saetran. Micro particle image velocimetry an overview. *Turbulence*, 10:83–90, 2004.

[56] J.G. Santiago, S.T. Wereley, C.D. Meinhart, D.J. Beebe, and R.J. Adrian. A particle image velocimetry system for microfluidics. *Exp. Fluids.*, 25: 316–319, 1998.

[57] R. Lima, S. Wada, K. Tsubota, and T. Yamaguchi. Confocal micro-PIV measurements of three-dimensional profiles of cell suspension flow in a square microchannel. *Meas. Sci. Technol.*, 17:797–808, 2006.

[58] J.H. Kang and J. Park. Technical paper on microfluidic devices cell separation technology. *APBN Vol. 9 No. 21 2005*, 9(21):1135–46, 2005.

[59] A.Y. Fu, C. Spence, A. Scherer, F.H. Arnold, and S.R. Quake. A microfabricated fluorescence-activated cell sorter. *Nat. Biotechnol.*, 17:1109–11, 1999.

[60] H.P. Chou, C. Spence, A. Scherer, and S.R. Quake. A microfabricated

device for sizing and sorting dna molecules. *Proc. Natl. Acad. Sci.*, 96: 11–13, 1999.

[61] C.C Chen, S. Zappe, O.Sahin, X.J. Zhang, E.E.M Furlong, M. Fish, M. Scott, and O. Solgaard. Microfluidic switch for embryo and cell sorting. Boston, MA, June 2003. 12th International conference on TRANSDUC-ERS, Solid State Sensors, Actuators and Microsystems, IEEE.

[62] D. Huh, Y. Kamotani W. Gu, J.B. Grotberg, and S. Takayama. microfluidics for flow cytometric analysis of cells and particles. *Physiol. Meas.*, 26: 73–98, 2005.

[63] N.R. Harris, M. Hill, R. Townsend, N.M. White, and S.P. Beeby. Performance of a micro-engineered ultrasonic particle manipulator. *Sens. and Actuat. B*, 111(112):481–486, 2005.

[64] F. Petersson, A. Nilsson, C. Holm, H. Jönsson, and T. Laurell. Separation of lipids from blood utilizing ultrasonic standing waves in microfluidic channels. *Analyst*, 129:938–934, 2004.

[65] A. Nilsson, F. Petersson, H. Jönsson, and T. Laurell. Acoustic control of suspended particles in micro fluidic chips. *Lab Chip*, 4:131–135, 2004.

[66] M.P. MacDonald, S. Neale, L. Paterson, A. Richies, K. Dholakia, and G.C. Spalding. Cell cytometry with a light touch - sorting microscopic matter with an optical lattice. *J. Biol. Regul. Homeost. Agents.*, 18:200–5, 2004.

[67] W. Ehrfield and D. Munchmeyer. US patent 04797211: Cross flow microfilter, 1989.

[68] B. He, L. Tan, and F. Regenier. Microfabricated filters for microfluidic analytical systems. *Anal. Chem.*, 71(7):1464–1468, 1999.

[69] R.H. Austin, W.D. Volkmuth, and L.C. Rathbun. US patent 5837115: Microlithographic array for macromolecule and cell fractionation, 1998.

[70] H. Andersson, W. van der Wijngaart, and G. Stemme. Micromachined filter-chamber array with passive valves for biochemical assays on beads. *Electrophoresis*, 22:249–257, 2001.

[71] L.J Kricka and P. Wilding. US patent 05296375: Mesoscale sperm handling devices, 1994.

[72] L.J Kricka and P. Wilding. US patent 5744366: Mesoscale devices and methods for analysis of motile cells, 1998.

[73] R.H. Carlson, C.V. Gabel, S.S. Chan, and R.H. Austin. Self-sorting of white blood cells in a lattice. *Phys. Rev. Lett.*, 79(11):2149–2152, 1997.

[74] O. Ohman. US patent 0042766: Micro fluidic structures, 2005.

[75] G.P. Lopez, S.R.J. Brueck, L.K. Ista, M. O'Brien, and S.D. Hersee. US patent 6685841: Nanostructured devices for separation and analysis, 2004.

[76] N. Maluf and K. Williams. *Materials for* MEMS *in An Introduction to Microelectromechanical Systems Engineering*. Artech House, Inc., Norwood, MA, second edition, 2004.

[77] L.K. Chau, T. Osborn, C.C. Wu, and P. Yager. Microfabricated silicon flow-cell for optical monitoring of biological fluids. *Anal. Sci.*, 15:721–724, August 1999.

[78] B.A. Weisenberg and D.L. Mooradian. Hemocompatibility of materials used in microelectromechanical systems: Platelet adhesion and morphology in vitro. *J. Biomed. Mater. Res.*, 60:283–291, 2002.

[79] J. Bhardwaj, H. Asraf, and A. McQuarrie. Dry silicon etching for MEMS. Annual Meeting of the Electrochemical Society, May 4-9 1997.

[80] N. Maluf and K. Williams. *An Introduction to Microelectromechanical Systems Engineering.* Artech House, Inc., Norwood, MA, second edition, 2004.

[81] L. Johnson, C. Staub, W.B. Neaves, and R. Yanagimachi. Live human germ cells in the context of their spermatogenic stages. *Hum. Reprod.*, 16 (8):1575–1582, 2001.

[82] Society for Assisted Reproductive Technology Practice Committee. Round spermatid nucleus injection (rosni). *Fertil. Steril.*, 80(3):687–9, 2003.

[83] S.Kahraman, G. Polat, M. Samli, E. Sözen, O.D. Özgün, K. Dirican, and T. Özbiçer. Multiple pregnancies obtained by testicular spermatid injection in combination with intracytoplasmic sperm injection. *Hum. Reprod.*, 13 (1):104–110, 1998.

[84] P.F. Man, C.H. Mastrangelo, M.A. Burns, and D.T. Burke. Microfabricated capillarity-driven stop valve and sample injector. Heidelberg, Germany, January 1998. MEMS Conference, IEEE.

[85] E. Hernández-Baltazar and J. Gracia-Fadrique. Elliptic solution to the young–laplace differential equation. *J. Coll. Int. Sci.*, 287:213–216, 2005.

[86] S. DiBartolomeo and J. Warrick. *ASM3500W DXF to GDSII Bidirectional Translator technical support manual*, 2003. Artwork Conversion Software, Inc.

[87] R.W. Fox and A.T. McDonald. *Fluid as a continuum in Introduction to Fluid Mechanics.* Springer-Verlag, New York, second edition, 1982.

[88] W.M. Deen. *An Analysis of transport phenomena*. Oxford University Press, Oxford, 1998.

[89] M. Gad el Hak. *Liquid flows in microchannels in The* MEMS *Handbook*, pages 6–3. CRC Press, Boca Raton FL, 2002.

[90] H. Eyring and T. Ree. Significant liquid structures, vi. the vacancy theory of liquids. *Proc. N.A.S.*, 47:526–537, 1961.

[91] R.F. Probstein. *Physicochemical hydrodynamics: An introduction. 2nd Edition*. John Wiley and Sons, New Jersey, USA, 2003.

[92] S. Chakraborty. Dynamics of capillary flow of blood into a microfluidic channel. *Lab Chip*, 5:421–430, 2005.

[93] M. Gad el Hak, editor. *The* MEMS *Handbook*. CRC Press, Boca Raton FL, 2002.

[94] G. Martic, F. Gentner, D. Seveno, D. Coulon, and J. De Coninck. A molecular dynamics simulation of capillary imbibition. *Langmuir*, 18:7971–7976, 2002.

[95] J.F. Douglas, J.M. Gasiorek, and J.A. Swaffield. *Fluid Mechanics: Fourth Edition*. Prentice Hall, Harlow, Essex, 2001.

[96] T. Cubaud and C-M Ho. Transport of bubbles in square microchannels. *Phys. of Fluids*, 16(12):4575–4585, 2004.

[97] C.J. Hamel. [MEMS-talk] contact angle, accessed 2006. URL http://mail.mems-exchange.org/pipermail/mems-talk/2002-July/. forum posting on factors affecting Si contact angles.

[98] S.D. Senturia. *Fluids in Microsystem Design*. Kluwer Academic Publishers, USA, 2001.

[99] C.D. Powell, S.M. Van Zandycke, D.E. Quain, and K.A. Smart. Replicative ageing and senescence in saccharomyces cerevisiae and the impact on brewing fermentations. *Microbiology*, 146:1023–34, 2000.

[100] M.G. Barker and K.A. Smart. Morphological changes associated with the cellular aging of a brewing yeast strain. *J. Am. Soc. Brew. Chem.*, 54: 121–126, 1996.

Chapter 8

Appendix A

8.1 Filter Design Concept Summary

The principal differences in features of the different device concepts and the manufacturing and flow considerations they are intended to evaluate are detailed in the following tables.

Design	Feature	Manufacturing Considerations	Flow Considerations
A	converging channels	—	reducing meniscus radius to counteract increasing hydraulic drag
	irregular array of pillars	—	increase opportunities for particle arrest
	few elements with balancing pillars	balance etch loading	avoid excessive flow restriction
A2	converging channels	—	reducing meniscus radius to counteract increasing hydraulic drag
	regular array of pillars	improve etch balance	reduce flow path complexity, improve fluid flow characteristics
	uniform pillar size	reduce mask cost and improve etch balance	—

Table 8.1: 'A' and 'A2' device concept summary

Design	Feature	Manufacturing Considerations	Flow Considerations
B	uniform channels	—	increased final filter stage processing volume
	irregular array of pillars	—	tortuous particle flow path, increase opportunities for particle arrest
	uniform pillar size	decrease mask drafting complexity and improve etch balance	—
	elements stretch to edge of wells	improve etch balance	avoid trapped particles
B2	uniform channels	—	increased final filter stage processing volume
	irregular array of pillars	—	tortuous particle flow path, increase opportunities for particle arrest
	finer filtration stages and pillar sizes	assess limits of DRIE process	refine particle type separation

Table 8.2: 'B' and 'B2' device concept summary

Design	Feature	Manufacturing Considerations	Flow Considerations
B3	uniform channels	–	increased final filter stage processing volume
	linear filtration plates	reduce mask cost and improve etch balance	simple flow path to enhance wetting
	fine filtration stages	assess limits of DRIE process	refine particle type separation
C	uniform channels	–	increased final filter stage processing volume
	regular array of square pillars	reduce mask cost and improve etch balance	–
	square wells	reduce mask cost and improve etch balance	increased filter stage processing volume
	uniform pillar size	reduce mask cost and improve etch balance	–

Table 8.3: 'B3' and 'C' device concept summary

Design	Feature	Manufacturing Considerations	Flow Considerations
C2	uniform channels	—	increased final filter stage processing volume
	linear filtration plates	reduce mask cost and improve etch balance	simple flow path to enhance wetting
	square wells	reduce mask cost and improve etch balance	increased filter stage processing volume
D	non-linear channels	—	redundancy in event of single stage blockage
	multiple channels to each well	—	redundancy in event of single stage blockage
	external drain feature	—	increased/continuous processing volume
	reduced number of primary channels	to accommodate redundancy conduits	—

Table 8.4: 'C2' and 'D' device concept summary

Design	Feature	Manufacturing Considerations	Flow Considerations
E	divergent channels	—	increased final filter stage processing volume
	equispaced uniform round pillars	decrease mask drafting complexity and improve etch balance	—
	elements stretch to edge of wells	improved etch balance	avoid trapped particles
H	linear format	reduce mask cost and improve etch balance	simple fluid flow path
	multiple element types	etch quality comparison	filtration feature comparison
	5 stage filtration	—	more filter gradations
	3 reservoirs	improved etch balance	—

Table 8.5: 'E' and 'H' device concept summary